Spring 2012

Molecular Dynamics Studies on Nanoscale Gas Transport

Murat Barisik
Old Dominion University

MOLECULAR DYNAMICS STUDIES ON NANOSCALE GAS TRANSPORT

by

Murat Barisik
B. S. June 2006, Middle East Technical University, Turkey
M. S. June 2008, Middle East Technical University, Turkey

A Dissertation Submitted to the Faculty of
Old Dominion University in Partial Fulfillment of the
Requirements for the Degree of

DOCTOR OF PHILOSOPHY

AEROSPACE ENGINEERING

OLD DOMINION UNIVERSITY
May 2012

Approved by:

Ali Beskok (Director)

Robert Ash (Member)

Shizhi Qian (Member)

Yan Peng (Member)

ABSTRACT

MOLECULAR DYNAMICS STUDIES ON NANOSCALE GAS TRANSPORT

Murat Barisik
Old Dominion University, 2012
Director: Dr. Ali Beskok

Three-dimensional molecular dynamics (MD) simulations of nanoscale gas flows are studied to reveal surface effects. A smart wall model that drastically reduces the memory requirements of MD simulations for gas flows is introduced. The smart wall molecular dynamics (SWMD) represents three-dimensional FCC walls using only 74 wall molecules. This structure is kept in the memory and utilized for each gas molecule surface collision. Using SWMD, fluid behavior within nano-scale confinements is studied for argon in dilute gas, dense gas, and liquid states. Equilibrium MD method is employed to resolve the density and stress variations within the static fluid. Normal stress calculations are based on the Irving-Kirkwood method, which divides the stress tensor into its kinetic and virial parts. The kinetic component recovers pressure based on the ideal gas law. The particle-particle virial increases with increased density, while the surface-particle virial develops due to the surface force field effects. Normal stresses within nano-scale confinements show anisotropy induced primarily by the surface force-field and local variations in the fluid density near the surfaces. For dilute and dense gas cases, surface-force field that extends typically 1nm from each wall induces anisotropic normal stress. For liquid case, this effect is further amplified by the density fluctuations that extend beyond the force field penetration region. Outside the wall force-field penetration and density fluctuation regions the normal stress becomes isotropic and recovers the thermodynamic pressure, provided that sufficiently large force cut-off distances are utilized in the computations. Next, non-equilibrium SWMD is utilized to investigate the surface-gas interaction effects on nanoscale shear-driven gas flows in the transition and free molecular flow regimes. For the specified surface properties and gas-surface pair interactions, density and stress profiles exhibit a universal behavior inside the

wall force penetration region at different flow conditions. Shear stress results are utilized to calculate the tangential momentum accommodation coefficient (TMAC) between argon gas and FCC walls. The TMAC value is shown to be independent of the flow properties and Knudsen number in all simulations. Velocity profiles show distinct deviations from the kinetic theory based solutions inside the wall force penetration depth, while they match the linearized Boltzmann equation solution outside these zones. Afterwards, surface effects are studied as a function of the surface-gas potential strength ratio ($\varepsilon_{wf}/\varepsilon_{ff}$) for the shear driven argon gas flows in the early transition and free molecular flow regimes. Results show that increased $\varepsilon_{wf}/\varepsilon_{ff}$ results in increased gas density, leading towards monolayer adsorption on surfaces. The near wall velocity profile shows reduced gas slip, and eventually velocity stick with increased $\varepsilon_{wf}/\varepsilon_{ff}$. Similarly, using MD predicted shear stress values and kinetic theory, TMAC are calculated as a function of $\varepsilon_{wf}/\varepsilon_{ff}$, and TMAC values are shown to be independent of the Knudsen number. Results indicate emergence of the wall force field penetration depth as an additional length scale for gas flows in nano-channels, breaking the dynamic similarity between rarefied and nano-scale gas flows solely based on the Knudsen and Mach numbers.

To my beloved grandfather Hikmet Kirpi

Sevgili dedeciğim Hikmet Kirpi'ye

ACKNOWLEDGMENTS

It is with great pleasure and honor that I can thank my thesis advisor, Dr. Ali Beskok for not only supporting my PhD studies, but also his continuous support of my research, communication, and writing skills. His guidance, encouragement, and most importantly, his friendship during my graduate years provided me a well-rounded PhD experience. He supported me to not only grow as a researcher, but also as an instructor and an independent thinker. Without Dr. Beskok's bright ideas, patience and attention to my work, this thesis or research would not have been possible. He always provided me with excellent comments, and listened to me when I was excited about a new idea. I am not sure many graduate students are given the opportunity to develop their own individuality and self-sufficiency by being allowed to work with such independence.

Additionally, I am very grateful for the friendship of all of the members of his research group, especially Dr. Bohung Kim, with whom I worked closely and was mentored in the field of molecular dynamics.

I would also like to acknowledge the generous support from National Science Foundation (NSF) which was greatly appreciated (Grant # DMS 0807983).

I thank my parents, Mesut and Hülya Barisik, for their faith in me and allowing me to be as ambitious as I wanted. Also, I thank my grandparents, Hikmet and Azize Kirpi, for their endless love. It was under their watchful eye that I gained so much drive and an ability to tackle challenges head on.

Finally, and most importantly, I would like to thank the love of my life, Megan. Her part through my graduate years was one of a kind as she was my life coach, teammate, best friend and sweet valentine as she will be forever.

NOMENCLATURE

English Symbols

a	Acceleration, nm/ns^2
c_m	Mean thermal speed, nm/ns
f_{ij}	Force acting on molecule i from molecule j, N
F	Force, N
H	Channel height, nm
k	Modified Knudsen number, (No Units)
k_b	Boltzmann constant, (J K^{-1})
Kn	Knudsen number, (No Units)
L	Channel length, nm
m	Mass, kg
M	Mach number, (No Units)
N	Number of molecules, #
p	Momentum
P	Pressure, kPa
Q	Mass parameter, (No Units)
r_{ij}	Spacing between the molecules i and j, nm
r_c	Cut-off distance, nm
R	Specific gas constant, J K^{-1} kg^{-1}
Re	Reynolds number, (No Units)
s	Steps, (No Units)
S_{xx}	Normal component of Stress tensor in x-direction, (kPa)
t	time, ns
T	Temperature, K
u_i	Velocity, m/s
Vol	Volume, nm^3
V_{ij}	Potential, m/s
W	Channel width, nm
x	Direction parallel to surface, nm
y	Direction normal to surface, nm

z	Direction parallel to surface, nm
Z	Compressibility factor, (No Units)

Greek Symbols

ε	Depth of potential well, Joule
ε_{wf}	Fluid-solid interaction strength, Joule
ε_{ff}	Fluid-fluid interaction strength, Joule
ρ	Number density, #/nm^3
σ	Molecular diameter, nm
α	Tangential momentum accommodation coefficient, (No Units)
λ	Mean free path, nm
μ	Chemical potential
γ	Ratio of specific heats, (No Units)
τ_∞	Free molecular shear stress, kPa
π	Pi number, (No Units)

Subscripts

i	Molecule i, (No Units)
j	Molecule j, (No Units)
f	Fluid, (No Units)
w	Wall, (No Units)

TABLE OF CONTENTS

Page

LIST OF TABLES

LIST OF FIGURES

Figure Page

CHAPTER 1

INTRODUCTION

Recent developments in micro and nanotechnology have pushed the characteristic lengths of devices from microns down to nanometers. Understanding the behavior of fluids and their manipulation within nanoscale confinements is of great interest for a vast number of applications that include the design of micro/nano electromechanical systems (MEMS&NEMS), microfluidic device components, and computer hard drives (Juang et al. 2007; Tagava et al. 2007). For the latter, the distance between the head and media is on the order of ten nanometers (Figure 1.1), and the next generation disc drives strive to reduce this distance to enhance the magnetic storage capacity (IBM 2004). For gas flow in such small scales the Knudsen number, Kn, (ratio of the gas mean free path, λ, to the characteristic flow dimension, H) emerges as a measure of the degree of rarefaction. Depending on the local Knudsen number, the flow is considered to be in the continuum ($Kn \leq 0.001$), slip ($0.001 \leq Kn \leq 0.1$), transition ($0.1 \leq Kn \leq 10$), and free-molecular ($Kn > 10$) flow regimes (Karniadakis et al. 2005). The mean free path for air at standard conditions is about 65nm. As a result, the nanoscale confined flows of computer hard drives are mostly in the transition and free molecular flow regimes (Figure 1.2).

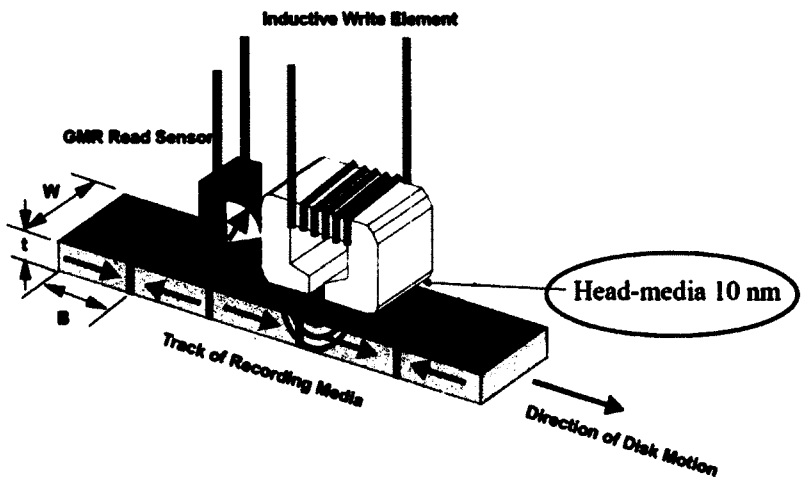

Figure 1.1 Illustration of a magnetic disk drive showing the spacing between the magnetic recording head and the recording medium.

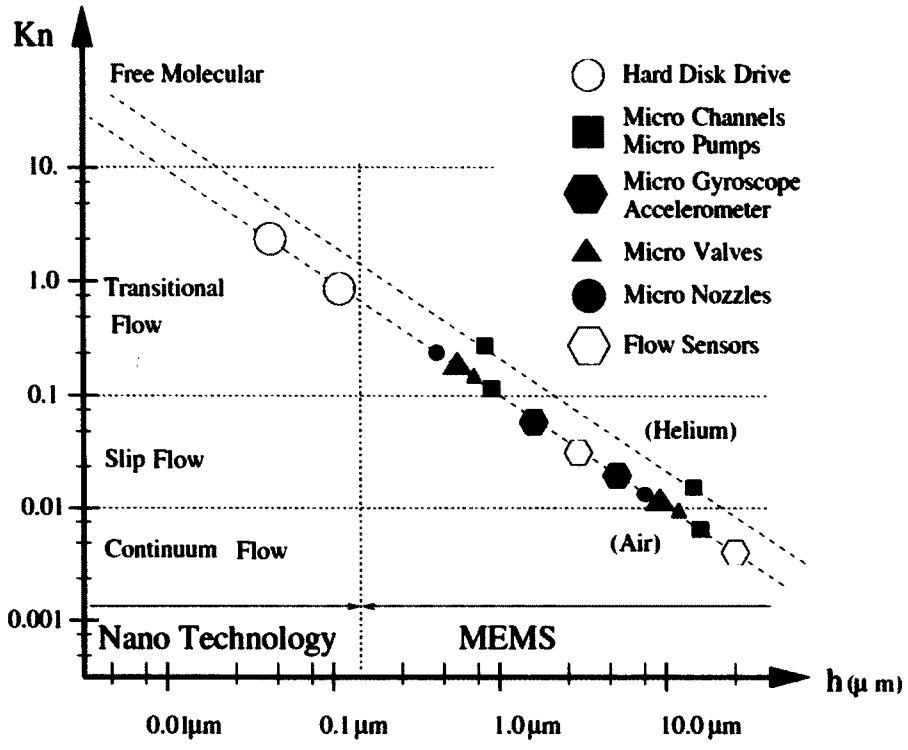

Figure 1.2 Typical MEMS and NEMS applications in standard atmospheric conditions span the entire Knudsen regime (Continuum, slip, transition, and free-molecular flow). Here h denotes a characteristic length scale for the microflow (Karniadakis et al. 2005).

Gas transport in small scales can be characterized by the Reynolds (Re), Mach (M), and Knudsen (Kn) numbers. However, these three parameters for ideal gas flows are interdependent by,

$$Kn = \sqrt{\pi \frac{\gamma}{2}} \frac{M}{Re}, \tag{1}$$

where γ is the ratio of specific heats. As a result, dynamic similarity of rarefied gas flows can be maintained by matching only two dimensionless parameters, preferably the Kn and M (Beskok and Karniadakis 1994). Kinetic theory based investigations of nano-scale gas transport assume "dynamic similarity" between the gas flows in low pressure environments (i.e., large λ) and small scale domains. Such characterizations often neglect the surface force interactions between gas and wall molecules. However, such an approach neglects dimensional effects and thus the surface force field influence which is dominant in nanoconfinements. Within regions experiencing the wall force field, the

transport could significantly deviate from the kinetic theory predictions. As a result, analyses of fluid behavior near a surface require proper investigations of the wall force field effects.

The objective of this study is to investigate the deviations of nano-scale confined shear-driven gas flows from kinetic theory predictions. The intent of this dissertation is to prove that dynamic similarity between the rarefied and nano-scale confined gas flows, often used in the literature by simply matching the Knudsen number, is incomplete. In addition to the channel dimension and gas mean free path, the wall force field penetration length should also be considered as an important length scale in nano-confined gas flows. Findings of this research clearly indicate the importance of wall force field effects in nano-scale confinements, mostly neglected in previous gas flow studies.

The discussion is organized by chapters as summarized here: Chapter 1, Introduction, continues with the following sub-sections. Classical Approaches for Gas Trasnport, presents a current literature review of multiple methods, to include Continuum-based approaches; various Kinetic Theory based solutions such as Boltzmann equation and Direct Simulation of Monte Carlo (DSMC); and the key method for my research, Molecular Dynamics (MD) with my rationale for using it. Molecular Dynamics Method, presents a detailed overview of the method and the key steps in an MD simulation. Chapter 2, Molecular Dynamics Simulations of Nanoscale Gas Flows, introduces my MD gas simulations by describing the Smart Wall model. I also describe the differences of the wall force field in two- and three-dimensions. Chapter 3, Equilibrium Molecular Dynamics Studies on Nanoscale Confined Fluids, studies the density and stress variations within the static fluids in dilute gas, dense gas, and liquid states. Chapter 4, Molecular Dynamics Simulations of Shear Driven Gas Flows, investigates the surface-gas interaction effects for a specified gas/surface couple in the transition and free molecular flow regimes. Chapter 5, Surface-Gas Interaction Effects on Nanoscale Gas Flows, extents the shear driven gas flows study for various surface-gas potential strength ratios. Chapter 6, Conclusions, summarizes and gives the highlights of gas flows in nanoconfinements.

1.1 Classical Approaches for Gas Transport

Fluids inside nanoscale channels can exhibit substantially different physics from what is observed in larger scale systems due to the breakdown of the continuum hypothesis as well as the increased influence of the wall force field effects. Thus any solution procedure is expected to account for both effects which is challenging.

Continuum-based procedures are inadequate for solution of high Kn flows. Its applicability is rather limited with slip flow to early transition regime. Its current applications for small scale flows can be summarized as follow.

The Navier–Stokes equation with no-slip boundary conditions is only applicable for flows at $Kn < 0.01$ known as the continuum regime. No-slip boundary conditions seem to fail in the slip flow regime where a sublayer on the order of one mean free path, known as the Knudsen layer, starts to become dominant between the bulk of the fluid and the wall surface. The flow, in the Knudsen layer cannot be analyzed with the Navier–Stokes equations, and it requires special solutions of the Boltzmann equation. However, for $Kn \leq 0.1$, the Knudsen layer covers less than 10% of the channel height and can be neglected by extrapolating the bulk gas flow towards the walls. This results in a finite velocity slip value at the wall with the flow governed by the Navier–Stokes equations, and rarefaction effects modeled through the partial slip at the wall. However further increase of Kn leads the breakdown of constitutive laws defining the stress tensor and the heat flux vector. Thus, in the transient regime, the solution requires higher-order corrections to the constitutive laws, resulting in the Burnett or Woods equations (Woods 1993). In general, the conservation equations are valid for continuum as well as for rarefied flows, but the viscous stresses and the heat flux have to be determined differently for distinct flow regimes. As a result, rarefaction effects alone bring many challenges to the formulation of relevant constitutive laws and boundary conditions for high-order continuum models (in Kn). Furthermore, these models are not capable to direct account for the wall force field effects, so continuum based methods are improper to model nanoscale gas flows.

Consequently, gas transport in small scales is often investigated using kinetic theory based on the Boltzmann equation where the time evolution of distribution density in space is described by molecular transport and binary intermolecular collisions. It expresses the global non-equilibrium distribution in terms of local equilibrium distributions which enables application of properties of equilibrium systems to the study of a non-equilibrium system. Boltzmann equation for a simple dilute gas is,

$$\frac{\partial f}{\partial t}+\frac{\partial f}{\partial x}\cdot\frac{p}{m}+\frac{\partial f}{\partial p}\cdot F=\left.\frac{\partial f}{\partial p}\right|_{collision}, \tag{2}$$

where f is distribution function, t is time, x is position, p is momentum and F is force. The terms on the left hand side of Equation (2) are considering the change in number of molecules by time, the convection of molecules by molecular velocity and the convection of molecules due to external force F, respectively. On the right hand side, collision term giving the insight of molecular interactions needs careful consideration and brings difficulties. Gas-surface interactions are often described using simple rules, such as the diffuse and specular reflection. More complex gas/surface interaction models, based on the Maxwell's scattering kernel (Karniadakis et al. 2005) or Cercignani-Lampis model also exist (Cercignani and Lampis 1971). Boltzmann equation can yield analytical solutions in the free molecular flow regime, where the intermolecular collisions can be neglected. There are many analyses utilizing the Boltzmann equation with simplifications in collision term (Sone et al. 1990; Fukui and Kaneko 1987, 1990). However, analytical and numerical solutions of the Boltzmann equation are usually challenging due to the complexity induced by the collision integral terms and the multi-dimensionality of the equation.

Alternatively, Direct Simulation Monte Carlo (DSMC), first developed by Bird (Bird 1994), can be utilized to solve the Boltzmann equation by modeling the fluid flow using "simulation molecules" which represent a large number of real molecules in a probabilistic simulation. It is a numerical method for modeling rarefied gas flows, in which the mean free path of a molecule is of the same order (or greater) than a representative physical length scale. The typical DSMC method employs hundreds of thousands or even millions of "simulated molecules" that mimic but do not follow

exactly the motion of real molecules. For a molecular based simulation model, computing the exact motion and interactions of all these molecules is not possible. However, DSMC method can achieve to track the evolution of this molecular process in space and time by splitting the molecular motion (modeled deterministically) and intermolecular collisions (modeled probabilistically). For efficient numerical implementation, the space is divided into cells and molecules are moved through a simulation of physical space in a realistic manner directly coupled to physical time. The main computational approximations associated with the DSMC method are the ratio of the number of real molecules to the number of simulated molecules (particle weight), the time step and the finite cell and subcell sizes in the physical space. Since the molecules will go through intermolecular collisions, the overall time step for simulation is chosen smaller than the mean collision time. Similarly, in order to capture correct intermolecular interactions between neighboring cells, the cell size is about one third of the local mean free path (or less). Since only a small portion of the molecules is simulated, intermolecular collisions and molecule-surface collisions are needed to be calculated using probabilistic, phenomenological models. Common collision models include the Hard Sphere model, the Variable Hard Sphere (VHS) model, and the Variable Soft Sphere (VSS) model. For molecule-surface collision calculations, a priori knowledge of the accommodation coefficients must be used which is a weakness of the DSMC method, similar to the Navier–Stokes-based slip and even Boltzmann-equation-based simulation models. At the end, the molecular movement and collision phases are decoupled over time periods. One can use DSMC to simulate flows in the slip, transition and free-molecular flow regimes. The DSMC could also include the gas-surface interaction models based on the aforementioned scattering kernels. (Karniadakis et al. 2005; Cercignani and Lampis 1971; Cercignani and Pagani 1966). Based on these theoretical and algorithmic developments there has been a vast number of investigations of gas flows in the late transition and free molecular flow regimes ($Kn \geq 5$) (Bahukudumbi et al. 2003a, b; Loyalka at al. 1979; Park et al. 2004; Stefanov et al. 1998; Willis 1962). Overall, DSMC is a very powerful approach in simulating high Knudsen number rarefied flows but there are several possible limitations and error sources.

The fundamental limitation of kinetic theory based approaches in nanoscale gas transport investigations is the assumption of "dynamic similarity" between the gas flows in low pressure environments (i.e., large λ) and small scale domains. Such characterization based on Knudsen number is only valid if one can neglect the surface force interactions between gas and wall molecules. However, even for the most simplified case of atomically smooth non-charged surfaces, van der Waals force field interactions between the wall and gas molecules induce variations in momentum and energy transport within the wall force field penetration depth, which is typically one nanometer from each wall. As a result, 40% of a 5.4nm wide channel would experience the wall force field effects, within which the transport could significantly deviate from the kinetic theory predictions. Therefore, one must understand and evaluate the influence of this near-wall force field on the nano-scale confined flow, and characterize deviations from the kinetic theory predictions.

On the other hand, such wall force field effects can be directly accounted within a deterministic computational process by Molecular Dynamics (MD) method. Simply stated, MD is a microscopic form of computer simulation where the time evolution of a system of atoms is governed by Newton's laws of motion. With the aid of modern computing, it is possible to numerically solve the equations of motion and use statistical mechanical theory to measure quantities of interest. MD method is mostly suitable for simulating very small volumes of liquid flow, with linear dimensions on the order of 100nm or less and for time intervals of several tens of nanoseconds. It can deal effectively with nanodomains and is perhaps the only accurate approach in simulating flows involving very high shear where the continuum or the Newtonian hypothesis may not be valid. For dimensions less than approximately ten molecules, the continuum hypothesis breaks down even for liquids, and MD should be employed to simulate the atomistic behavior of such a system. In fact, liquid transport in nano-channels have been studied extensively using MD, by utilizing the apropriate wall/liquid interaction potentials (Li et al. 2010; Thompson and Troian 1997). However, MD is inefficient for simulating gas microflows due to the large intermolecular distances that require relatively large domains. Thus, literature on MD simulations of rarefied gas flows is rather limited. In a series of studies Cieplak, et al., investigated gas flows in nano-channels using three-

dimensional MD simulations (Cieplak et al. 1999, 2000, 2001, 2006). Particularly, (Cieplak et al. 2000) presents Poiseuille flow for Kn = 0.03, 0.12, and 5.52 in a nano-channel with 12.75σ in height, by assigning periodic boundary conditions along the channel length and width of 13.6σ and 5.1σ, respectively. These simulations utilized purely repulsive and attractive wall models, and have demonstrated density accumulation effects near the boundaries, results of which have been quantified in (Cieplak et al. 1999). Furthermore, differences in the velocity profiles from the predictions of continuum hydrodynamics are shown. In Cieplak, et al., (2001), the boundary conditions at the fluid/solid interface is presented for monatomic and chain molecules. Density immediately next to the surface for both kinds of fluids is shown to be largely independent of the bulk density for different Kn values, driven by the attractive walls with large gas/wall interaction strength. The effect of patterned surface on both chain and simple fluid cases are presented in (Cieplak et al. 2006). In next section, MD simulation technique is discussed in details.

1.2 Molecular Dynamics Method

MD considers time evolution of a system of atoms governed by Newton's laws of motion. It generate a sequence of points in phase space as a function of time, these points belong to the same ensemble, and they correspond to the different conformations of the system and their respective momenta. An ensemble is a collection of points in phase space satisfying the conditions of particular microscopic state. Several ensembles, with different constraints on the microscopic state of the system are commonly used in MD. Some general ensembles are isobaric-isothermal ensemble (*NPT*) categorized by fixed number of the molecules (*N*), temperature (*T*) and pressure (*P*); microcanonical ensemble (*NVE*) where the number of the molecules, sytem volume (*V*) and energy are kept constant corresponding to an isolated system; canonical ensemble (*NVT*) for a constant number of the molecules and volume of an isothermal sytem; and grand canonical ensemble (μVT) for constant chemical potential (μ), sytem volume and temperature. MD simulations can be classified into two group by statistical mechanics. An equlibrium system of MD is named as Equilibrium MD (EMD) which is applicable only for *NVE*

ensemble of a constant energy system. On the other hand, all other ensembles with a constant T, P or μ, fluid properties are described by nonequilibrium statistical mechanics, and Nonequilbrium MD (NEMD) will be performed. Typically, NEMD involves applying a perturbation to the usual equations of motion. The perturbation can be constant throughout the simulation or it can evolve with time (i.e. a sinusoidally oscillating perturbation).

The motion of an ensemble of atoms in MD simulations is governed by interatomic forces arising from interaction of electrons and nuclei. Thus, the results obtained from MD simulations are linked with ability of the potential energy function to represent the underlying system. In classical MD simulation, a model system consisting of N particles is selected and Newton's equations of motion ($F=ma$) are solved until the properties of the system no longer change with time. Once a steady state is reached, the required measurements are performed.

The key steps in MD simulation are,

- Initialization: Initial positions and velocities must be assigned to N particles
- Force calculation; Forces due to the interactions are computed.
- Integration of the equations of motion: Verlet integration rule
- Data storage and analysis: After the equations of motion are integrated, the relevant properties of the system (i.e. temperature, pressure,..) are calculated and stored.

1.2.1 Initialization

In a typical molecular dynamics simulation, a set of molecules is introduced initially with a random velocity for each molecule corresponding to a Boltzmann distribution at the temperature of interest.

1.2.2 Force Calculation

In MD, interaction of the molecules is prescribed in the form of a potential energy (V_i). Realistic intermolecular potentials are constructed by modeling the atom–atom interaction potential using relatively simple equations. In most simple case, molecules repel each other at very short range as explained in Pauli's Exclusion Principle (two

electrons in the same orbit cannot shear the same quantum states) and attract at longer distances by induced dipole interaction. Even when the atoms have no net charge, they have charge distributions, and polarizabilities, which lead to weak attractions. Therefore, netural molecules attract because of charge asymmetries. The sum of those attractive and repulsive forces due to the molecular interactions are called Van der Walls interactions.

Modeling intermolecular potentials is evolved over time employing the MD method. Initial MD simulations employed hard sphere molecules defined by infinite repulsive potential becoming effective only if the intermolecular distance (r) is equal or smaller than the atomic diameter. With later developments, soft sphere models extended this effective distance with a short range repulsive force represented by a potential continuously decaying with increasing r. However, the typical Van der Waals potential has a steep repulsive wall at small r and a region of positive slope that accounts for the attractive forces between atoms at larger separations as explained earlier. There are many different mathematical functions that have this basic shape; however, the one most encountered is known as the Lennard Jones (LJ) potential (Karniadakis et al. 2005). The LJ model takes into account not only the short-range repulsion encountered when atoms collide, but also long-range attractive forces that occur at larger separations. Many studies have demonstrated that the LJ model is the most accurate model for the Argon intermolecular potential. The most common use of LJ is LJ (12-6), where the $1/r^{12}$ term dominates short range behavior and the $1/r^{6}$ term dominates at long range, modeling the attractive nature between atoms. LJ (12-6) potential is given by,

$$V(r_{ij}) = 4\varepsilon\left(\left(\frac{\sigma}{r_{ij}}\right)^{12} - \left(\frac{\sigma}{r_{ij}}\right)^{6}\right), \tag{3}$$

where r_{ij} is the intermolecular distance, ε is the depth of the potential well and σ is the molecular diameter. Potential and force distribution of an LJ (12-6) is plotted in Figure 1.3.

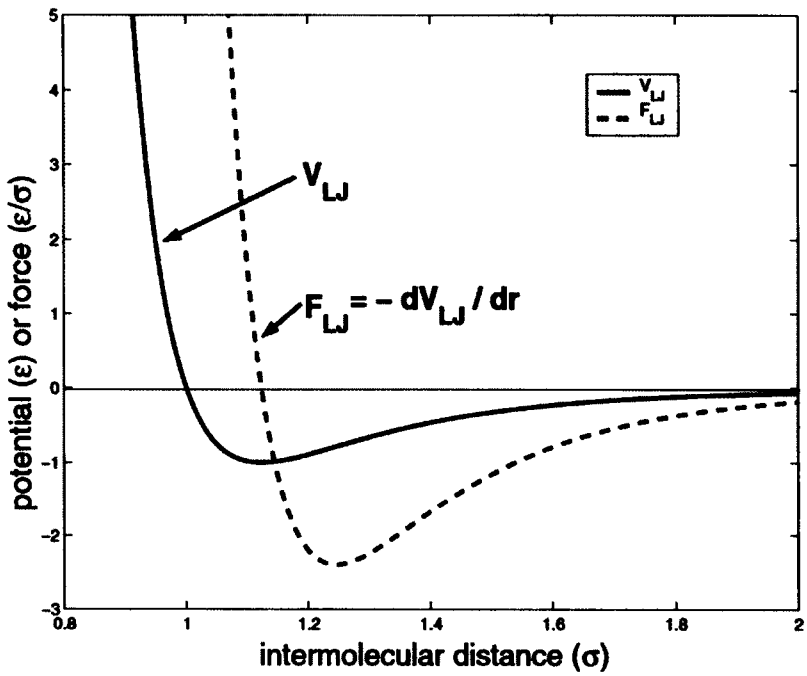

Figure 1.3 Potential and force distribution of an Lennard Jones (12-6) model through intermolecular distance (Karniadakis et al. 2005).

Formally, all interactions between the non-bonded particles have to be calculated in MD. Since the LJ potential vanishes at larger molecular distances, only the interactions with particles within a certain cut-off radius (r_c) need to be calculated. Therefore, the intermolecular interaction forces were truncated and switched to zero at a certain cut-off distance. For L-J potentials, it is *customary* to utilize a cut-off distance of 1.08nm, which is approximately equal to 3σ (Allen and Tildesley 1989). Using a larger cut-off distance does not affect the density predictions for LJ fluids. However, long-range attractive LJ interactions are crucial for accurate calculations of dense gas and liquid pressure.

However, the truncating at r_c causes a discontinuity in energy conservation and actual atomic motion, with atoms separated at a distance close to r_c moving in and out of interaction range repeatedly. To avoid a jump discontinuity at r_c, the LJ potential must be shifted upward a little so that the truncated potential would be zero exactly at the r_c. The shifted L-J potential function is given by,

$$V_{truncated}(r_{ij}) = 4\varepsilon\left(\left(\left(\frac{\sigma}{r_{ij}}\right)^{12} - \left(\frac{\sigma}{r_{ij}}\right)^{6}\right) - \left(\left(\frac{\sigma}{r_c}\right)^{12} - \left(\frac{\sigma}{r_c}\right)^{6}\right)\right). \quad (4)$$

The most computationally intensive part of an MD simulation is calculating the forces between pairs of particles. For a potential function without a cut-off radius, it is necessary to evaluate forces for every pair within the simulation region. However, the use of a truncated potential function greatly reduces the number of interaction pairs, and subsequently the number of pairs worth investigating. Evaluating pairs of particles separated by a distance greater than r_c is wasteful, necessitating the need for a method that is less computationally intensive. In order to address this, Link cell method can be utilized to construct the list of pairs needed to be considered in force calculations (Allen and Tildesley 1989). It divides the simulation domain into small equal size cells which are must be at least one r_c long in all directions and it creates the list of molecules inside each cell. Thus, any molecule in a cell interacts with only the other molecules in the same cell and in its' neighbors which is 26 cells for a 3D simulation.

In general, the potential energy (V) of a system consisting of N interacting particles can be expressed as,

$$V = \sum_i V_1(r_i) + \sum_i \sum_{j>i} V_2(r_i, r_j) + \sum_i \sum_{j>i} \sum_{k>j>i} V_3(r_i, r_j, r_k) + \cdots, \tag{5}$$

The first term on the right-hand side (V_1) is the potential energy due to the external fields, and the remaining terms, which are modeled by intermolecular potentials, represent the particle interactions (e.g., V_2 is the potential between pairs of particles and V_3 is the potential between particle triplets and so on). Typically, Equation (5) is truncated after the second term; i.e., the three-body and higher-order interactions are neglected.

The interatomic forces based on the potential energy between individual particles are defined as,

$$f = -\nabla V(r). \tag{6}$$

By using Equations (5) and (6), the interactions between the particles are examined and the forces due to these interactions are calculated at each time step.

1.2.3 Integration of the Equations of Motion

The equations of motion are integrated using time integration algorithms that are based on finite difference methods derived from the Taylor expansion. Using time integration techniques, it is possible to determine the velocity and position of a particle from its acceleration. The most commonly used time integration algorithm is the Verlet integration rule as given by follows.

$$r_i(t+\delta t) = r_i(t) + v_i(t)\delta t + \frac{1}{2}a_i(t)\delta t^2, \tag{7}$$

$$v_i(t+\delta t) = v_i(t) + \frac{1}{2}[a_i(t) + a_i(t+\delta t)]\delta t, \tag{8}$$

where r_i is the position, v_i is the velocity and a_i is the acceleration of particle i. The Verlet algorithm uses position, velocity and accelerations at time t to calculate new positions at time $t+\delta t$ which is used afterward to find the acceleration at time $t+\delta t$. Then, velocity at time $t+\delta t$ is calculated by velocity and acceleration at time t and new acceleration at time $t+\delta t$.

For several reasons (drift as a result of force truncation and integration errors, heating due to external or friction forces), it is necessary to control temperature of the system in MD simulation. Temperature control is obtained by scaling the particles velocities for a desired temperature which may need altering of equation of motion.

A constant-temperature MD simulation can be realized in a variety of ways. Among several approaches, the extended-ensemble method first proposed by Nose and later modified by Hoover (Evans and Hoover 1986) is the most significant technique. In this method, the system Hamiltonian is extended by introducing a thermal reservoir and a frictional term in the equations of motion. The frictional force is proportional to the product of each particle's velocity and a friction parameter ξ. This friction parameter (or "heat bath" variable) is a fully dynamic quantity with its own equation of motion; the time derivative is calculated from the difference between the current kinetic energy and the reference temperature. In Hoover's formulation, the particles' equations of motion are given by,

$$\frac{d^2r_i}{dt^2} = \frac{F_i}{m_i} - \xi\frac{dr_i}{dt}, \tag{9}$$

where the equation of motion for the heat bath parameter ξ is,

$$\frac{d\xi}{dt} = \frac{1}{Q}(T - T_0). \tag{10}$$

The reference temperature is denoted by T_0, while T is the current instantaneous temperature of the system. The strength of the coupling is determined by the constant Q (usually called the "mass parameter" of the reservoir) in combination with the reference temperature. Since the mass parameter is dependent on the reference temperature, it is an awkward way of describing the coupling strength.

1.2.4 Data Storage and Analysis

After the equations of motion are integrated, the relevant properties of the system (e.g., temperature, pressure, volume) are calculated and stored. MD simulation generates the trajectories of all particles in the system, but to obtain deeper insight into the system being studied, one needs to analyze the trajectories obtained during the MD simulation. To investigate nanoflows in channels and pores, where the fluid density is inhomogeneous, it is useful to compute the spatial distribution of fluid density.This is usually performed using the "binning method" (Allen and Tildesley, 1994). In this scheme the relevant spatial domain (i.e., the domain where the density distribution of the species needs to be computed) is partitioned into a number of cells, which are identified as the "bins." The number of atoms in each bin is computed from the knowledge of the positions of the atoms. In order to obtain a better statistical analysis of the number density in a bin, the number of atoms in the bin is added for a number of steps and then the total number of atoms in the bin is diveded by the number of steps and the volume of the bin. Thus, the number density, ρ_i, of the i^{th} bin, averaged over s steps, is given by,

$$\rho_i = \langle N_i / Vol_i \rangle_s, \tag{11}$$

where N_i is the total number of atoms in the i^{th} bin during each step and Vol_i is the volume of the i^{th} bin.

The velocity profile is one of the most important measurables for fluid transport, and can be computed in a similar manner as the density profile. Usually, the simulation system is partitioned into n bins, and statistics of the fluid velocity are gathered separately in each bin. Assuming that during an s-step simulation, at each step k, there are

$n_{k,i}$ particles in the i^{th} bin, and the velocity of each of these particles (denoted by j) is given by $u^j_{k,i}$, then the average fluid velocity u_i in the i^{th} bin can be computed by

$$u_i = \frac{\sum_{k=1}^{s}\sum_{j=1}^{n_{k,i}} u^j_{k,i}}{\sum_{k=1}^{s} n_{k,i}}. \tag{12}$$

The other important property for a confinement is the pressure tensor. Computations of the stress tensor components for an atomistic system have two additive components. The first is the kinetic contribution from throughput of linear momentum resulting from the particle velocities, while the second component is the virial term, which is an internal contribution from intermolecular forces between the particles. In these simulations Irving-Kirkwood expression was utilized to compute the stress tensor components for an N particle system with unity differential operator approximation as follows (Irving and Kirkwood 1950; Todd et al., 1995),

$$S_{kl} = \frac{1}{Vol}\left\langle \sum_i^N m^i (u^i_k - \bar{u}^i_k)(u^i_l - \bar{u}^i_l) + W_{kl} \right\rangle, \tag{13}$$

$$W_{kl} = \frac{1}{2}\sum_{i,j}^{N} (r^j_k - r^i_k) f^{i,j}_l, \tag{14}$$

where the first term on the right hand side of Equation (13) is the kinetic, and the W_{kl} term is the virial component. In the kinetic part, m^i is the atomic mass of particle i, while k and l are the axes of the Cartesian coordinate system, u^i_k and u^i_l are the peculiar velocity components of particle i in the k and l directions, and $\bar{u}^i_k$ and $\bar{u}^i_l$ are the local average streaming velocities at the position of particle i, in the k and l directions, respectively. For non-equilibrium systems, the local streaming velocities should be subtracted from the equilibrium velocities in order to establish mechanical equilibrium at the system's center of mass. For the virial component, $(r^j_k - r^i_k)$ in Equation (14) is k^{th} component of the relative distance vector between particles i and j, and $f^{i,j}_l$ is the l^{th} component of the intermolecular force exerted on particle i by particle j.

CHAPTER 2

MOLECULAR DYNAMICS SIMULATIONS OF NANOSCALE GAS FLOWS

MD simulations of gas flows are computationally expensive due to the following reasons: First, gas flows evolve through intermolecular collisions characterized by the mean free path. Despite the large Kn value induced by the nano-scale confinement, the computational domain in the lateral and axial flow directions must be extended to a distance on the order of λ to allow intermolecular collisions in these directions. This requirement results in simulation volumes on the order of λ^3/Kn that contain a large number of gas molecules ($N\times\lambda^3/Kn$, N being the number density). Second, the MD simulations must be executed for time-scales on the order of several intermolecular collision times to result in a state amenable for time or ensemble averaging. The third issue is the excessively large number of wall molecules required to atomistically model the surfaces, which induces extensive memory requirements.

In order to address the overwhelming computational burden of the excessive number of wall molecules, a Smart Wall MD (SWMD) algorithm was developed to reduce the memory requirement of wall modeling (Barisik et al. 2010). For a three-dimensional FCC crystal structured wall with (1,0,0) plane facing the gas molecules, the SWMD limits memory use of a semi infinite wall slab into a stencil of 74 wall molecules by utilizing the cut-off distance definition of L-J potential, and enables modeling of gas flows within sufficiently large three-dimensional domains. SWMD is discussed in detail in the following section.

2.1 Smart Wall Model

MD simulations of rarefied gas flows often require large computational domains, since gas flows evolve through intermolecular and molecule/surface collisions. Without losing generality, channel flow will be examined at a given Kn value. Depending on the base pressure and temperature one can find the number density of gas molecules (N) using the ideal gas law, and can also calculate the mean free path, λ (Karniadakis et al.

2005). The simulation domain needs to encompass the channel height (H) in the transverse direction, and should be large enough to allow intermolecular collisions in the lateral and axial directions. For this reason dimensions of the simulation domain should extend at least one mean-free path in the lateral and axial directions. This requires a computational volume of λ^3/Kn with a total number of gas molecules equal to $N\lambda^3/Kn$. For example, simulation of argon gas at $T = 298K$ and $P = 202kPa$ ($\lambda_{argon} = 32.4nm$) in 3.24 nm height channel ($Kn = 10$) with in a $\lambda \times H \times \lambda$ domain requires simulation of only 177 gas atoms (Table 2.1). However, these gas molecules interact with walls that encompass an area of $2\times\lambda^2$. The wall thickness should be chosen properly to consider the wall crystalline structure and the force field due to all molecules within that structure.

Table 2.1 Comparison of the number of molecules used in SWMD and typical MD simulations.

H=3.24nm , λ=32.4nm	Regular rarefied gas MD		SWMD	
W x L	N_{wall}	N_{gas}	N_{wall}	N_{gas}
λ x λ	36,603	200	74	177
3λ x 3λ	325,803	1,800	74	1,593
5λ x 5λ	903,003	4,900	74	4,425

In this study, the Face Centered Cubic (FCC) fixed lattice structure was considered at various orientations, and assume electrically neutral surfaces whose molecules interact via the 6-12 Lennard-Jones (L-J) potential. Figure 2.2 (a) shows the schematics of the unit FCC fixed lattice solid wall with its atomistic positions and molecular separation length scales. If the (1,0,0) plane faces the fluid, a single FCC structure would occupy a volume of $(0.54)^3$ nm^3 and contain only 14 molecules. Due to the cut-off distance of the L-J potential (1.08nm), one needs to model the walls using at least two layers of FCC structure, which include 23 wall molecules within $2\times(0.54)^3 nm^3$ volume and will cover only $(0.54)^2$ nm^2 surface area. Considering the example of the 3.24nm height channel for argon flow at $T = 298K$ and $P = 202kPa$, the total number of molecules required to model both walls (area of $2\times32.4\times32.4nm^2$) is 36,603 (Table 2.1). One must note my choice of the artificially large pressure of 202kPa. A similar

calculation at one atmosphere would require simulation of 708 argon molecules and 145,203 wall molecules. Therefore, straightforward MD simulations of rarefied gas flows suffer from the overwhelmingly large number of wall molecules, which unnecessarily require large computational memory.

In order to develop the smart wall model (SWM), several layers of FCC wall structures with (1,0,0) planes facing the fluid were first formed. Force interactions were evaluated between a cluster of these FCC structures and a single molecule approaching this cluster with various angles of incidence and target locations. Utilizing the structure of the FCC crystal and the cutoff distance for the L-J potentials, a truncated molecular wall module was developed that accurately represents the force field acting on an approaching molecule due to a semi infinite half plane. The molecular structure of the resulting SWM, consisting of only 74 wall molecules, is shown in Figure 2.1. The centerline of the model and the center molecule are also shown in the figure. Any gas molecule approaching the SWM targets the basic FCC structure immediately around the centerline. The aforementioned cut-off distance is still applied to calculate the force field properly. Otherwise the molecules within one side of the SWM could falsely bias the force calculations due to the motion of the approaching gas molecules, and/or motion of the surface. The SWM structure, consisting of 74 wall molecules, is formed once and maintained in the computer memory as a basic unit. When a gas molecule is about to enter into the force penetration region (3σ) of walls, this basic unit, conforming exactly to the crystalline structure of the surface, is placed on the surface. In the case of moving walls, the desired tangential velocity is imposed on the wall molecules according to the wall speed, simulation time and the initial configuration of the wall crystalline structure.

Figure 2.1 Schematics of the wall surface for optimized gas/wall interaction model for three-dimensional MD simulations. The line represents the center line of the model.

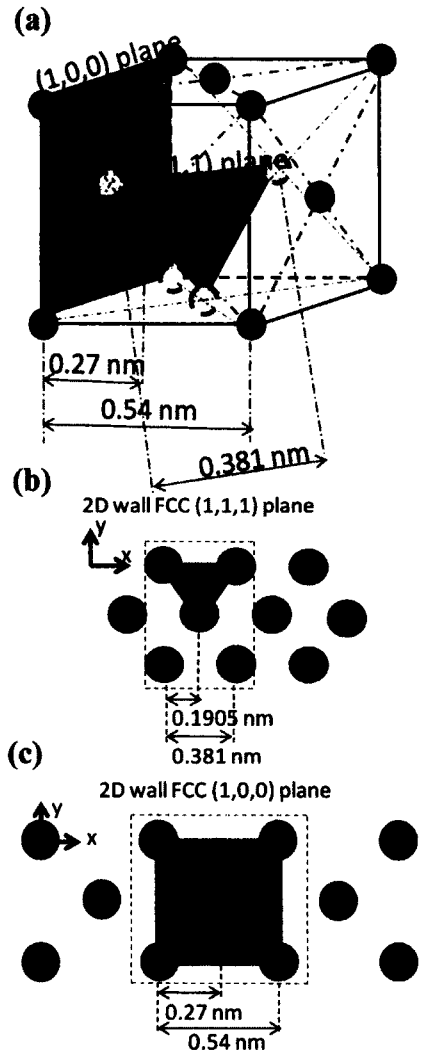

Figure 2.2 (a) The schematic of the unit FCC fixed lattice for solid walls. Modeling of two-dimensional FCC walls corresponding to (b) the (1,1,1) and (c) (1,0,0) planes.

2.2 Two-Dimensional versus Three-Dimensional Wall Models

In order to assess the differences between two- and three-dimensional simulations, two-dimensional wall models were developed shown in Figure 2.2 (b) and (c) by utilizing the (1,0,0) and (1,1,1) planes of the basic FCC structure. Similar two-dimensional molecular models were developed and utilized earlier to simplify the MD computations. The smart wall models corresponding to two-dimensional configurations contain 14 and 18 molecules for the (1,0,0) and (1,1,1) planes, respectively. Since two-dimensional simulations require relatively small number of wall molecules, impact of

SWM for two-dimensional (2-D) models is not as extensive as in three-dimensional (3-D) simulations.

An important aspect of the three- versus two-dimensional MD simulations is the differences between the wall force fields. In Figure 2.3, the force fields on a single molecule approaching the 2-D and 3-D walls directly on the center-line of the wall molecules is shown. The 2-D FCC walls with (1,0,0) plane induces the least amount of force on the approaching molecule, while the 2-D FCC wall with (1,1,1) plane has slightly larger influence. None of the two-dimensional model force fields can induce the force due to the three-dimensional model. Therefore, it is necessary to investigate the effects of these wall force fields on the two- and three-dimensional simulations.

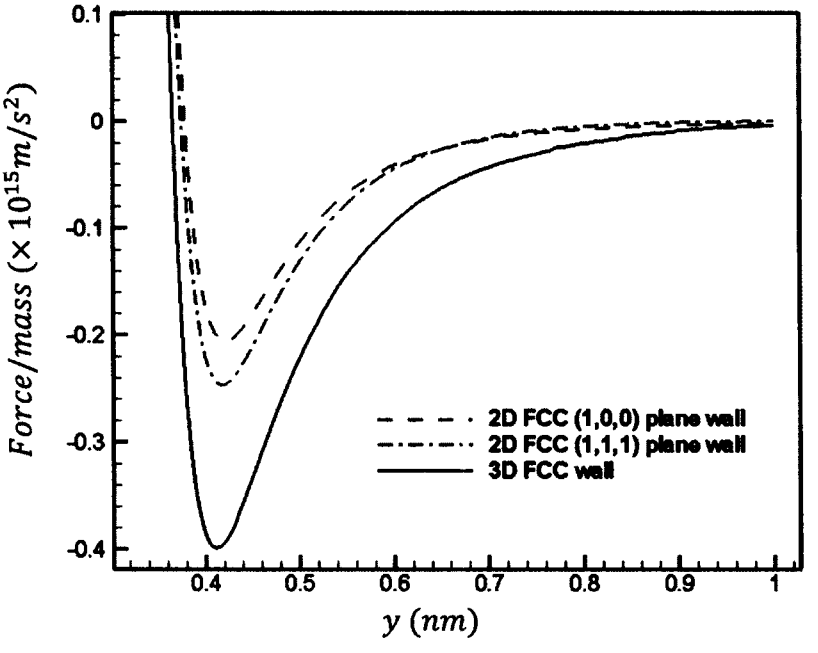

Figure 2.3 Comparisons of wall force fields for two-dimensional FCC (1,0,0) and (1,1,1) planes and three-dimensional FCC (1,0,0) plane for a fluid molecule approaching the wall through the center line of the wall molecule ($\varepsilon_{wf}/\varepsilon_{ff}$ = 1 is assumed).

CHAPTER 3

EQUILIBRIUM MOLECULAR DYNAMICS STUDIES ON NANOSCALE CONFINED FLUIDS

Investigation of the behavior of a fluid next to a solid surface requires careful considerations of wall force fields. For the most simplistic case, van der Waals forces between the fluid and solid molecules can induce significant changes on the fluid properties near a surface (Zhou 2007; Lee and Aluru 2010). As the gradient of scalar potentials, the inter-atomic forces play a key role in the local stress tensor calculations. Different than an ideal gas system of non-interacting point masses, these forces have significant contribution to the stresses in the near wall regions, where the wall force penetration depth extends a couple molecular diameters from the surface, and covers non-negligible portions of a nano-scale domain. Consequently, stresses induced by the surface forces, identified as the "surface virial", should not be neglected (Tsai 1971).

The wall force field can induce adsorption of gas, liquid or dissolved solids on to a surface (Toth 2002). Although useful, adsorption theory essentially utilizes "one-dimensional" force field based on the separation distance between the fluid-solid molecular pair, and molecular structure of the surface (Steele 1973). As a result, the anisotropy in fluid density (i.e., density layering for liquids) and the corresponding stress distribution near a surface cannot be predicted accurately.

The main *goal* of this chapter is to investigate the fluid density and normal stresses in the bulk and near wall regions of simple fluids confined within nano-scale channels. Molecular dynamics simulations are conducted for argon at varous fluid densities corresponding to the dilute gas, dense gas and liquid states. Specifically, the surface virial effects are investigated at various fluid/wall potential strength ratios. To my knowledge, this work presents the density, and normal stress distributions for a nano-channel confined gas for the first time in literature. Liquid argon results exhibit well known density layering, and show normal stress variations in liquids including the surface virial effects. Findings of this research clearly indicate the importance of the wall

force field effects in nano-scale confinements, which are mostly neglected in previous gas flow studies.

This chapter is organized as follows: In Section 1, I describe the MD simulation parameters. In Section 2, I explain the stress tensor computations and methods utilized in the MD algorithm. In Section 3, I present the dilute gas, dense gas and liquid results. Normal stress components of the stress tensor are investigated by considering the contributions of kinetic and virial additive parts separately. Further discussions of the virial component and the relative importance of the particle-particle virial and the surface-particle virial terms are presented. Finally, I present the conclusions of this chapter.

3.1 Three-Dimensional MD Simulation Details

Argon simulations confined between two infinite plates that are H = 5.4nm apart were performed by using the microcanonical ensemble (NVE) (i.e., constant mole, N, volume, V, and energy, E). The *truncated* (6-12) Lennard-Jones (L-J) potential was utilized to model the van der Waals interactions. The mass for an argon molecule is m = 6.63×10^{-26} kg, its molecular diameter is σ = 0.3405nm and the depth of the potential well for argon is ε = $119.8\times k_b$, where k_b is the Boltzmann constant (1.3806×10^{-23}JK^{-1}). Simulations consider different states of argon as dilute gas, dense gas, and liquid states. The domain size, temperature, density and other simulation details can be found in Tables 3.1 and 3.2.

Table 3.1 MD simulation properties.

State	Domain(nm)	T (K)	# Molecs.	ρ (#/nm^3)	ρ (#σ^3/nm^3)	ρ (kg/m^3)
Dilute Gas	54×5.4×54	298	450	0.0286	0.0011	1.896
Dense Gas	2.7×5.4×2.7	180	352	8.94	0.353	593.16
Comp. Liquid	2.7×5.4×2.7	125	801	20.35	0.803	1349.8

Formally, all interactions between the non-bonded particles have to be calculated in MD. Since the L-J potential vanishes at larger molecular distances, only the

interactions with particles within a certain cut-off radius (r_c) need to be calculated. Therefore, the intermolecular interaction forces were truncated and switched to zero at a certain cut-off distance. For L-J potentials, it is *customary* to utilize a cut-off distance of 1.08nm, which is approximately equal to 3σ (Allen and Tildesley 1989). Using a larger cut-off distance does not affect the density predictions for L-J fluids. However, long-range attractive L-J interactions are crucial for accurate calculations of dense gas and liquid pressure. In this work, various cut-off distances were employed between the fluid molecules and MD results were compared with the corresponding thermodynamic state properties of argon to validate my findings (See Table 3.2). In order to model the wall effects consistently, we utilized a constant cut-off distance of 1.08 nm for fluid-surface interactions. My algorithm utilizes the well known link cell method to handle the particle-particle interactions (Allen and Tildesley 1989). Increasing the cut-off distance by a factor of M, increases the computational load by M^6, since the computational cost for MD is proportional to the square of the number of molecules contained within a cell.

Gas states evolve through intermolecular collisions separated by ballistic motion of particles characterized by the "mean free path (λ)". In order to allow intermolecular collisions, gas simulation domains should be on the order of λ in the lateral and axial directions. This requirement results in relatively large simulation volumes for classical MD, which necessitates modeling of a large number of gas molecules and excessively large number of wall molecules. In order to address this computational difficulty, the recently developed "smart wall" MD (SWMD) algorithm (Barisik et al. 2010) is utilized. For L-J molecules interacting with FCC wall structures ((1,0,0) plane facing the fluid), the SWMD utilizes 74 wall molecules as a stencil for fluid-surface interactions. Due to the cut-off distance of the L-J potentials such a small stencil of wall molecules properly incorporates the wall force field effects of an infinite wall; significantly reducing the memory requirements for MD simulations (Barisik et al. 2010). For simplicity, the FCC structured walls have the same molecular mass and molecular diameter of argon ($\sigma_{wall} = \sigma_{argon}$). Periodic boundary conditions are applied in the axial (x) and lateral (z) directions. Overall the computational domain size is related with the mean free path of the gas states. As a result, domain sizes of ($\lambda \times H \times \lambda$) 54nm×5.4nm×54nm, 2.7nm×5.4nm×2.7nm, and 2.7nm×5.4nm×2.7nm are selected for dilute gas, dense gas, and liquid cases,

respectively. Based on my previous work, one mean-free-path long domain-sizes in the periodic dimensions are sufficient to obtain MD solutions for gas flows, independent of the periodicity effects (Barisik et al. 2010).

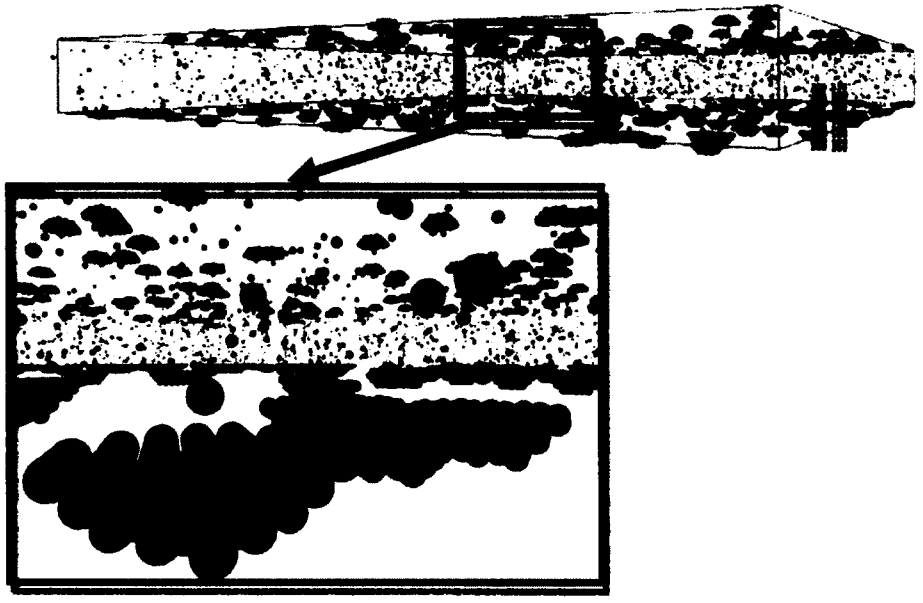

Figure 3.1 Illustration of the SWMD procedure.

Simulations started from the Maxwell-Boltzmann velocity distribution at corresponding simulation temperatures given in Tables 3.1 and 3.2. Initial particle distribution is evolved 10^6 time-steps (4 ns) to reach an isothermal steady state using 4 fs (~0.002τ) time steps using a thermostat. This initial procedure ensures that the fluid system attains equilibrium in presence of the surfaces at desired temperatures, after which, 2×10^6 time steps (8 ns) are performed for time averaging in a thermostat free domain. Longer time averaging has also been performed to confirm convergence of the density and stress profiles to the steady state. Particularly, simulation times were compared with the mean collision times to result in a state amenable for time or ensemble averaging. The mean collision time is predicted by the ratio of λ to the mean thermal speed, $c_m = \sqrt{8RT/\pi}$, where R is the specific gas constant ($208.132 JK^{-1}kg^{-1}$ for Ar) and

T is the gas temperature. The computational domain is divided into 100 bins of approximately $\sigma/10$ in size to resolve the near boundary region accurately.

Two different thermostat techniques are also employed to study their effects in the case of non-equilibrium MD simulations. The Nose-Hoover thermostat is applied to the fluid molecules at each time step to obtain isothermal condition with a fixed lattice model (Evans and Hoover 1986). This deterministic algorithm achieves temperature control by extended system dynamics. In addition, a recently developed thermally interacting wall model is used to simulate the flow domain free of thermostat effects (Kim et al. 2008), which allows specification of a constant wall temperature induced by a velocity scaling thermostat. In this method, the walls have their own thermal oscillations, and they exchange momentum and energy with the fluid particles through intermolecular interactions. This approach enables simulation of heat transfer between the fluid and a surface, and properly dissipates heat through the thermostat applied on the walls (Kim et al. 2008; Kim et al. 2010).

3.2 Computation of the Stress Tensor Components

In my simulations Irving-Kirkwood expression was utilized to compute the stress tensor components for an N particle system given in Equations (13) and (14) (Irving and Kirkwood 1950, Todd et al., 1995). The first term in the Irving-Kirkwood expression is related to the ideal gas law. For an ideal gas in equilibrium (i.e., zero peculiar velocity and no virial), the average normal stress due to the kinetic terms result in

$$\frac{S_{xx}+S_{yy}+S_{zz}}{3}=\frac{1}{3Vol}\left\langle\sum_{i}^{N} m^{i}(u_{k}^{i})^{2}\right\rangle=\frac{NkT}{Vol}=P. \tag{15}$$

Therefore, the kinetic part of the Irving-Kirkwood expression calculates ideal gas pressure exactly by considering the momentum resulting from the particle velocities, while the particle-particle virial terms are corrections to the ideal gas law due to the interaction of particles having non-zero volumes and force-fields. Accurate prediction of pressure, and hence, the thermodynamic state for dense gas and liquids requires considering of the long-range force field interactions between the particles, where the particle-particle virial calculations in Equation (14) have significant effects. Specifically,

The L-J force between a molecule pair experiences sign change at a distance of $2^{1/6}\sigma$ which corresponds to 0.3822nm for argon molecules. For regions where the mean molecular spacing is lower than 0.3822nm, the intermolecular forces are repulsive and the virial terms are positive. For larger mean molecular spacing, the intermolecular forces are attractive and the virial terms become negative. Therefore, local fluid density and the resulting mean molecular spacing carries an important role in the sign of the particle-particle virial terms.

Utilization of the NVE ensemble fixes the fluid density and energy. Since there is no flow or heat flux in the system, fixed energy simulations result in constant temperature. Therefore, one can obtain the correct density and temperature distributions in the domain, while the pressure calculations are sensitive to the long-range intermolecular force interactions. Simply increasing the cut-off distance of the L-J force interactions intensifies the computational cost tremendously. Having recognized this deficiency, *empirical* corrections to the MD based pressure calculations using the Irving-Kirkwood expression have been proposed to model the long-range force interactions (Frenkel and Smit 2002). Since the objective of my study is the investigation of the wall force field effects in nano-scale confined fluids, I paid specific attention to accurate calculations of the local pressure. A detailed discussion on the prediction of local thermodynamic state for dense gas and liquid argon is presented in the results section as a function of the MD cut-off distance used in computations. As can be seen in Table 3.2, the absolute error in MD prediction of local pressure at a given thermodynamic state is less than 8%.

In the following section, Equations (13) and (14) will be utilized for nano-scale confined dilute gas, dense gas and liquid systems, and calculate the normal stress components across nano-channels. I will distinguish the virial effects given in Equation (14) due to the particle-particle and surface-particle interactions. Before I proceed further, I must indicate that the off-diagonal components of the stress tensor (i.e., shear stresses) were also computed. Shear stresses on the fluid induced by the stationary walls were zero, as expected. Given this fact, the normal stress components and their directions presented in this study correspond to the principal stresses and directions for fluids confined in stationary nano-channels.

3.3 Results

3.3.1 Dilute Gas

I first focus on argon at 298K and 1.896kg/m^3 (See Table 3.1 for computed and ideal gas pressure values). This state corresponds to dilute gas, since the mean molecular spacing to molecular diameter ratio is 9.6. Mean free path of argon at this state is 54nm. MD simulations are performed in a nano-channel of 5.4nm in height, and 54nm in length and width. The simulation contains 450 argon molecules. The resulting number density is 0.0286#/nm^3. Systematic studies are performed for various argon-wall interaction strengths, by varying the $\varepsilon_{wall\text{-}Ar}/\varepsilon_{Ar\text{-}Ar}$ ratio ($=\varepsilon_{wf}$). A snapshot of the computational domain is shown in Figure 3.2 (a) for $\varepsilon_{wf}=1$ case, where periodic boundary conditions are imposed along the channel length and width. As can be seen from the figure, the SWMD introduces a stencil of wall molecules on the surface, when a fluid molecule approaches to the surface within the cut-off distance of the L-J potential (1.08nm used for dilute gas cases). Therefore wall stencils in the figure show the locations where argon molecules are in the vicinity of the surface. Comparison of the mean free path to the channel height results in the Knudsen number (*Kn*) of 10. In the case of flow, driven by a pressure gradient, force field or the motion of surfaces, argon gas would have been in the free molecular flow regime, where gas-wall interactions overwhelm the gas-gas collisions (Karniadakis et al. 2005). Although the flow cases are out of scope of the current study, density and normal stress distributions for nano-channel confined fluid are precursor for future flow studies.

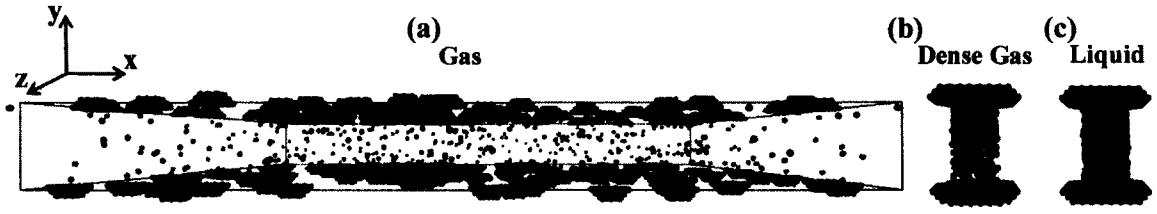

Figure 3.2 Snapshots of (a) dilute gas, (b) dense gas and (c) liquid simulation domains.

Table 3.2 Simulation properties for the periodic cases, and comparison of pressure predictions with the thermodynamic state using various L-J force cut-off distances (r_c).

State	r_c (nm)	ρ^{-1} (m^3/kg)	T (K)	P_{table} (kPa)	P_{MD} (kPa)	Error %	$P_{ideal\ gas}$ (kPa)	Z_{table}
Dense Gas	2.7	0.00505	298.2	11,670	11,705	0.30	12,288	0.95
Dense Gas	2.7	0.00505	178.2	5,451	5,483	0.58	7,345	0.74
Dense Gas	2.7	0.002525	181.9	8,699	8,726	0.31	14,992	0.58
Dense Gas	2.7	0.001686	178.9	10,820	11,157	3.11	22,092	0.49
Dense Gas	2.7	0.001319	166.2	10,630	9,797	-7.83	26,233	0.41
Comp. Liquid	2.16	0.000741	127.7	56,310	59,707	6.03	-	-

Figure 3.3(a) shows the density variation within half of the nano-channel for ε_{wf}=1 case, obtained using the Nose-Hoover thermostat, interactive thermal wall model, and without using a thermostat. The latter case is based on the microcanonical ensemble (NVE), which is appropriate here, since no external work is done on the system. The Nose-Hoover and interactive thermal wall model utilize NVT ensemble on the fluid and surfaces, respectively. Identical density distribution within the nano-channel is predicted using all three methodologies. A density buildup near the surface is observed. For ε_{wf}=1, gas density near the surface increases almost three times with a single peak point, representing accumulation near the surface. This behavior is due to the surface potentials increasing the residence time of particles inside the force penetration depth. Molecules are not immobilized on the surface. Instead, they are trapped in the wall potential field for a certain time period, and experience multiple collisions with the surface. Since the simulation domains are in equilibrium, some of the trapped particles can leave and resume their free flights, while new particles get inside the force penetration region. Therefore, the density is a constant both in the bulk and near wall regions. The density particularly starts to deviate from its bulk value around 2.5σ from the wall. I must indicate that accumulation near the boundary results in slight reductions in gas density in

the bulk of the channel. Specifically, the bulk density reduces to 0.0275#/nm^3, or 96 % of its assigned value. This density reduction is due to the constant number of gas molecules (N) used in MD simulations. Since the gas molecules cannot penetrate to the bins neighboring the wall, gas density goes to zero on the wall. Figure 3.3 (b) shows the temperature profile in the nano-channel obtained without a thermostat. The Nose-Hoover thermostat and interactive thermal wall model techniques predict the same temperature in the system (not shown). Gas is essentially under isothermal conditions at 298K. Near wall gas temperature approaches zero due to zero gas density near the walls.

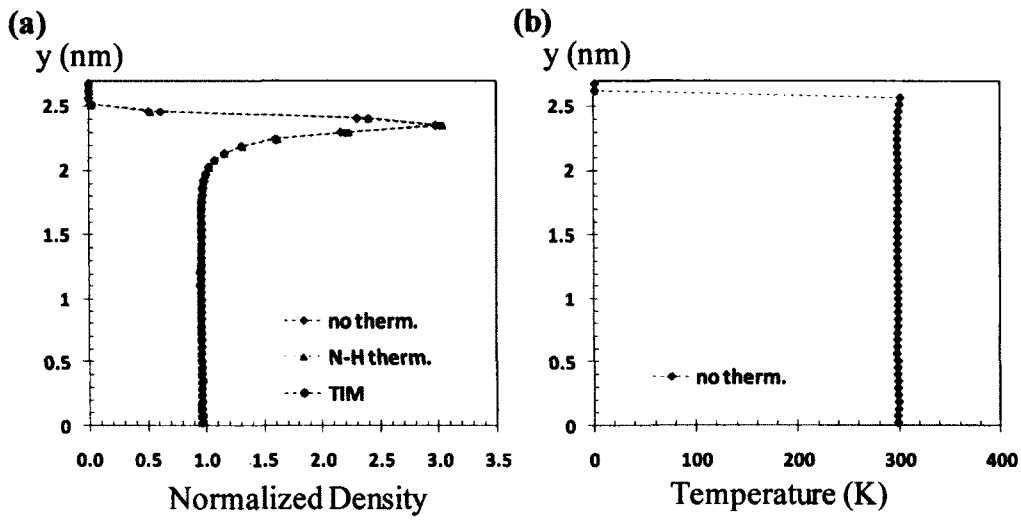

Figure 3.3 (a) Normalized density distribution of the dilute gas case obtained using different thermostat techniques (N-H therm: Nose-Hoover thermostat, TIM: thermally interacting wall). (b) Simulations were performed for average density of 0.0286 #/nm^3. Results for ε_{wf}=1 are shown. Temperature distribution verifies isothermal conditions at 298K.

Density variations within the nano-channel are induced by the wall force field. It is important to investigate the effects of these force fields within the perspective of normal stresses, which can be eventually related to pressure within this simple compressible system. Figure 3.4 shows the distribution of three mutually orthogonal components of normal stresses within the nano-channel. As stated earlier, the off-diagonal terms of the stress tensor is zero. Therefore, these normal stresses correspond to the principle stresses, and they are acting in three mutually orthogonal directions that coincide with the directions of the Cartesian coordinate system used in this study.

Specifically, the channel length and width are in x- and z-directions, while the channel height is in y-direction. Therefore, S_{xx}, S_{yy} and S_{zz} are the normal stresses at a point that act in the x-, y-, and z-directions, respectively. I have utilized Equation (13) to calculate the stresses. Particularly, I distinguish between the kinetic and virial parts of Equation (13), which are shown in Figures 3.4 (a) and (b), respectively, while Figure 3.4 (c) shows the total normal stresses as the sum of the kinetic and virial components. The virial term is often dominant for liquids, while the kinetic term is more dominant for gas flows, as suggested by Irving and Kirkwood (Irving and Kirkwood 1950). My calculations have shown that the contribution of the virial component in the bulk region (i.e., outside the wall force field cut-off distance, which is approximately $y \leq 1.7$nm in the figures) is less than 0.05 percent of the resulting normal stress. In fact, the normal stresses due to the kinetic terms in Equation (13) are isotropic in the entire channel, and variation of the kinetic part of the normal stresses shown in Figure 3.4 (a) are similar to the density variations shown in Figure 3.3 (a) under isothermal conditions. In the bulk portion of the channel ($y \leq 1.7$ nm), pressure can be calculated as the average of the three normal stress components ($P = \frac{S_{xx} + S_{yy} + S_{zz}}{3}$), and the pressure field predicted using the computed density and temperature within the ideal gas law matches the computed pressure distribution exactly. This is an expected behavior, as explained earlier in Section 2.

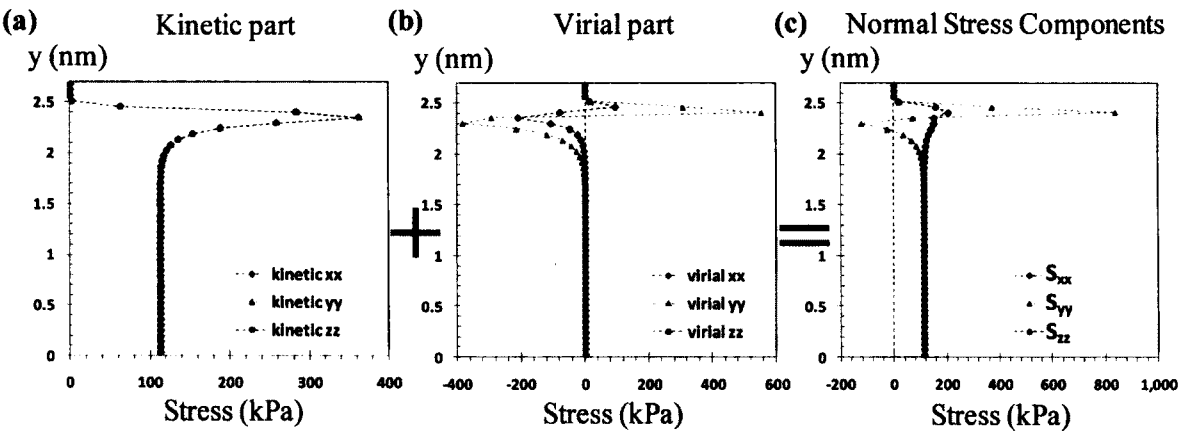

Figure 3.4 (a) Kinetic and (b) virial components of (c) the normal stress distribution for the dilute gas case.

Virial terms in the bulk region are isotropic, and their contribution to pressure is negligible. However, this is not the case in the near wall region, as can be seen from Figure 3.4(b), where the surface virial effects induce anisotropy and significant deviations from the ideal gas behavior in the near wall region. Different than the bulk portion, virial term dominates the normal stress distribution inside the force penetration depth. Behavior of the virial terms is rather sensitive to the net force field and local density changes, and affected by the particle-particle and particle-wall interactions. The virial terms in x- and z-directions are identical, while the virial in y-direction (i.e., normal to the wall) shows significant deviations from the previous two components.

Figure 3.5 shows the variations of the yy component of the particle-particle (a) and surface-particle (b) virial terms in y-direction. In the bulk flow region, the particle-particle virial results in weak attractive forces (shown by the negative stress values in Figure 3.5 (a)). However increase in the gas density near the wall induces local repulsive forces, increasing the particle-particle virial rapidly as a result of the surrounding gas molecules. As the local gas density reaches a peak and starts to decline, the particle-particle virial term starts to decrease. The surface virial in the y-direction is shown in Figure 3.5 (b). Although its value is zero in the bulk region, the surface virial becomes dominant in the near wall region, overwhelming both the particle-particle virial and kinetic terms. The surface virial variation is non-monotonic. In order to understand its behavior, I present in Figure 3.6 the surface virial part of S_{yy} as a function of the distance from the wall. The figure also includes the gas density variation within one nano-meter from the wall, and the potential and force fields induced by the *entire* FCC wall onto a single molecule approaching normally to the surface through the centerline of a wall molecule (also represented in the figure). The value of the surface virial is in kPa, and should be read from the left ordinate (Axis a), while the gas density, wall potential and force fields are normalized by the values stated in the figure caption, and their values should be read from the right ordinate (Axis b) in non-dimensional form. Keeping in mind that the potential and force fields in the figure are the result of the *entire wall structure*, I first discuss the density distribution near the surface, which exhibits its peak value at the potential minimum. After this minimum, the potential increases exponentially and hence, the density profile converges to zero. One may expect observing

infinite potential and zero density one molecular diameter distance from the wall by simply considering the L-J potential. However, the molecular corrugations due to the structure of FCC walls allow some gas molecules penetrate into the one molecular diameter region, resulting in gradual convergence of density distribution to zero.

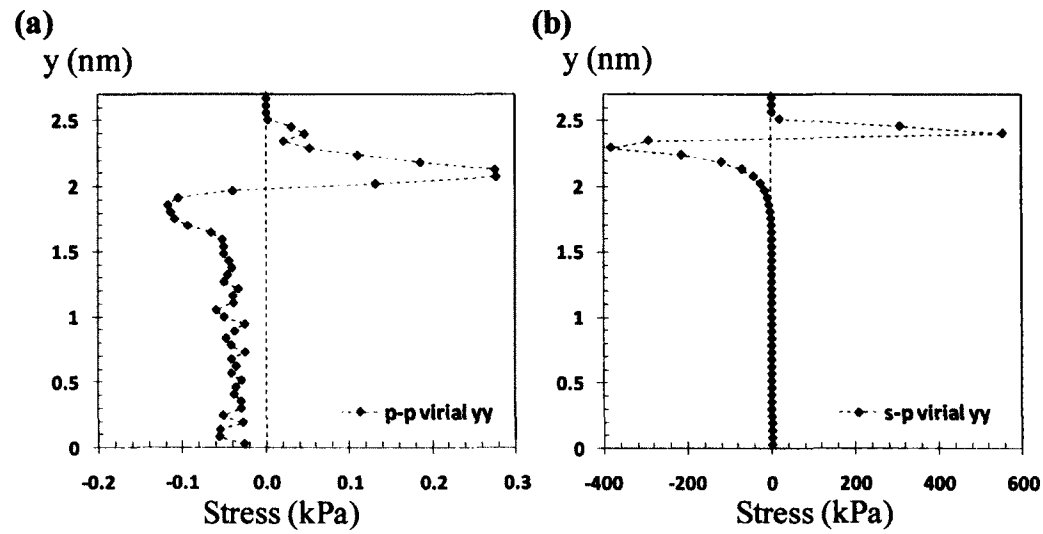

Figure 3.5 Variation of the yy component of (a) the particle-particle and (b) surface-particle virial terms within half of the nano-channel for the dilute gas case.

As the gradient of a scalar potential, the force field in the normal direction to the wall is also plotted in Figure 3.6. The normal force reaches zero at the potential minimum, as indicated by the vertical dashed line at y ≈ 0.36nm. The negative and positive force values show attractive and repulsive behaviors, respectively. The surface virial in the y-direction is negative through the attractive portion of the wall potential. The surface virial decreases up to the zero force point, after which, the surface force becomes repulsive, and the surface virial starts increasing rapidly towards the wall. However, this increase is limited and finally overwhelmed by the decrease in the density of gas molecules near the surface. As a result, the surface virial terms decrease and converge to zero. Overall, the variation in surface virial is a function of the wall force field as well as the local gas density. I investigated the surface virial behavior for different gas/wall interaction strength ratios (ε_{wf}), which has shown similar behavior to

the results depicted in Figure 3.6 with an approximately linear increase in the magnitude of the virial terms with increased ε_{wf} ratio (Results are not shown for brevity).

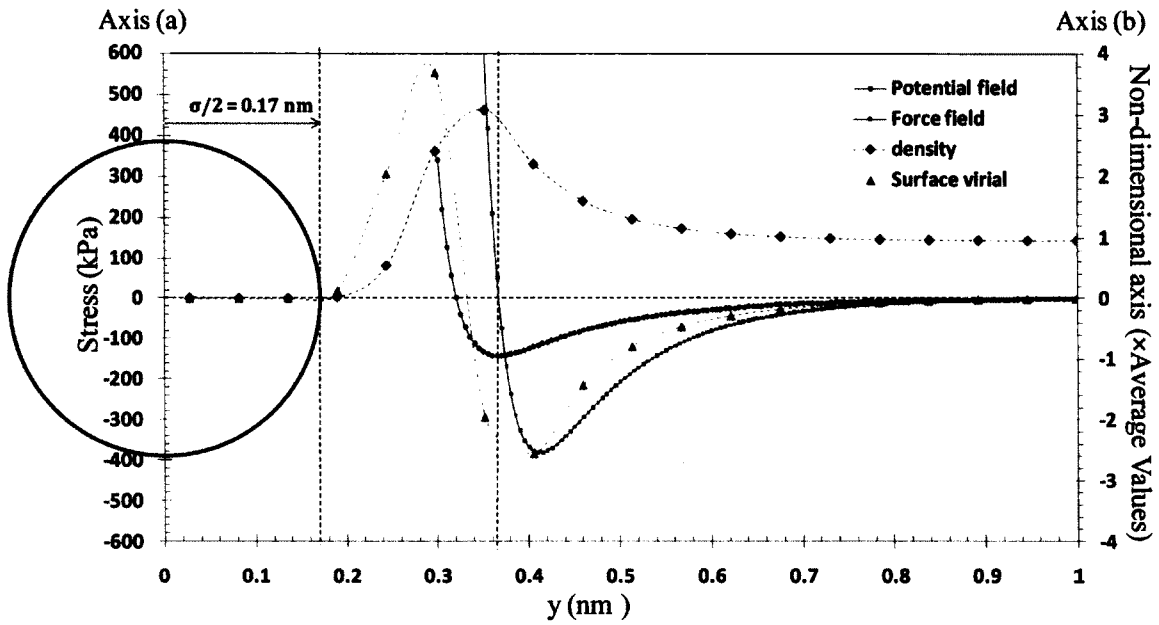

Figure 3.6 Spatial variation of the surface virial (left ordinate), gas density, wall potential and force fields (right ordinate) in the near wall region. The density, potential and force terms are normalized by 0.0286#/nm^3, -0.205×10^{-20}kg m^2/s^2 and 2.034×10^{-20}N, respectively. The potential and force fields induced by the entire FCC wall onto a single molecule approaching normally to the surface through the centerline of a wall molecule is shown. A representation of the wall molecule is also included.

The number of argon molecules in the channel under various gas/wall interaction strength ratios (ε_{wf}) is shown in Figure 3.7. The near wall gas density increases with increasing the gas/wall interaction strength ratio, which leads to gradual decrease of the number of gas molecules in the bulk region. An increased residence time for gas molecules within the force penetration region is observed. For the ε_{wf}= 3 case, more than 360 of 450 molecules are mostly like to spend time in the near wall region at a given instant. However, identity of these gas molecules can still change by time. Therefore some molecules are able to leave the surface force field and continue their free flight

towards the opposing surface. Further increase of the wall strength results in adsorption of argon on the surfaces with bulk region being depleted from gas molecules.

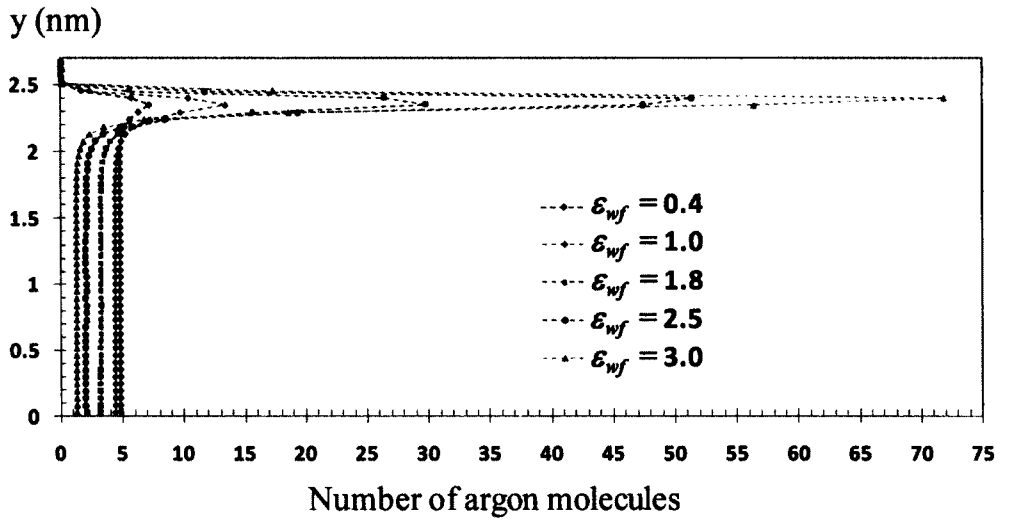

Figure 3.7 Number of argon molecules across the nano-channel obtained for different gas/wall interaction strength ratios (ε_{wf}).

Variations of the xx and yy components of normal stresses in the nano-channels are shown in Figure 3.8 for different gas/wall interaction strength ratio (ε_{wf}) values. The stress profiles are normalized using the channel center pressure values of 126.1kPa, 113kPa, and 83.9kPa, for the ε_{wf} = 0.4, 1.0, and 1.8 cases, respectively. Kinetic parts of stress profiles are proportional to the density distributions, and match ideal gas predictions in the bulk region. Increase in the ε_{wf} results in stronger surface-particle interactions, and hence, the surface virial become more dominant. Figure 3.8(b) illustrates the yy-component of normal stress for different ε_{wf} values. Trends in this figure are similar for all ε_{wf} cases. However, the magnitude of the stress increases with increased ε_{wf}. Surface-particle virial is dominant within the wall force field penetration depth, initially inducing an attractive force (negative stress values) followed by strong repulsion (positive stress values). In Figure 3.8(a), sudden variations in the xx-component of normal stresses for the ε_{wf}=1.8 case is due to the negative surface-particle virial becoming

more dominant than the positive kinetic component. Local variations of the kinetic and virial components of these stresses are not shown for brevity.

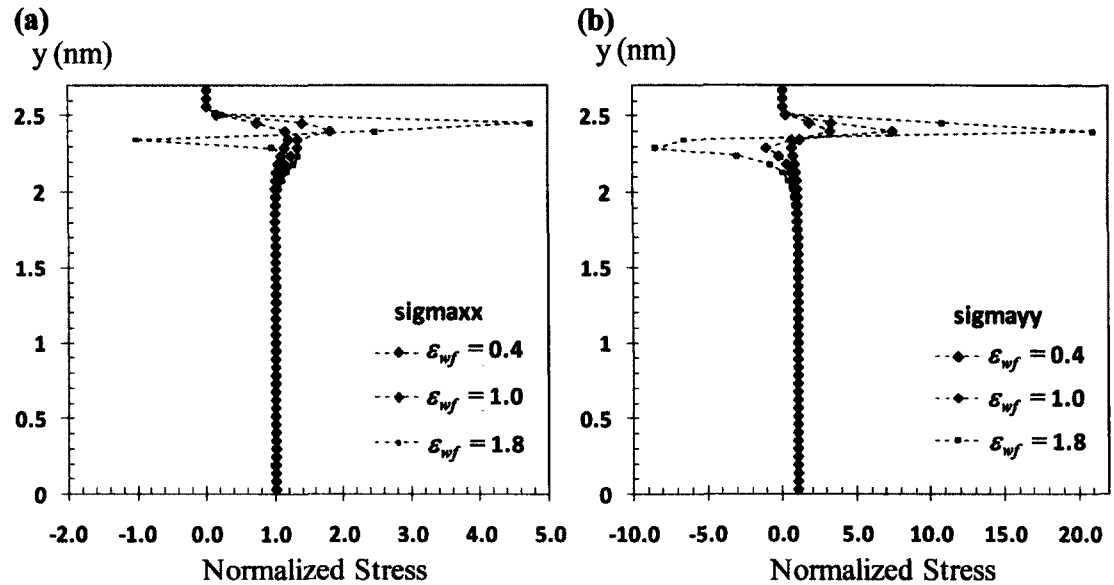

Figure 3.8 Variations of (a) the xx and (b) yy components of the normal stress in the nano-channel for different gas/wall interaction strength ratios (ε_{wf}). The stresses are normalized using the bulk pressure values of 126.1kPa, 113kPa, and 83.9kPa for the ε_{wf} = 0.4, 1.0, and 1.8 cases, respectively.

3.3.2 Dense Gas

In order to predict the correct thermodynamic state of dense argon gas, a series of dense gas simulations were performed in periodic domains spanning $\lambda \times \lambda \times \lambda$, where λ is the local mean free path. The density and temperature of argon gas were selected at various states identified in Table 3.2, and computed pressure using Equation (13). Different cut-off distances were utilized for intermolecular forces in pressure computations. Increasing the cut-off distance from 1.08nm to 2.7nm results in better agreements between the MD and pressure values tabulated in (Sonntag and Borgnakke 2002). The compressibility factor Z ($=P/\rho RT$) was also computed, which shows deviations from the ideal gas law. Thus, (1-Z) shows relative importance of the particle-

particle virial terms in Equation (13). An example of a compressed liquid state of argon is also computed. Pressure of the liquid was successfully predicted using a cut-off distance of 2.16nm. Using shorter cut-off distance in L-J interactions neglects weakly attractive forces between the molecules. As a result, the thermodynamic pressure is consistently over predicted. Effects of using short cut-off distances in MD calculations were studied earlier in (Mecke et al. 1997; Guo and Lu 1997).

Dense argon gas is studied at 180K and 593.16kg/m^3 (number density of 8.94#/nm^3) by simulating 352 argon molecules in a nano-channel of 5.4 nm in height, and 2.7 nm in length and width (See Table 3.1). MD simulations are performed using the L-J force cut-off distance of 2.7nm. Mean free path of argon at this state is 0.173nm and the mean molecular spacing is 0.482nm. The ratio of mean molecular spacing to molecular diameter is 1.42, which corresponds to a dense gas state. Local thermodynamic pressure is 11.62MPa and the compressibility factor Z=0.52 (See Table 3.3). Periodic boundary conditions are applied along the channel length and width. Figure 3.2 (b) shows a snapshot of the computational domain for the ε_{wf}=1 case.

Table 3.3 Comparison of MD calculated pressure values with the thermodynamic state in nano-scale confinements.

State	r_c (nm)	ρ^{-1} (m^3/kg)	T (K)	P_{table} (kPa)	P_{MD} (kPa)	Error %	$P_{ideal\ gas}$ (kPa)	Z_{table}
Dilute Gas	1.08	0.5494	298	113	113	0	113	1
Dense Gas	2.7	0.00168	180.2	11,620	10,926	-5.98	22,166	0.52
Comp. Liquid	2.7	0.0007065	124.8	80,840	86,000	6.4	-	-

Density distributions in the nano-channel obtained using the Nose-Hoover thermostat, interactive thermal wall model, and without using a thermostat are shown in Figure 3.9. Density profile obtained using 1.08nm force cut-off distance is also shown in the figure. The near surface gas density is larger than the bulk density. Unlike the dilute gas case with a single density peak, I now observe a dominant second density peak and a much weaker third density peak, indicating the onset of density layering effects.

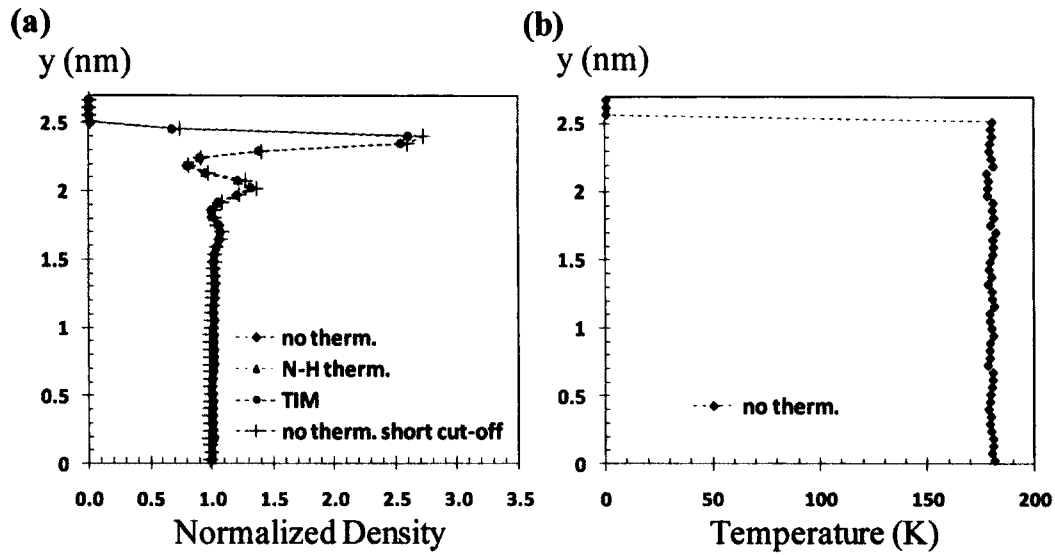

Figure 3.9 (a) Normalized density distribution of the dense gas case obtained using different thermostat techniques. (b) Simulations were performed for average density of 8.94#/nm^3. Results for ε_{wf}=1 are shown. Temperature distribution verifies isothermal conditions at 180K.

Figure 3.10(c) shows the distributions of the normal stress components along with their kinetic (a) and virial (b) contributions. I first examine the stress distribution in the bulk of the channel (y≤1.5nm), where the surface-particle virial effects are zero. Away from the walls, the particle-particle virial contribution is -11.24MPa. Negative sign of the normal stresses show attractive forces on the molecules. At this state the mean molecular spacing is 0.482nm, where the L-J force interactions are attractive. The kinetic part of the normal stresses is isotropic, and reaches 22.166MPa in the bulk of the channel. Combination of the positive kinetic components of normal stresses with the negative particle-particle virial components result in local pressure of 10.926MPa, a value 6% lower than the thermodynamic pressure of 11.620MPa (Sonntag and Borgnakke 2002). Different than the bulk region, virial terms dominate the near wall stress distribution with anisotropic behavior similar to that discussed for the dilute gas state. Non-monotonic variation of the surface-particle virial is similar to the dilute gas case shown earlier in Figure 3.5. However the minimum and maximum values of the surface-particle virial are now -100MPa to 80MPa, respectively. Overall, the dense gas state acts as a transition between the dilute gas and liquid cases. Therefore, further discussions will be given in the

liquid results. Higher ε_{wf} cases, not shown for brevity of my discussions, resulted in higher surface virial magnitudes with almost linear increase in their magnitude.

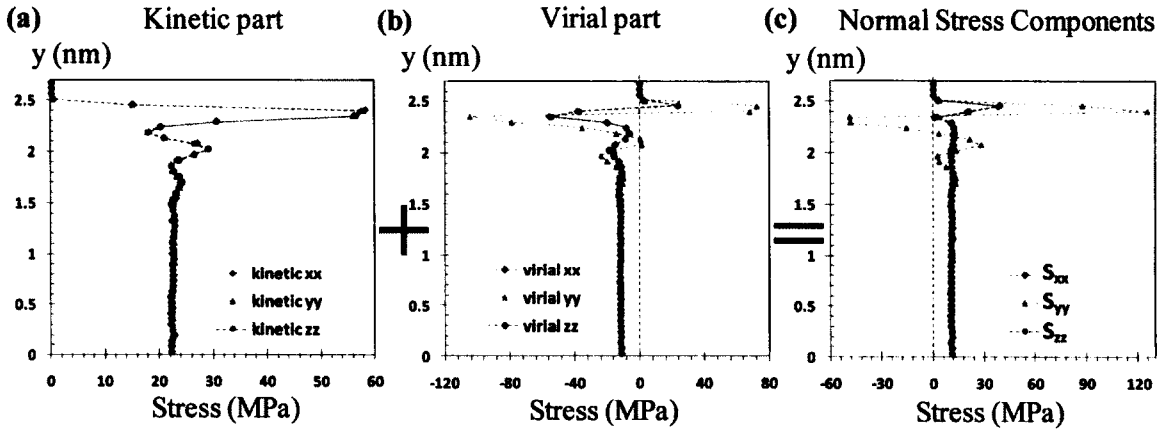

Figure 3.10 (a) Kinetic and (b) virial components of (c) the normal stress distribution for the dense gas case.

3.3.3 Liquid

Liquid argon at 125K and 1349.8kg/m^3 is studied inside a nano-channel of 5.4nm in height, and 2.7nm in length and width. Figure 3.2 (c) illustrates a snapshot of the computational domain for the ε_{wf} =1 case. Periodic boundary conditions are imposed along the channel length and width. The simulation contains 801 argon molecules with a resulting number density of 20.35#/nm^3. The mean molecular spacing is 0.366nm, which is comparable with the molecular diameter of argon.

Density distributions obtained using the Nose-Hoover thermostat, interactive thermal wall model and without using a thermostat give identical results under isothermal conditions at 125K (Figures 3.11 (a), (b)). Density distributions obtained using 1.08nm and 2.7nm cut-off distances (r_c) for intermolecular force interactions are also shown in the figure. Density distribution is not affected by r_c. Similar with the previous researchers, multiple density layering is observed on the surface. In the direction normal to the interface, liquid density profiles exhibit oscillatory behavior on the *molecular scale* due to the interactions between the liquid and solid molecules. The magnitude of the

density layering increases with increasing the solid–liquid interaction strength ratio (ε_{wf}). Detailed investigation of density for different epsilon ratios can be found in (Li et al. 2010; Thompson and Troian 1997; Cieplak et al. 2001; Cieplak et al. 1999). Ordering of the liquid extends wall effects more into the bulk portion of the channel, compared with the gas cases. This dominant behavior at the solid–liquid interface has a major effect on the mechanical properties.

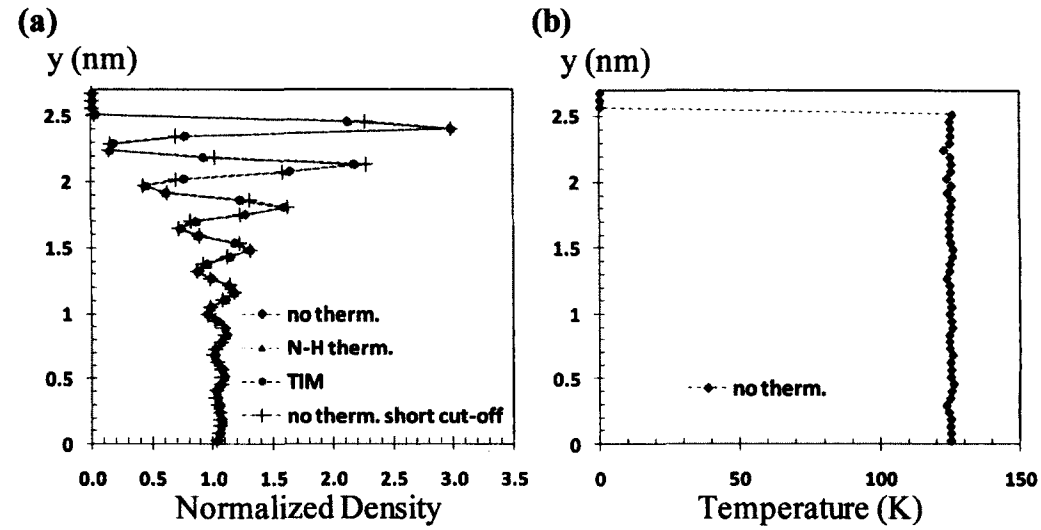

Figure 3.11 (a) Normalized density distribution of the liquid case with different thermostat techniques and using L-J force cut-off distances of r_c=1.08nm and 2.7nm. (b) Simulations were performed for average density of 20.35#/nm^3. Temperature distribution verifies isothermal conditions at 125K.

Stress tensor computations were performed using an L-J force cut-off distance of 1.08nm and 2.7nm. Kinetic components of the stresses (proportional to the density variation via the ideal gas law) were unaffected from the use of the shorter cut-off distance. However, the virial contributions of the stress tensor were overestimated due to the negligence of the long-range weakly attractive interaction forces (results not show for brevity). In the following, I only show the results obtained using the cut-off distance of 2.7nm.

Normal stress distribution in liquid argon interacting with walls at ε_{wf}=1 is shown in Figure 3.12 (c) along with the contributions of their kinetic (a) and virial (b) components. Oscillatory behavior of normal stresses arising from the density layering is apparent in the results. The normal stresses are anisotropic. Specifically, S_{yy} behaves differently than S_{xx} and S_{zz}. Similar to the gas cases, the stress tensor is diagonal. Therefore, the stresses shown in the figure correspond to the principle stresses on the liquid, and *x*-, *y*-, and *z*-directions correspond to the principle directions. There is a small region near the channel center having constant and equal normal stresses (i.e., pressure) at 86 MPa. This isotropic region would be bigger in a larger channel. The MD calculated pressure is about 6.4% larger than the tabulated value of 80.84MPa (See Table 3.3 for further details). It is worth to mention that addition of a single molecule to this nano-scale system induces 0.125 % variation in the liquid density, which increases the pressure by 1.34%. As expected from a compressed liquid state, small variations in the liquid density (at constant temperature) induce large changes in pressure; and discrete nature of the nano-scale system (i.e., limited volume and finite number of molecules) can induce large fluctuations in the calculated thermodynamic state. In the bulk region of the channel, the kinetic and virial contributions of pressure are the same order of magnitude. Specifically, the kinetic and virial components of stresses at the channel center are 37.54MPa and 48.46MPa, respectively. The kinetic part of normal stresses is isotropic, and obeys the ideal gas law. Since temperature is a constant, kinetic component of the normal stresses show fluctuations similar to the fluid density. The virial part of the normal stresses are positive in the bulk of the channel, indicating repulsion between the molecules. The reason of this repulsive force is that the liquid argon molecules at this state are at a mean molecular spacing of 0.366nm, where the intermolecular forces for the L-J potential are repulsive. As shown in Figure 3.12 (b), the virial terms become dominant in the near wall region and their behavior are sensitive to the net force field and local density changes. The virial in y-direction shows significant deviations from the x- and z-components. Different than the gas cases, anisotropic nature of normal stress distribution extends beyond the surface force penetration depth of 3σ. The reason of this behavior is the density layering, which induces anisotropic normal stresses due to the particle-particle virial terms in Equation (13).

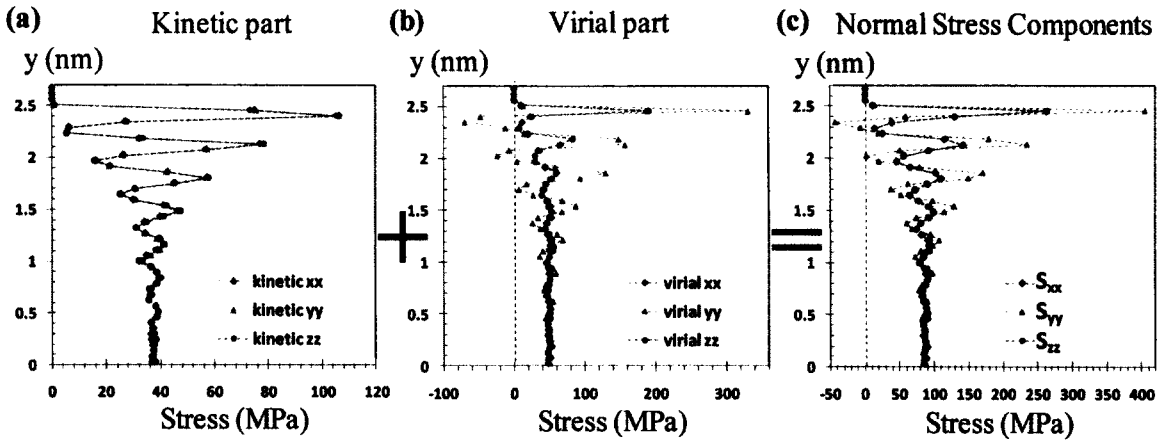

Figure 3.12 (a) Kinetic and (b) virial components of (c) the normal stress distribution for the liquid case.

Figure 3.13 shows the variations of the yy component of the particle-particle (a) and surface-particle (b) virial terms in y-direction. The particle-particle virial has strong influence of the density layering. It has oscillatory positive stress values showing mostly strong repulsive forces in the bulk region. Decrease of the intermolecular distances inside the compact density layers of the near wall region induces stronger local repulsive forces between the molecules that can be observed as increased positive virial values. At density values smaller than the mean liquid density, the intermolecular spacing between the fluid layers is increased and the particle-particle interaction may become weakly attractive if the local molecular spacing increases beyond 0.3822nm (i.e., the distance between two molecules, when the L-J force switches sign). These effects decrease the particle-particle virial. Figure 3.13 (b) shows variation of the surface virial in y-direction. Surface virial effects overwhelm both the particle-particle virial and kinetic terms inside the force penetration depth before it converges to zero around the L-J cut-off distance.

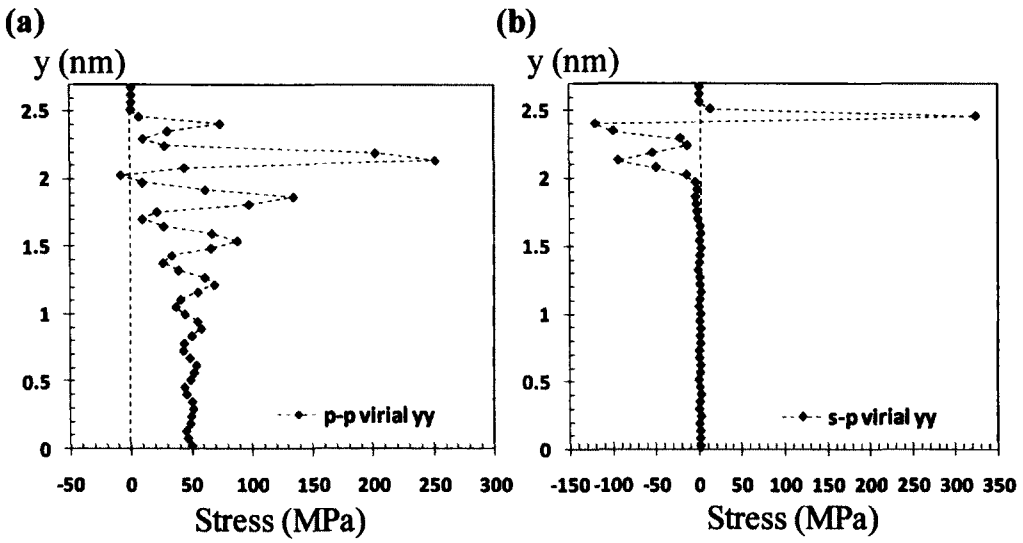

Figure 3.13 Variation of the yy component of (a) the particle-particle and (b) surface-particle virial terms within half of the nano-channel for the liquid case.

Variation of the yy component of the surface-particle and particle-particle virial terms (Axis a) and the normalized density distribution (Axis b) inside a region 2nm from the wall are shown in Figure 3.14. Unlike the ideal gas case, potential variation induced by the entire FCC wall onto a single molecule approaching normally to the surface cannot represent the potential distribution inside the channel anymore. Variations of the particle-particle and surface-particle virial terms in the near wall region are affected by the density profile. In the figure, the fluid density is normalized using the averaged density at which the mean molecular spacing is equal to 0.366nm. Ratio of this value to the distance where the L-J force switches sign (0.3822nm) is 0.96. A horizontal dashed line was included to the normalized density profile in the figure to indicate the density values below which the intermolecular force between the two atoms become weakly attractive. Local density fluctuations in the figure can be correlated with variations in the particle-particle virial terms. When the local (normalized) density is reduced below 0.96, the local particle-particle virial tends to decrease. The surface-particle virial exhibits two negative peak points within $0.3\text{nm} < y < 0.7\text{nm}$ due to the locally attractive forces between the two near surface density layers and solid. Closer to the wall, the net force induced by wall molecules on the fluid becomes repulsive, and hence, the surface-particle virial suddenly switches sign and becomes positive.

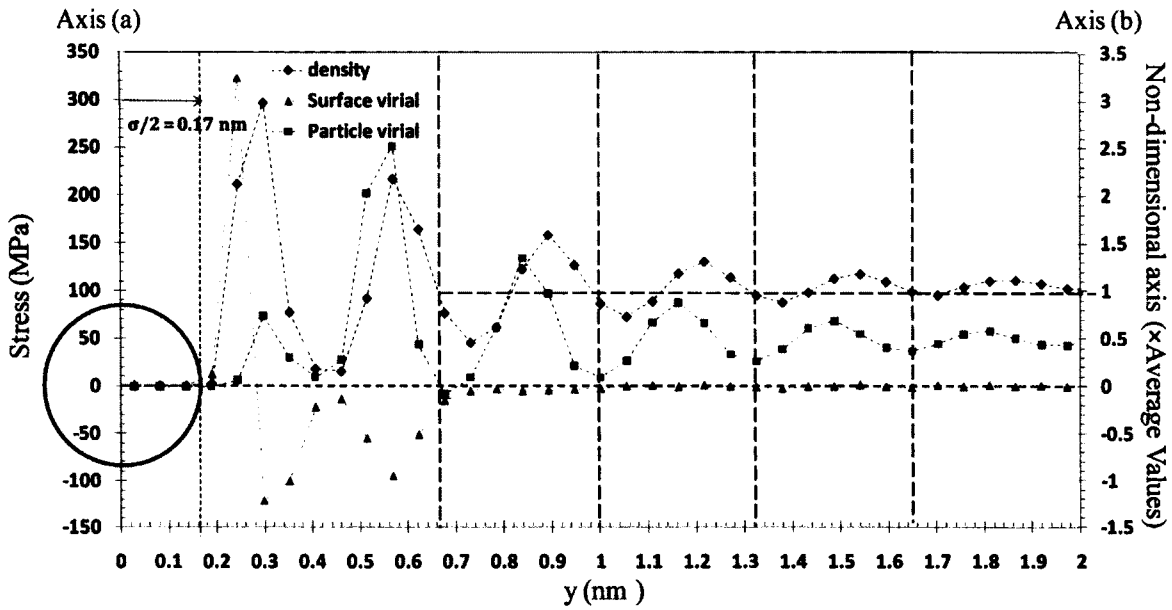

Figure 3.14 Variation of the yy component of the surface-particle and particle-particle virial terms (Axis a) and the normalized density (×20.35#/nm^3) distribution (Axis b) near the wall.

3.4 Summary

Prediction of stresses using the Irving-Kirkwood method can be greatly affected by long-range force field interactions between the molecules. Using various cut-off distances, I calculated the normal stresses (pressure) for argon gas and liquid within periodic domains, and verified the results using published thermodynamic states. Regardless of the fluid's state, kinetic parts of the normal stresses capture the ideal gas law, while corrections to pressure are induced by the virial components. Within a periodic domain, free of solid boundaries, fluid molecules experience particle-particle virial effects. If the force-field induced by the mean-molecular spacing at a given density is attractive, the particle-particle virial becomes negative. The virial terms become positive for molecular separations (i.e., densities) that lead to repulsion. I have observed that using 1.08nm cut-off distance in Lennard-Jones force calculations can induce significant errors in prediction of the thermodynamic state for dense gas and liquids. However, utilization of 2.7nm cut-off distance resulted in reliable pressure predictions, despite the 244 ($\approx 2.5^6$) fold increase in the computational cost. Neglection of the weakly attractive interaction forces due to the use of small cut-off distances in MD result in over-

prediction of the local pressure, which is a numerical artifact relevant to the virial calculations only.

Density buildup with a single peak is observed for the dilute gas confined within a nano-channel. The normal stresses are anisotropic within the force-field penetration region, which extends approximately 1.08nm from each wall. Beyond this distance, the ideal gas law is valid and the density is uniform in the channel. Simulations performed at different gas/wall interaction strength ratios (ε_{wf}) show more distinct density buildup near the wall with almost linear increase in the magnitude of the surface-particle virial effects. Dense gas case exhibited onset of density layering effects. Anisotropic normal stresses are observed approximately 1.2nm from each wall. Beyond this distance, pressure reached its thermodynamic value. The liquid case shows well known density layering effects with anisotropic normal stresses penetrating over 2nm from each wall. In the bulk of the channel thermodynamic pressure is reached. In addition to the kinetic part of the normal stress tensor being isotropic and be able to recover the ideal gas law, my observations show that:

1) Wall force field induces anisotropic normal stresses on the fluid by the surface-particle virial terms, which becomes zero beyond the wall force-field penetration depth.
2) An additional wall effect is due to the density layering induced by the wall force field, where the particle-particle virial terms induce further anisotropy that protrudes beyond the wall force penetration distance. This effect becomes more dominant in liquids as a result of strong density layering.

Due to the anisotropic normal stress distribution, it is impossible to define pressure in the near wall region of nano-scale confined fluids. I expect these observations to be valid for flow cases, which will be presented in the following chapters.

CHAPTER 4

MOLECULAR DYNAMICS SIMULATIONS OF SHEAR DRIVEN GAS FLOWS

Analysis of fluid behavior near a surface requires proper investigations of the wall force field effects. This can be achieved either utilizing simplified wall potential models that ignore the atomic structure of surfaces (Steele 1973), or via three-dimensional molecular dynamics (MD) simulations. Inside the wall force penetration depth, solid surface induces body forces on fluid molecules, which result in surface induced stresses. Stresses generated by the surface-particle interactions are identified as the "surface virial". The previous chapter was focused on the stress variations in gas, dense gas and liquid argon confined in stationary nano-channels, where the "surface virial" created anisotropic normal stresses for dilute and dense gas phases while the normal stresses became isotropic and recovered the thermodynamic pressure sufficiently away from the surfaces (Barisik and Beskok 2011). These previous studies were performed in stationary channels and employed equilibrium MD simulations. As a result, they did not focus on flow and tangential momentum exchange of gas molecules with walls.

The tangential momentum exchange between a surface and gas can be characterized using the tangential momentum accommodation coefficient, TMAC (α), which was introduced by Maxwell as the fraction of gas molecules reflected diffusively from a solid surface. Specifically $\alpha = 1$ and $\alpha = 0$ correspond to diffuse and specular reflections, respectively. Despite the presence of other scattering kernels, such as the Cercignani-Lampis model (Cercignani and Lampis 1971), most theoretical and numerical research on rarefied gas flows utilizes Maxwell's gas-surface interaction model due to its simplicity. As a result, several experimental and numerical studies were conducted for determination of TMAC. Experimental research ranged from molecular beam experiments to gas flow experiments in the slip and early transition flow regimes (Arkilic et al. 2001; Bentz et al. 1997, 2001; Goodman and Wachman 1976; Gronych et al. 2004; Rettner 1998; Sazhin et al. 2001), while the numerical research includes MD simulations of single-molecule interactions with crystalline surfaces (Arya et al. 2003; Chirita et al.

1993, 1997; Finger et al. 2007), two- and three-dimensional MD simulations for Kn<1 flows (Cao et al. 2005; Sun and Li 2010, 2011), and coupled MD/DSMC models (Yamamato et al. 2006).

Fluid behavior in the wall-force penetration region depends mostly on the properties of the surface-gas pair. In order to show this, I pick a specific gas-surface pair, and show independency of the near-wall fluid behavior on channel dimensions (H) and flow dynamics (Kn). Therefore, the surface and gas properties, and the surface-gas interaction parameters are kept constant, while the channel height and gas densities are varied to explore and categorize gas flow inside the force penetration depth. MD results are compared with the solutions of the linearized Boltzmann equation in literature (Sone at al. 1990) at various modified Knudsen number (k) values, defined as $k = \sqrt{\pi}/2\, Kn$.

The *objective* of this chapter is to investigate the deviations of nano-scale confined shear-driven gas flows from kinetic theory predictions due to the wall-force field effects. This study shows a universal behavior inside the wall force penetration depth, regardless of the characteristic dimensions of confinement, gas density and the Knudsen number. In order to address this, two different sets of molecular dynamics simulations are conducted. In the first set of simulations, I varied H and density to compare the results of k=10 flow in different height nano-channels, and studied dimensional effects on dynamically similar flow conditions. In the second set of simulations, I varied the channel height and kept the local pressure and temperature constant, and varied k from early transition to free molecular flow regime. Thus, I were able to investigate k dependency of the surface influence. Findings of this research clearly indicate the importance of wall force field effects in nano-scale confinements, mostly neglected in previous gas flow studies.

This chapter is organized as follows: In Section 1, I describe the MD simulation parameters, explain the stress tensor computations and methods utilized in the MD algorithm. In Section 2, I present gas flow results at k=10 and at various k values in two sub sections. Comparisons are made on density, normal stress, shear stress, and velocity profiles for each case. Kinetic and virial contributions of shear stresses are investigated separately, and the importance of surface virial terms is presented. MD predictions of

shear stress and velocity profiles are compared with the kinetic theory calculations, and TMAC values are predicted. Finally, section 3 presents the conclusions of this study.

4.1 Three-Dimensional MD Simulation Details

I consider argon gas flow confined between two infinite plates that are a distance H apart as illustrated in Figure 4.1. Periodic boundary conditions were applied in the axial (x) and lateral (z) directions. Atomistic walls move in opposite directions with a characteristic velocity corresponding to $U_w = M\sqrt{\gamma k_b T/m}$, where M is the Mach number, γ is the adiabatic index (5/3 for monatomic molecules), k_b is the Boltzmann constant (1.3806×10^{-23}J K^{-1}), T is the temperature, and m is the molecular mass of gas molecules. Mass for an argon molecule is $m = 6.63\times10^{-26}$kg, its molecular diameter is σ = 0.3405nm and the depth of the potential well for argon is $\varepsilon = 119.8\times k_b$. For simplicity, the walls have molecular mass and diameter equivalent to argon ($m_{wall} = m_{Ar}$, $\sigma_{wall} = \sigma_{Ar}$) with FCC (face-centered cubic) structure, and (1,0,0) plane faces the gas molecules.

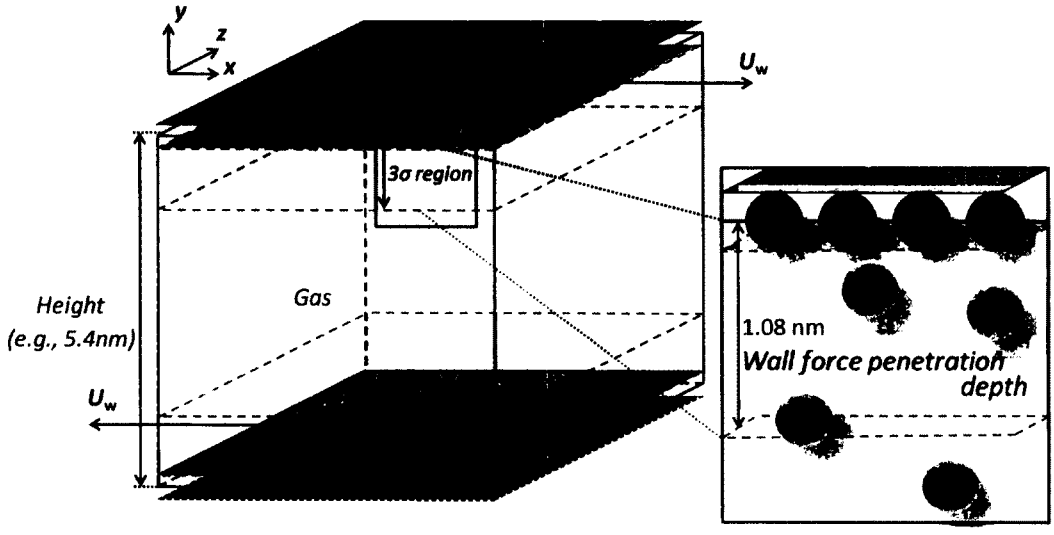

Figure 4.1 Sketch of the simulation domain with explanation of the wall force penetration depth.

Lennard-Jones (L-J) 6-12 potential was utilized to model the van der Waals interactions between gas-gas and gas-wall molecules. In this study, I utilized the potential

strength for gas-wall interactions to be the same with that of gas-gas molecular interactions ($\varepsilon_{wall\text{-}Ar} = \varepsilon_{Ar\text{-}Ar}$). Since the L-J potential vanishes at larger molecular distances, only the interactions with particles within a certain cut-off radius (r_c) need to be calculated. Therefore, the intermolecular interaction forces were truncated and switched to zero at a certain cut-off distance (Allen and Tildesley 1989). In this study I utilized r_c=1.08nm, which is approximately equal to 3.17σ for argon molecules. At this cut-off-distance the attractive part of the LJ potential is reduced to 0.00392ε. My algorithm utilized the well known link cell method to handle particle-particle interactions (Allen and Tildesley 1989).

Table 4.1 MD simulation details for Argon gas at 298K.

$k = \sqrt{\pi}/2\ Kn$	Domain W×H×L (nm)	# Argon Molecules	ρ (#/nm^3)	ρ (kg/m^3)	ρ_{bulk} (#/nm^3)	P_{bulk} (kPa)
k = 10	54×5.4×54	450	0.0286	1.896	0.0275	113.65
	108×10.8×108	1800	0.0143	0.948	0.014	58.07
	162×16.2×162	4050	0.0095	0.632	0.0094	38.93
k = 5	54×10.8×54	900	0.0286	1.896	0.028	115.11
k = 2	54×27×54	1350	0.0286	1.896	0.0283	116.2
k = 1	54×54×54	4500	0.0286	1.896	0.0285	116.56
k = 0.5	54×108×54	9000	0.0286	1.896	0.0285	116.73

Molecular dynamics (MD) simulations in three-dimensional computational domains need to span at least one mean free path per periodic (lateral and axial) direction in order not to affect the gas intermolecular collisions (Barisik et al. 2010). In order to address this limitation, I used the SWMD algorithm to reduce the memory requirement of wall modeling (Barisik et al. 2010). The current SWMD is a fixed lattice model, where the wall molecules are rigid and keep their corresponding FCC positions (i.e., cold wall model). Hence, there is no thermal motion of wall molecules.

Overall the computational domain sizes were chosen according to λ of the simulated gas states. Thus, for the first simulation set of argon gas flow in the free molecular regime, domain sizes of 54nm×5.4nm×54nm, 108nm×10.8nm×108nm, and 162nm×16.2nm×162nm ($\lambda \times H \times \lambda$) were selected at different pressures to render k=10 flow

within different channel sizes. For various k flows at standard conditions, simulations were performed inside 5.4, 10.8, 27, 54 and 108nm height channels with a constant domain span equal to 54nm in length and width. Simulation details can be found in Table 4.1.

Simulations started from the Maxwell-Boltzmann velocity distribution for gas molecules at 298K. Initial particle distribution was evolved 10^6 time-steps (4ns) to reach an isothermal steady state using 4 *fs* (~0.002τ) time steps, after which, 2×10^6 time steps (8 ns) were performed for time averaging. Longer time averaging has also been performed to confirm convergence of the density, stress and velocity profiles to the steady state. Particularly, the simulation times are compared with the mean collision times (predicted by the ratio of the mean free path to the mean thermal speed $c_m = \sqrt{8RT/\pi}$) to result in a state amenable for time or ensemble averaging. In order to capture the property variations within the near wall region accurately and using the same resolution, all simulation domains were divided into equally sized bins of 0.054nm in height in the wall normal direction. As a result, k=10 cases use 100 slab bins, while k=0.5 case utilizes 2,000 slab bins.

I employed the canonical ensemble (NVT, i.e., constant mole, N, volume, V, and temperature, T) by utilizing a thermostat. Initially, Nose-Hoover thermostat (Evans and Hoover 1986) was applied to all fluid molecules at each time step to obtain isothermal condition of 298K with a relaxation time of ~ 0.2*ps*. This resulted in temperature variations in the near wall regions even for very low wall velocities (16m/s, M=0.05), and became more significant for moderate wall speeds of 64m/s (M=*0.2*). Detailed discussions about using Nose-Hoover thermostat for gas simulations are out of scope of this manuscript, and will be presented elsewhere. In order to maintain a constant temperature system in my study, the Nose-Hoover algorithm was employed as a global thermostat inside the local sub-domains. I divided the flow domain into sub-domains having 0.54nm heights through the entire span which is 10 times larger than the utilized bin size. By this way, similar numbers of particles were obtained inside each sub-domain. Thus, each sub-domain had the same Hamiltonian. Applying the global Nose-Hoover thermostat inside each sub-domain was able to maintain constant temperature in the entire flow domain.

Irving-Kirkwood (I-K) expression was utilized to compute the stress tensor components for an N particle system with unity differential operator approximation as given in Equation (13) and (14) (Irving and Kirkwood 1950, Todd et al., 1995).

4.2 Results

In the following, I present two different sets of results. Initially, I present shear driven gas flow in the free molecular regime at k=10 using different size nano-channels at various pressures. This is followed with gas flow at different size channels at fixed pressure and temperature spanning transition and free molecular flow regimes ($0.5 \leq k \leq 10$).

4.2.1 Gas Flows at k=10

I first focus on argon gas flow within 5.4, 10.8, and 16.2nm height channels at 1.896, 0.948, and 0.632kg/m^3 densities, respectively (See Table 4.1). Shear driven flow is obtained by moving the top and bottom channel walls in opposite directions at the same speed. Density variations at fixed temperature (298K) result in different pressures and mean free path values. As a result, the channel height is varied to obtain k=10 flow at different pressures. Kinetic theory based solutions of these flows are identical and determined by the Knudsen and Mach numbers. My objective is to test the nano-scale confinement effects by varying the channel height at a fixed k value. Figure 4.2 shows snapshots of the simulation domains. Gas molecules are shown in green, while presence of a gas molecule within the wall force penetration region requires utilization of the smart wall stencil on the surface, shown in blue and black on the bottom and top surfaces of the channel, respectively.

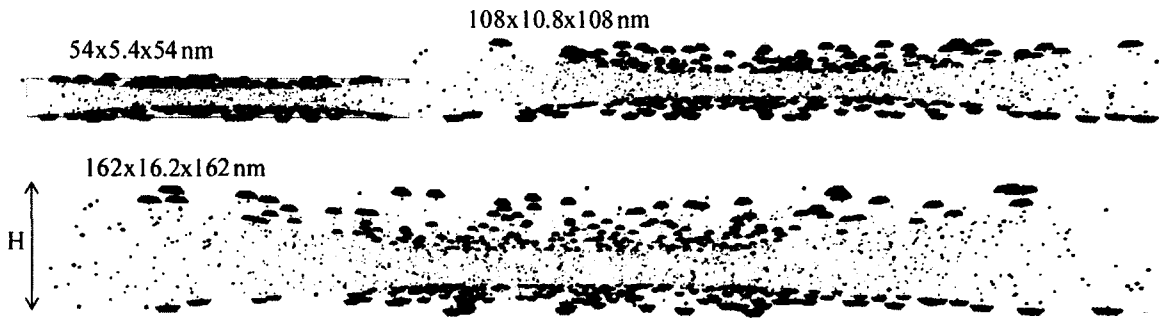

Figure 4.2 Snapshots of 5.4, 10.8, and 16.2nm height channel simulation domains at k=10.

Density distributions are plotted in Figure 4.3 (a) within 2nm distance from the top wall of each channel. Density is a constant in the bulk of the channels while near surface regions have density buildup with a single peak point. This density increase is due to the wall force field, which induces increased particle residence time inside the force penetration depth. In particular, density starts to deviate from its bulk value around 2.5σ from the wall. For the H=5.4nm case, the near wall density buildup decreases bulk density to 96.1% of its assigned value. This density reduction is a result of constant number of gas molecules (N) used in MD simulations, which diminishes as the ratio of the wall force penetration depth to channel height decreases. The figure also includes a schematic of the wall and gas molecules, to emphasize the scales involved in the problem. The wall is defined at the center of the first row of wall molecules facing the fluid. As a result, gas molecules cannot penetrate to several bins neighboring the wall, and gas density goes to zero within 0.2nm from the walls.

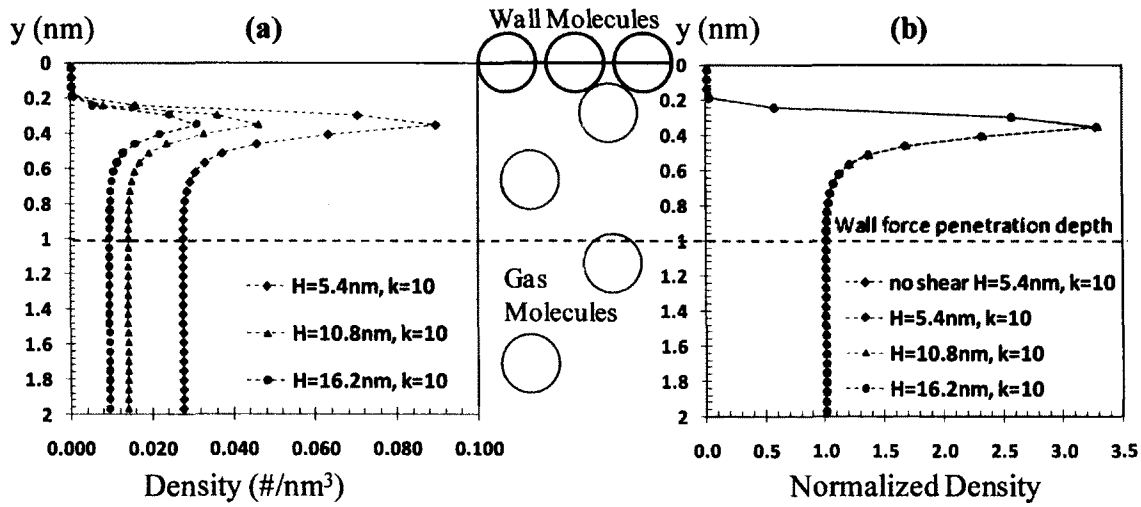

Figure 4.3 (a) Density and (b) normalized density distributions for k=10 flows inside 5.4, 10.8, and 16.2nm height channels at number densities of 0.0286, 0.0143 and 0.0095#/nm^3, respectively. Normalizations are made using the channel center densities of 0.0275, 0.014 and 0.0094#/nm^3. The no-shear case corresponds to thermostat free NVE results obtained in 5.4nm height channel at k=10 and 298K.

Figure 4.3 (b) illustrates the density profiles in 5.4, 10.8, and 16.2nm height channels normalized with the channel center densities of 0.0275, 0.014 and 0.0094#/nm^3, respectively. Although the simulations were at different densities, normalized density profiles are identical. Density profile in a 5.4nm height channel without wall motion (i.e., no-shear) obtained using an NVE system at 298K is also presented for comparison. Identical density profiles validate my present thermostat technique. The density build-up of each case is linearly proportional to the channel center density. Density variation inside the force penetration depth is a result of the wall force field and only depends on the gas-surface interaction properties. It is unaffected by the channel height, flow, and density.

Figure 4.4 shows normal stress profiles for k=10 flows within 2nm distance from the top wall of each channel. The yy-components of the normal stress variations are shown in Figure 4.4 (a). Different densities in different height channels led to different stress values. Normal stresses are constant in the bulk regions and equal to pressure based on the ideal gas law, while the walls induce variations inside the force penetration depth. These variations arise from both kinetic and virial contributions of I-K stress calculations due to the density variations and surface-particle interactions, respectively. Since the gas molecules cannot penetrate to the bins neighboring the wall, stress values reach zero very near the walls (~0.2nm). Figures 4.4 (b) and (c) show the yy- and xx-components of the normal stresses, normalized using the channel center values of 113.65kPa, 58.07kPa and 38.93kPa for the 5.4nm, 10.8nm, and 16.2nm height channels, respectively. Exact match is obtained between the normal stresses in different density domains indicating independency of the wall force field penetration depth behavior to the characteristic dimensions of the domain, gas density, and flow. The normal stress profiles obtained in a stationary (i.e., no-shear) NVE system are also shown in Figures 4.4 (a), (b) and (c). The yy- and xx- components of normal stresses in the no-shear system are identical with the stress profiles obtained for shear driven gas flow. This shows that the normal stresses in shear driven nano-flows are unaffected by the tangential wall motion, as expected. In addition, identical results obtained between the NVE system and the current results validate my present thermostat technique. An important result in Figure 4.4 is that the normal stresses are anisotropic in the wall force field penetration region. In fact, xx- and

zz- components of normal stresses are identical, while the yy-component of normal stress differs due to differences in the surface virial effects. Detailed investigation of normal stress distributions inside stationary nano-scale channels can be found in (Barisik and Beskok 2011).

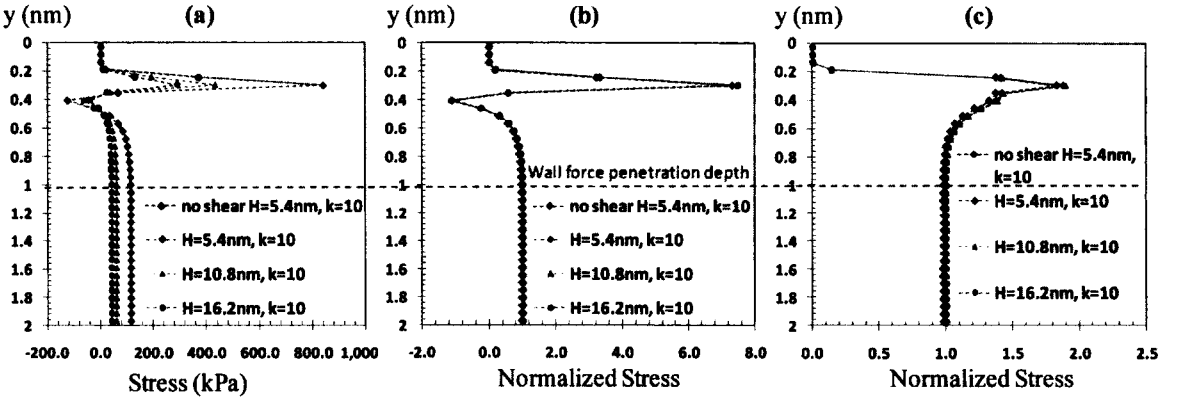

Figure 4.4 (a) Dimensional, and (b) normalized yy-, and (c) normalized xx-components of normal stress distributions of k=10 flows inside 5.4, 10.8, and 16.2nm height channels at 0.0274, 0.014 and 0.0094#/nm^3, respectively. Normalizations are made using the channel center values of 113.65, 58.07 and 38.93kPa. The no-shear case correspond to thermostat free NVE results of 5.4nm height channel at k=10.

Gas velocity profiles normalized with the wall velocity (64m/s) are plotted in Figure 4.5 (a). The velocity components in y- and z-directions have zero average values, confirming one dimensional flow in x-direction (not shown for brevity). I show the velocity profiles within half of the nano-channel. In order to compare the bulk portions of the velocity profile with each other, I present velocity variation as a function of the non dimensional channel height (y/H). The velocity profiles obtained using linearized Boltzmann equation at k=10 subjected to the TMAC (α) values of α=1 and α=0.75 are also presented. The MD based velocity profiles agree well with the kinetic theory predictions adopted from reference (Sone et al. 1990) in the middle of the channels. Better match between the MD results and linearized Boltzmann solutions using TMAC value of α=0.75 is observed for all cases. MD results show sudden changes in the velocity profile within the force penetration depth (i.e., approximately $1nm$ away from each surface). Overlays of this region on flow domains are differently visualized in Figure 4.5

(a) due to the use of different channel heights and utilization of normalized distance (y/H) in the figure. In order to clarify the influence of the wall force field, I zoom on the velocity profiles within 2nm from the top wall in Figure 4.5 (b). Identical velocity variations in the near wall region are observed despite of different shear rates in the bulk region, and different channel heights. Gas velocity increases rapidly within the force penetration region, and suddenly goes to zero on the walls, since the gas molecules cannot penetrate to several bins immediately neighboring the wall. Extrapolation of the velocity profile on to the walls shows reduction in the velocity slip for this particular case, which could be as a result of $\varepsilon_{wall\text{-}Ar}/\varepsilon_{Ar\text{-}Ar}$ =1 used in this study. This is a drastic difference from the linearized Boltzmann equation solutions at different TMAC values, which indicate substantial velocity slip on the walls.

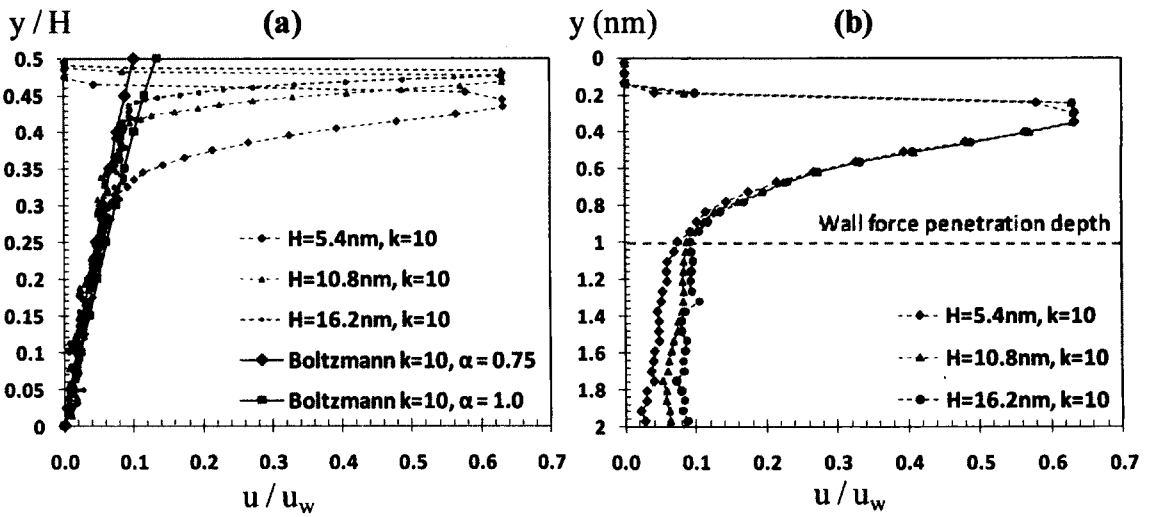

Figure 4.5 Normalized velocity profiles of k=10 flows with constant wall velocity of 64m/s (a) as a function of normalized channel height (y/H), and (b) within 2nm distance from the walls.

Shear stress distributions in the nano-channels are plotted in Figure 4.6 within 2nm distance from the top wall of each case. In Figure 4.6 (a) constant wall velocity of 64m/s (M=0.2) results in various shear rates inside different height channels. Since the channel velocity was kept constant, the shear stresses vary linearly with the shear rate; proving linear stress strain-rate relationship for constant k flows. This and the earlier results on density and normal stress variations show that simulations are in the linear shear response region (i.e., applied shear rate does not induce any non-linear effects).

Shear stress values are constant in the bulk region, while the surface virial induces variations near the walls with single peak points that are linearly proportional to the bulk shear stress values. In order to compare the shear stress profiles at a constant shear rate, wall velocities are adjusted according to the channel heights. Figure 4.6 (b) show shear stress variation in channels moving at M=0.1, 0.2, and 0.3 for the 5.4, 10.8 and 16.2nm height channels, respectively. Shear stress variations within the wall force penetration region in different sized channels at a constant shear rate are identical. This validates linear shear response and linear stress-strain rate relationship for constant k flows inside the nano-confinements.

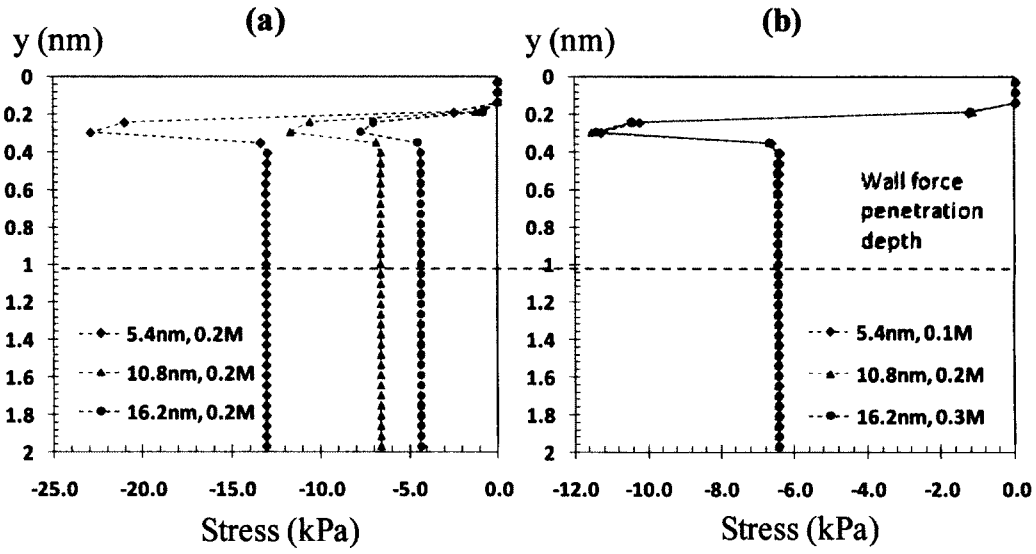

Figure 4.6 Shear stress distributions in 5.4, 10.8 and 16.2nm height channels at k=10 with (a) constant wall velocity of 64m/s (M=0.2), and (b) constant shear rate at M=0.1, 0.2 and 0.3, respectively.

Shear stresses are constant in the bulk of the channels, and show variations within 0.34nm (~σ) from wall. In order to explain the surface force effects on shear stress, I present in Figure 4.7, the shear stress variation within 5.4nm channel as the sum of its kinetic and virial contributions. Shear stress is defined by the kinetic term in most of the domain. Using a similar definition, kinetic theory based solution techniques utilize the kinetic evolution of molecules to calculate shear stresses only by considering particle velocities. The figure shows that the kinetic component of shear stress goes to zero within

approximately σ distance from the wall. However, the surface virial increases starting from one sigma distance from wall till the impenetrable zone for gas molecules where the density diminishes (i.e., 0.2nm ≤ y ≤ 0.34nm). Interestingly, density and density related properties are in a decreasing trend in the same region while the surface virial term peaks. This region, from one sigma distance to zero density, is the main location where the wall and gas molecules interact with strong repulsive forces.

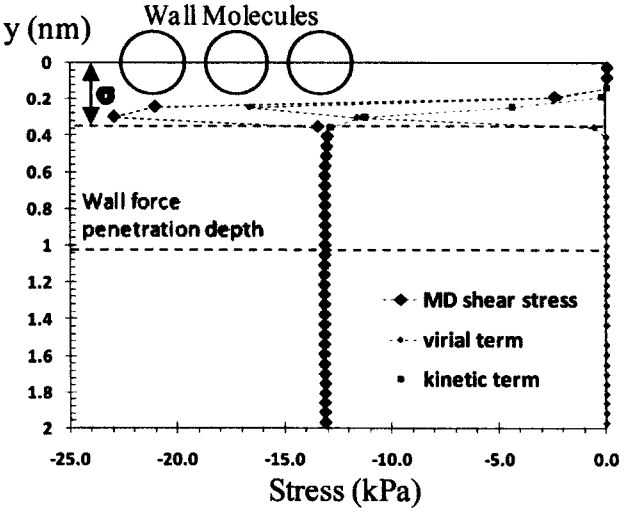

Figure 4.7 Virial and kinetic components of shear stress distribution in 5.4nm height nano-channel at k=10.

Based on the kinetic theory of gases, shear stress for shear driven flow in the free molecular flow regime ($Kn \rightarrow \infty$) can be written as (Shen 2005),

$$\tau_{\infty} = -\frac{\alpha}{2-\alpha}\rho U\sqrt{\frac{RT_w}{2\pi}} \tag{16}$$

where T_w is the wall temperature. The TMAC value can be interpreted as α portion of molecules reflecting diffusively, while and (1-α) portion reflecting specularly. As can be seen, pure specularly reflecting wall will not drive the fluid, and result in zero shear stress, while lower TMAC values will result in lower shear stress. I cannot directly apply Equation (16) to predict the TMAC value for my simulations at k = 10. In order to consider the finite Knudsen number effects I utilized the following correction uniformly valid in the free molecular to slip flow regimes (Bahukudumbi et al. 2003)

$$\frac{\tau}{\tau_\infty} = \frac{0.5297Kn^2 + 1.206Kn}{0.5297Kn^2 + 1.6277Kn + 0.603} \tag{17}$$

Utilizing Equations (16) and (17), I predicted the TMAC value for Argon gas flow confined in different height channels at k=10 to be α=0.75. Theoretical shear stress values calculated for TMAC values of 1.0 and 0.75, and MD results are shown in Figure 4.8 (a) for 5.4nm height channel. This result shows that the atomically smooth FCC wall structures using $\varepsilon_{wall\text{-}Ar}/\varepsilon_{argon\text{-}Ar}$ = 1 does not exhibit full diffusive reflection. My studies with other ε ratios (not shown for brevity) have consistently shown that the TMAC value and shear stress decreases with decreased the $\varepsilon_{wall\text{-}Ar}$ value. I verified the consistency of my shear stress results with the velocity profile. Figure 4.8 (b) shows the kinetic theory prediction of velocity distribution for k = 10 flow at TMAC values of α=1 and α=0.75. I observed that the linearized Boltzmann solution for α=0.75 matches the MD based velocity predictions better than the α=1 case in the bulk flow region. Same approach is conducted on all cases of different channel heights with constant wall velocity or constant shear rate conditions. A constant TMAC value (α=0.75) is found for all cases, independent of the channel height, density, channel velocity, and applied shear rate.

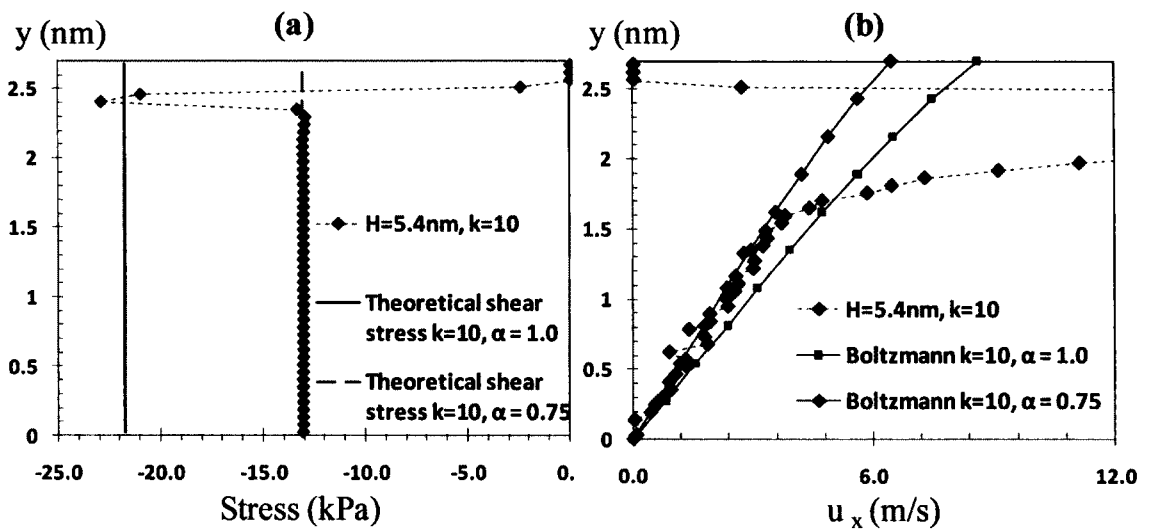

Figure 4.8 (a) MD shear stress profile of 5.4nm height channel at k=10 flow with wall velocity of 64m/s and the corresponding theoretical shear stress results for TMAC values of α = 1.0 and 0.75. (b) A zoomed version of the k=10 flow velocity distributions of MD results and linearized Boltzmann solutions at α=1.0 and 0.75.

4.2.2 Gas Flows at Various k

Shear driven gas flows in nano-channels are investigated in the early transition to free molecular flow regime by simulating argon gas at 298K and 116kPa inside 5.4, 10.8, 27, 54 and 108nm height channels. Simply by changing the channel heights and keeping the domain density constant, I obtained the k=10, 5, 2, 1 and 0.5 flows. Thus, I was able to investigate k dependency of the surface influence from early transition to free molecular flow regimes. Since all simulations are at the same density, λ is constant. Thus, computational domain spans λ in periodic directions for all cases. Figure 4.9 shows the simulation domains for different height channels, corresponding to different k values.

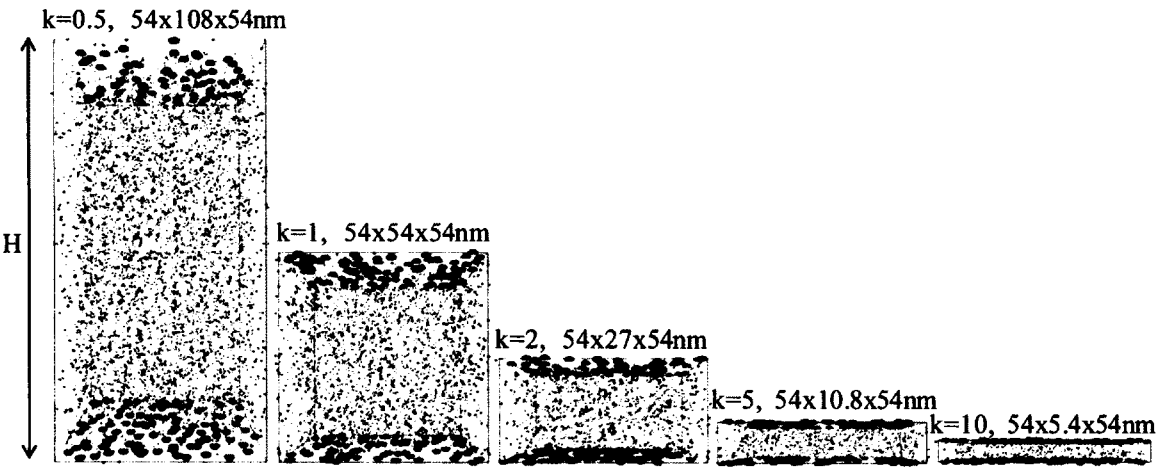

Figure 4.9 Snapshots of simulation domains for argon gas flow inside 5.4, 10.8, 27, 54 and 108nm height channels, corresponding to k=10, 5, 2, 1 and 0.5 flows at 298 K and 116 kPa, respectively.

Figure 4.10 (a) shows density distributions within 2 nm distance from the top wall of each domain. Density is a constant in the bulk region, and increases in the near wall region due to the increased residence time of molecules under the surface effects. For the 5.4nm height channel, bulk density reduces to 96.1 % of its assigned average value due to increased density near the walls. This density reduction in the bulk region vanishes as the channel height increases and becomes negligible for the 108nm case. Density profiles are identical both in the bulk and in the force penetration regions despite different channel heights and k values.

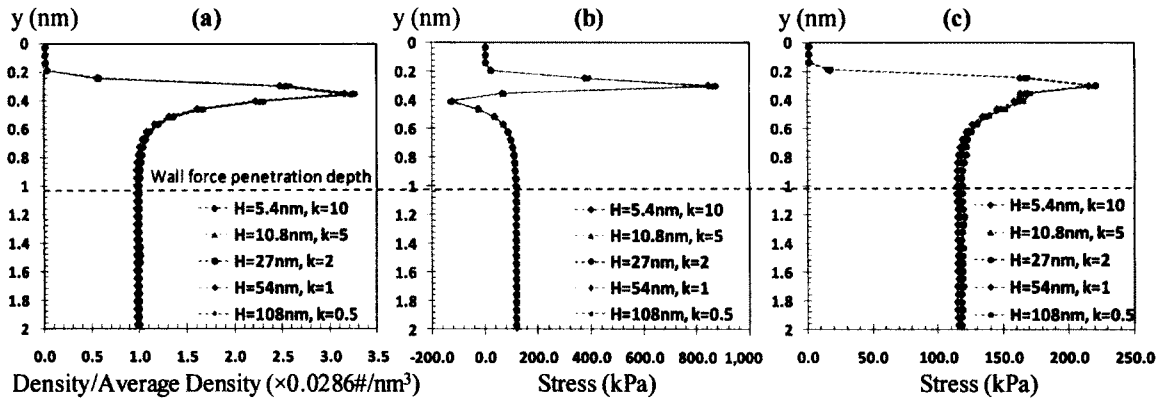

Figure 4.10 (a) Density distribution, and (b) the yy- and (c) xx- components of normal stresses within 2nm distance from wall for different k values.

The yy- and xx- components of normal stresses are shown in Figures 4.10 (b) and (c), respectively. The normal stress profiles are identical for all cases. Three mutually orthogonal components of the normal stresses are constant and equal in the bulk region. Hence, the pressure is calculated using averaged normal stress, and was found to be ~116kPa for each case, which is equal to the ideal gas predictions. Inside the force penetration depth, normal stress profiles are non-isotropic. This behavior emerges from the surface virial term due to the wall effects.

Velocity profile for k=1 flow (H=54nm) in half of the channel and the linearized Boltzmann solution at k=1 using α=1.0 and 0.75 are plotted in Figure 4.11 (a). Despite thermal fluctuations due to the use of very small bins, MD results agree better with the theory using α= 0.75 in the bulk region, while deviations from the kinetic theory solution are still observed inside the force penetration depth. Since these deviations are confined in the 3σ region, their influence extends only 4% of the domain for 54nm height channel. Figure 4.11 (b) shows velocity profiles for various k flows within 2nm distance from the top wall. Different profiles inside the force penetration depth shows effects of the Knudsen number on the near wall velocity profiles. Velocities in the near wall region increase with decreased k values due to the rarefaction effects.

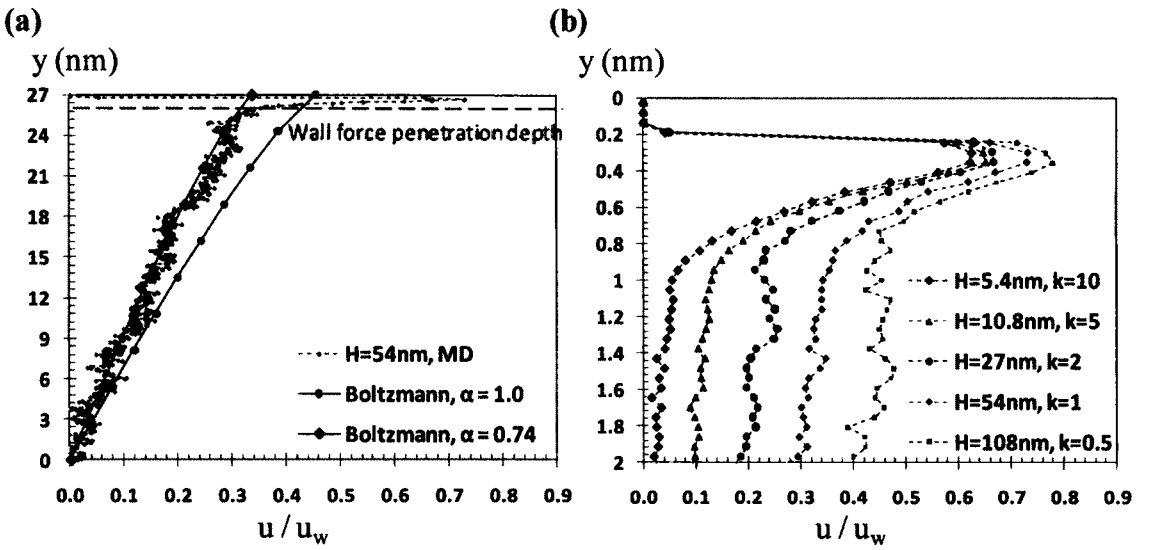

Figure 4.11 (a) Velocity profile for k=1 flow in half of the 54 nm height channel with linearized Boltzmann solutions using α=1.0 and 0.75. The domain is divided into 1000 bins. (b) Velocity profiles for various k flows within 2nm distance from the top wall. The wall velocity is 64m/s.

Constant wall velocity used in all cases (64m/s) creates different shear rates depending on the channel height and k value. Figure 4.12 (a) shows shear stress distributions in various k flows. Shear stress is constant up to one sigma distance from the wall. After which, surface virial component induces variations near the walls with single peak points linearly proportional to the bulk shear stress values. Constant shear cannot be achieved by simply adjusting the wall velocities, since the resulting shear response for different Knudsen flows is different. In order to make a comparison of shear stress variations inside the force penetration depth, I normalized the shear stress values with their corresponding bulk values of -13.17, -12.91, -11.21, -9.42 and -7.73kPa for the 5.4, 10.8, 27, 54 and 108nm height channels, respectively. Figure 4.12 (b) shows identical normalized shear stress distributions in the force penetration region for all five cases. Hence, the normalized shear stress variation in the near wall region is independent of the channel dimensions, shear rate and the Knudsen number.

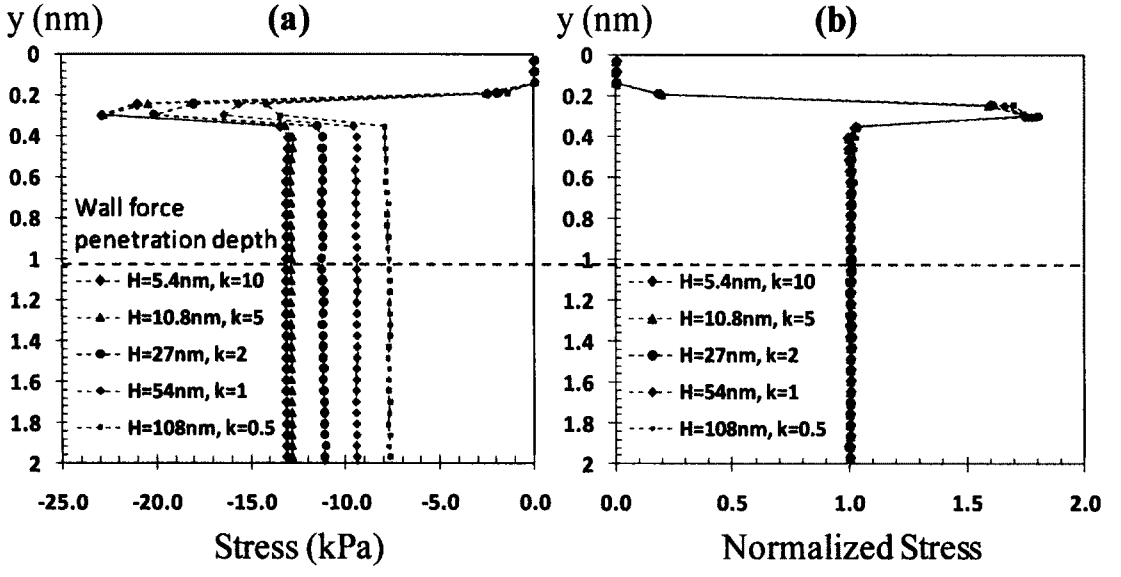

Figure 4.12 (a) Shear stress distribution for k=10, 5, 2, 1 and 0.5 flows confined in 5.4, 10.8, 27, 54 and 108nm height channels at constant wall velocity of 64m/s (M=0.2). (b) Shear stress variation within 2nm from the wall, normalized with -13.17, -12.91, -11.21, -9.42 and -7.73kPa for the 5.4, 10.8, 27, 54 and 108nm height channels, respectively.

Theoretical shear stress values are calculated using Equation (16) with finite Knudsen number correction in Equation (17) for various k values. Similar with the earlier cases, I predicted the TMAC values for Argon gas flow at k=0.5, 1, 2, 5 and 10 to be α=0.75.

4.3 Summary

The SWMD results of shear driven argon gas flows in nano-channels revealed significant wall force field effects on the velocity, density, shear stress and normal stress distributions in the near wall region that extends about 3σ from each surface. Within this region a density build up with a single peak point is observed. Normal components of the stress tensor are anisotropic, and dominated by the surface virial. Results show that the density and normal stress variations are scalable by the bulk density and pressure, and their behavior are unaffected by the shear driven flow, channel dimensions and gas rarefaction. The velocity profiles show sudden increase in gas velocity within this region.

This behavior is independent of the channel dimensions and density, however varies as a function of the Knudsen number due the rarefaction effects. Outside the "near wall" region, pressure is defined by the ideal gas law and the velocity distribution is predicted by kinetic theory based on the Boltzmann equation. Shear stress values are constant in the bulk region, while the surface virial induces variations very near the walls with a single peak point scalable with the bulk value. Simulation results verify linear stress strain-rate relationship at constant Knudsen values. Another important aspect of my findings is that one can predict the TMAC using 3D SWMD simulations. As a result, atomically smooth FCC crystal walls with (1,0,0) plane facing the gas resulted in TMAC=0.75, independent of the Knudsen number in the transition and free molecular flow regimes.

Overall the results show that the wall force field penetration depth is an additional length scale for gas flows in nano-channels, breaking the dynamic similarity between rarefied and nano-scale gas flows solely based on the Knudsen and Mach numbers. Hence, one should define a new dimensionless parameter as the ratio of the force field penetration depth to the characteristic channel dimension, where the wall effects cannot be neglected for large values of this dimensionless parameter.

CHAPTER 5

SURFACE-GAS INTERACTION EFFECTS ON NANOSCALE GAS FLOWS

With the advent of micro and nanotechnology, new sensors, resonators and scanning probes with sub-micron to nanometer size characteristic dimensions are being developed (Ekinci and Roukes 2005; Cleland et al. 2002; Husain et al. 2003; Verbridge et al. 2008). In such small scales, surface forces dominate over body forces, and surface-fluid interactions play a key role in momentum and energy transport. Nano-scale device components working in air under room conditions experience flow regimes that are substantially different from the classical continuum approximation. For example, the tip of an atomic force microscope (AFM) experiences harmonic variations in probe-surface separation distance from sub-micron down to the nanometer scale. During its oscillatory motion, the surrounding thin layer of gas induces a damping force on the tip, which is comparable with the AFM force output (Zhang et al. 2009). The first step in proper modeling of flows in such small scales is the recognition of the rarefaction and nonequilibrium effects described by the local Kn. For $Kn \geq 10$, the flow is in the free molecular regime, where gas-wall collisions are dominant and the collisionless Boltzmann equation can be used. For $0.1 \leq Kn \leq 10$, the flow is in the transition regime, where gas-gas and gas-wall collisions become equally important. Mathematical modeling of these flows requires utilization of Boltzmann equation, or direct simulation Monte Carlo (DSMC). High-order continuum approximations such as the Burnett and Grad equations can also be used (Karniadakis et al. 2005). For the AFM example, one can analyze the squeeze film damping problem using the kinetic theory, which models gas-wall interactions via various scattering kernels or the TMAC (α) (Guo and Alexeenko 2009; Bidkar et al. 2009; Gallis and Torczynski 2004). This classical approach mostly neglects the *surface force interactions between gas and wall molecules*. However, many molecular simulation and experimental studies in the literature reported significant effects of *surface-gas collisions* and *adsorbed gas molecules* on mechanical performance of

micro- and nano-scale devices (Honig et al. 2010; Feng and Jiang, 2011; Yang et al. 2011; Enguang 2002; Huang et al. 2008; Veijola et al. 1998; Gad-el-Hak 1999).

The tangential momentum accommodation coefficient was introduced by Maxwell as the fraction of gas molecules reflecting diffusively from a solid surface. TMAC value determines the tangential momentum exchange between gas and wall molecules, and it is heavily used in theoretical and numerical studies for rarefied, micro- and nano-scale gas flows. Several studies were conducted to determine its value using molecular beam and micro- and nano-channel gas flow experiments (Arkilic et al. 2001; Bentz et al. 1997, 2001; Goodman and Wachman 1976; Gronych et al. 2004; Rettner 1998; Sazhin et al. 2001), while the numerical research included MD simulations of single gas molecules interacting with crystalline surfaces (Arya et al. 2003; Chirita et al. 1993, 1997; Finger et al. 2007), two- and three-dimensional MD simulations (Cao et al. 2005; Sun and Li 2010, 2011), and coupled MD/DSMC models (Yamamato et al. 2006). Even though factors affecting the TMAC value are not well understood, these recent investigations demonstrated sensitivity of the accommodation coefficient to the surface-gas couple interaction parameters. In addition, gas adsorption on the surface is known to induce significant effects on transport (Zhou 2007; Lee and Aluru 2010; Finger et al. 2007, Sun and Li 2008).

The *objective* of this chapter is to investigate nano-scale shear-driven gas flows as a function of the wall-force field effects. In order to address this, two different sets of molecular dynamics simulations were performed at modified Knudsen number (k) values of k=1 and k=10, and for surface-gas pair interaction strength ratios of $1 \leq \varepsilon_{wf}/\varepsilon_{ff} \leq 6$. The range of simulation parameters covers the early transition and free molecular flow regimes, which are typical of nano-scale gas flows under standard conditions, and subjected to weak to strong gas-surface interactions. This chapter is organized as follows: In Section 1, I describe MD simulation parameters, explain the stress tensor computations and methods utilized in the MD algorithm. In Section 2, I present gas flow results at k=1 and k=10. Comparisons are made on density, velocity and shear stress profiles for each case. MD predictions of shear stress and velocity profiles are compared with the kinetic theory calculations, and TMAC values are predicted. Finally, Section 3 presents the conclusions.

5.1 Three-Dimensional MD Simulation Details

Shear driven argon gas flowsat k=1 and k=10 are simulated between two parallel plates separated with a distance h. Thermodynamic state of argon was fixed at 298K and 113.4kPa, corresponding to 1.896kg/m^3 density and 54nm mean free path (λ). Channel heights of h=54nm and h=5.4nm are used to establish k=1 and k=10 flows, respectively. Periodic boundary conditions are applied in the stream wise and lateral directions. Since gas flows evolve through intermolecular collisions, simulation domains span one mean free path in the periodic directions. Using such large domains in MD can be computationally overwhelming due to the excessively large number of wall molecules. I addressed this computational difficulty by using the recently developed SWMD algorithm, which reduces the memory requirements for modeling surfaces. For the three-dimensional FCC crystal structured wall with 0.54nm cube side length and (100) plane facing the gas molecules (used here), the SWMD limits memory use of a semi infinite wall slab into a stencil of 74 wall molecules (Barisik et al. 2010). The current SWMD is a fixed lattice model, where the wall molecules are rigid and keep their corresponding FCC positions (i.e., cold wall model). When a gas molecule approaches the surface and enters the near wall region, the SWMD wall stencil appears to model the wall. Figure 5.1 schematically shows this procedure, where patchy walls on the right figure shows SWMD stencils during a simulation. Although there are many wall stencils at a given instant, all of these are modeled using the same 74 wall molecules shown in the middle figure, resulting in significant computational advantages (Barisik et al. 2010).

Figure 5.1 Illustration of the SWMD procedure.

Shear driven flow is obtained by moving the top and bottom channel walls in opposite directions with a characteristic velocity of $U_w = M\sqrt{\gamma k_b T/m}$, where M is the

Mach number, γ is the adiabatic index (5/3 for monatomic molecules), k_b is the Boltzmann constant (1.3806×10^{-23}J K^{-1}), T (298K) is the temperature, and m is the mass of gas molecules. Mass for an argon molecule is $m = 6.63\times10^{-26}$kg, its molecular diameter is σ = 0.3405nm and the depth of the potential well for argon is $\varepsilon = 119.8\times k_b$. For simplicity, the walls have molecular mass and diameter equivalent to argon ($m_{wall} = m_{Ar}$, $\sigma_{wall} = \sigma_{Ar}$).

Lenard-Jones (L-J) 6-12 potential is utilized to model the van der Waals interactions between gas-gas and gas-wall molecules. The ratio of the potential strength for gas-wall interactions (ε_{wf}) to the gas-gas molecular interactions (ε_{ff}) is assigned to have values of $\varepsilon_{wf}/\varepsilon_{ff}$=1,2,3,4,5 and 6. Since the L-J potential vanishes at larger molecular distances, only the interactions with particles within a certain cut-off radius (r_c) are calculated. Therefore, the intermolecular interaction forces are truncated and switched to zero at a certain cut-off distance (Allen and Tildesley 1989). In this study I utilize r_c=1.08 nm, which is approximately equal to 3.17σ for argon molecules. At this cut-off-distance the attractive part of the LJ potential is reduced to 0.00392ε. My algorithm utilizes the well-known link cell method to handle particle-particle interactions (Allen and Tildesley 1989).

Simulations start from the Maxwell-Boltzmann velocity distribution for gas molecules at 298K. Initial particle distribution is evolved 10^6 time-steps (4ns) to reach an isothermal steady state using $4fs$ (~0.002τ) time steps, after which, 2×10^6 time steps (8 ns) are performed for time averaging. Longer time averaging has also been performed to confirm the convergence of density, stress and velocity profiles to steady state. In order to capture the property variations within the near wall region accurately and with same resolution, all simulation domains are divided into equally sized slab bins of 0.054nm in the wall normal direction. As a result, k=1 cases use 1,000 slab bins, while k=10 case utilizes 100 slab bins. Canonical ensemble (NVT, i.e., constant mole, N, volume, V, and temperature, T) is performed by utilizing a thermostat. I employed the Nose-Hoover algorithm (Evans and Hoover 1986) as a global thermostat inside the local sub-domains to obtain isothermal condition of 298K with a relaxation time of ~ $0.2ps$. Sub-domains have 0.54nm heights through the entire span which is 10 times larger than the utilized bin size.

5.2 Results

In this section, results of Argon gas confined in nano-channels are presented in two different sets. Initially, shear driven gas flows in the early transition regime (k=1) are simulated in 54nm height channels. This is followed with gas flows confined in 5.4nm height channels (k=10), corresponding to the free molecular flow regime. In both cases, I studied surface effects at different $\varepsilon_{wf}/\varepsilon_{ff}$ ratios that vary between 1 and 6.

5.2.1 Gas flows at k=1

I start my investigations with argon gas confined in 54nm height channel with different $\varepsilon_{wf}/\varepsilon_{ff}$ values. Snapshots of the simulation domains are shown in Figure 5.2, where the gas molecules are shown in green. Presence of a gas molecule within the wall force penetration region requires utilization of the smart wall stencil on the surface, which are shown in blue and black on the bottom and top surfaces of the channel, respectively. Increase in the surface-gas interaction strength results in more gas molecules in the vicinity of the surface. The $\varepsilon_{wf}/\varepsilon_{ff}$ =6 case approaches to complete surface coverage, as can be seen in Figure 5.2 (g). Since different $\varepsilon_{wf}/\varepsilon_{ff}$ values result in different number of adsorbed molecules on the surfaces, I start each simulation using the proper number of molecules to obtain the desired gas density in the bulk of the channels. Simulation details, such as the number of molecules used in computation of different $\varepsilon_{wf}/\varepsilon_{ff}$ ratio flows and the corresponding bulk density of argon are shown in Table 5.1.

Table 5.1 Simulation details of k=1 flows confined in 54nm height channels at 298K & 113.4kPa. Theoretical free molecular shear stresses (τ_∞), corrected stress values for k=1 flow ($\tau_{k=1}$), MD results (τ_{MD}) and TMAC predictions are tabulated for various $\varepsilon_{wf}/\varepsilon_{ff}$ values.

$\varepsilon_{wf}/\varepsilon_{ff}$	# molecules	ρ_{bulk} (kg/m^3)	k	τ_∞ (kPa)	$\tau_{k=1}$(kPa)	τ_{MD} (kPa)	TMAC
1	4,500	1.89	1.01	-23.97	-15.70	-9.51	0.75
2	4,700	1.87	1.02	-23.78	-15.62	-12.85	0.90
3	5,500	1.84	1.03	-23.42	-15.45	-13.77	0.94
4	10,000	1.90	1.00	-24.15	-15.66	-14.61	0.96
5	22,000	1.88	1.01	-23.89	-15.50	-15.02	0.98
6	36,000	1.85	1.03	-23.51	-15.25	-15.03	0.99

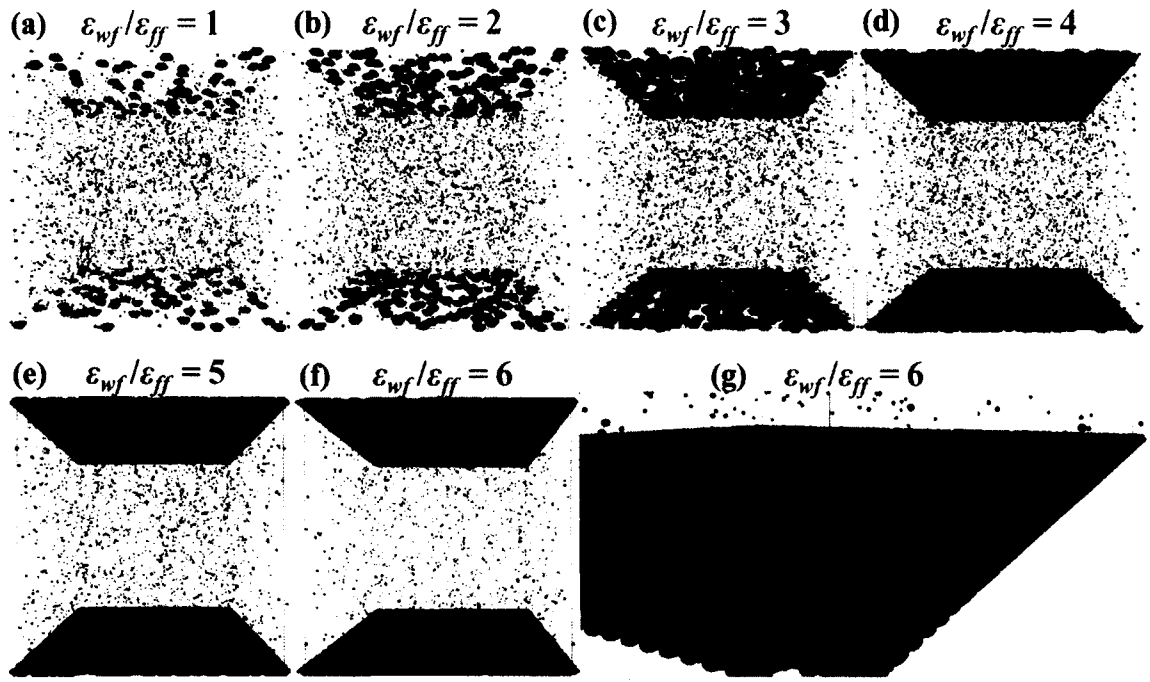

Figure 5.2 (a-f) Snapshots of argon gas flows at k=1 with various $\varepsilon_{wf}/\varepsilon_{ff}$ values. All simulations are confined in 54×54×54nm domains at 298K & 113.4kPa. Figure (g) shows adsorbed argon gas layer on the bottom surface for the $\varepsilon_{wf}/\varepsilon_{ff}$=6 case.

Density distributions within 2 nm from the top wall are shown in Figure 5.3 (a) for each $\varepsilon_{wf}/\varepsilon_{ff}$ case. The wall is defined at the center of the first row of wall molecules facing the fluid. Therefore, gas molecules cannot penetrate to several bins neighboring the wall, and the gas density goes to zero within 0.2nm from the walls. With the exception of the near wall regions, argon density is approximately 1.89kg/m^3. Surface forces induce increased particle residence time inside the force penetration depth, which results in density buildup. For $\varepsilon_{wf}/\varepsilon_{ff} \leq 5$, there is a single density peak point near the surface. But at $\varepsilon_{wf}/\varepsilon_{ff}$ =6, I observe a second density peak which is much weaker than the first value (less than 0.3% of the first peak value). It should be noted that this behavior is different than the dense gas case, where the second density peak value was comparable with the first one (48% of first peak value), which indicated the onset of density layering (Barisik and Beskok 2011a). For the case of $\varepsilon_{wf}/\varepsilon_{ff}$= 1 density starts to deviate from its bulk value around 2.5σ from the wall, while the density profiles for $\varepsilon_{wf}/\varepsilon_{ff}$= 6 case penetrate approximately 3σ from the wall. This shows that increased $\varepsilon_{wf}/\varepsilon_{ff}$ values

enhance the surface influence zone. For all cases, the near wall gas density increases with increasing the $\varepsilon_{wf}/\varepsilon_{ff}$, which is due to the adsorption of a single layer of argon gas molecules on the surface as can be seen on Figure 5.2 (e)-(g). In order to categorize the adsorption behavior, I calculated the number of the gas molecules near the surface. Assuming a monolayer of adsorbate on surface, I consider the gas molecules σ away from the surface. For the current case, wall molecules penetrate 0.5σ into the simulation domain (since y=0 is located at the center of wall molecules), therefore I calculate the sum of the gas molecules 1.5σ away from the surface. Figure 5.3 (b) shows the number of molecules per unit surface area, which increases with increased $\varepsilon_{wf}/\varepsilon_{ff}$, and approaches to the maximum limit of single layer adsorption. For the $\varepsilon_{wf}/\varepsilon_{ff}$ =6 case, surface molecular coverage reaches 6.08#/nm^2, while the hypothetical value for complete surface coverage due to the adsorption sites on a (1 0 0) surface is 6.86#/nm^2.

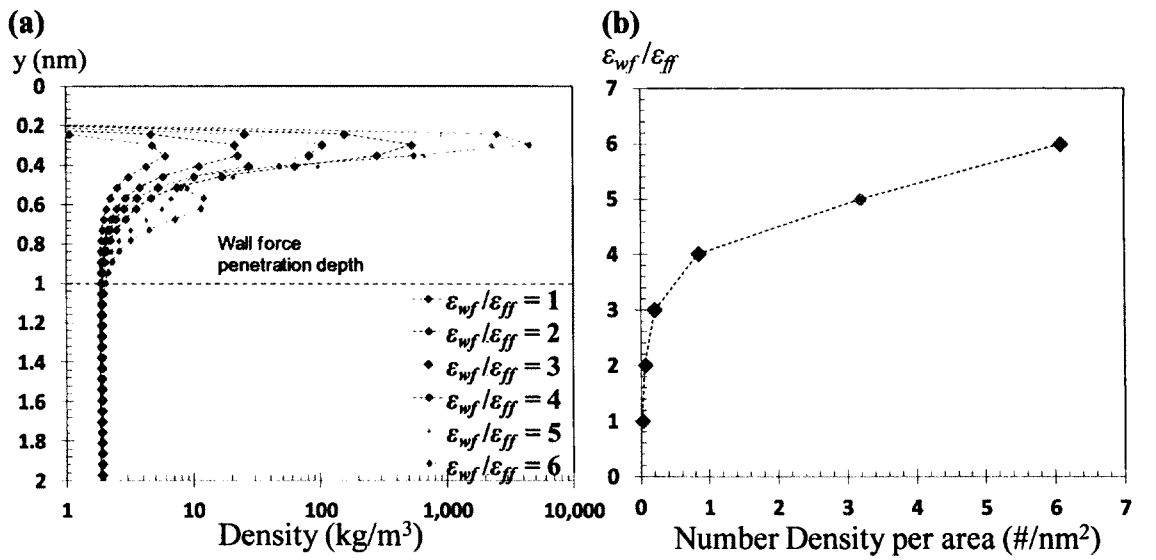

Figure 5.3 (a) Argon density variation in k=1 flows within 2 nm from the wall for various $\varepsilon_{wf}/\varepsilon_{ff}$ values. (b) Number density of argon molecules per surface area as a function of $\varepsilon_{wf}/\varepsilon_{ff}$ ratio.

Velocity profiles in half of the channel and the linearized Boltzmann (LB) solution for k=1 flow subjected to the TMAC (α) values of α=1 and α=0.75are shown in Figure 5.4 (a). The MD velocity profiles agree with the kinetic theory predictions adopted

from (Sone et al. 1990) in the bulk region. I observe a better match between the MD results for $\varepsilon_{wf}/\varepsilon_{ff}=1$ case and the LB solution using $\alpha=0.75$. Increase in $\varepsilon_{wf}/\varepsilon_{ff}$ increases the bulk velocity, which reaches to the LB solution of $\alpha=1$ for $\varepsilon_{wf}/\varepsilon_{ff}\geq 3$ cases. MD velocity profiles show sudden changes within the force penetration depth.Since these deviations are confined in the 3σ region, their influence extends only 4% of the domain for 54nm height channel. Figure 5.4 (b) shows zoomed view of this region to explore the velocity variation inside the wall force penetration depth. For $\varepsilon_{wf}/\varepsilon_{ff}\geq 3$, gas velocity reaches the wall velocity due to adsorption of gas molecules on to the surface. Despite the large amount of slip velocity predicted by the kinetic theory solution, the near wall velocity profiles for $\varepsilon_{wf}/\varepsilon_{ff}\geq 3$ cases show velocity stick in k=1 flows. This behavior is due to the wall force field that diminishes approximately 3σ away from the wall surface, after which the kinetic theory solution is valid.

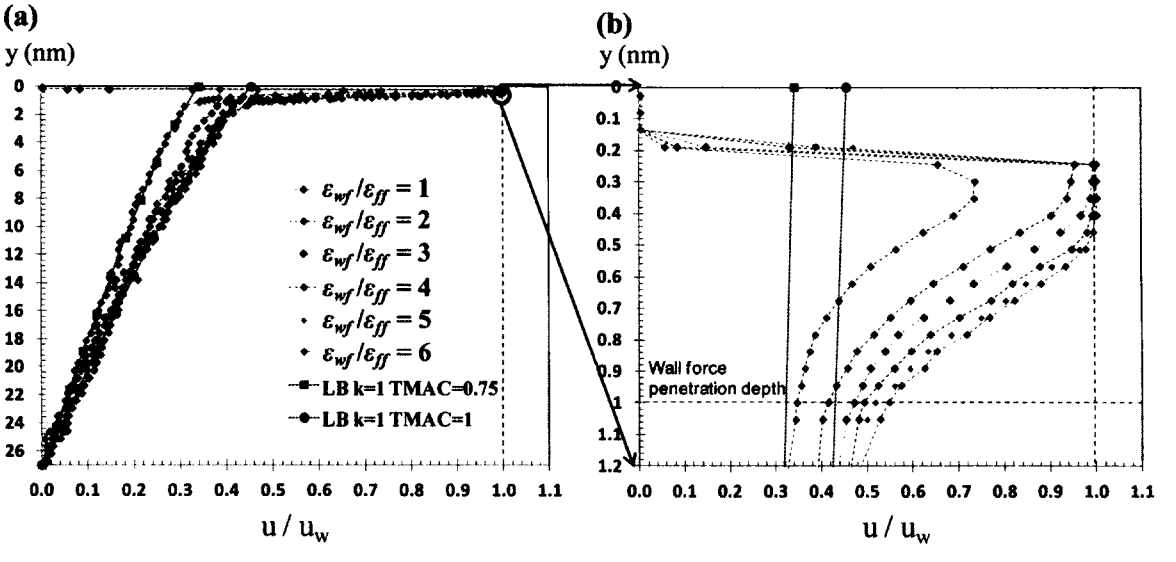

Figure 5.4 Velocity profiles for k=1 flows with different $\varepsilon_{wf}/\varepsilon_{ff}$ values in (a) the half of the 54nm height channel and (b) within 1.2 nm distance from the walls. Velocity profiles are normalized with the constant wall velocity of 64m/s.

Based on the kinetic theory of gases, shear stress for a shear driven flow in the free molecular flow regime ($Kn \rightarrow \infty$) can be calculated by Equation (16) (Shen 2005).

Specular reflections (α =0) will not drive the fluid, and result in zero shear stress. Therefore the shear stress for free molecular flows varies between a maximum value for α=1 to zero for α=0 based on Equation (16). In order to consider the finite Knudsen number effects, I utilized the Equation (17) which is uniformly valid from the free molecular to slip flow regimes (Bahukudumbi et al. 2003). Theoretical free molecular shear stresses (τ_∞) and corrected stress values for k=1 flow ($\tau_{k=1}$) are calculated for each simulation case by considering the gas bulk density. Results are tabulated in Table 5.1.

Figure 5.5 shows MD shear stress distribution in nano-channels within 1.2 nm distance from the top wall for each $\varepsilon_{wf}/\varepsilon_{ff}$ case. Despite the constant wall velocity of 64 m/s (M=0.2) applied for each case, increase of $\varepsilon_{wf}/\varepsilon_{ff}$ increases the shear rates and shear stresses inside the channels. All $\varepsilon_{wf}/\varepsilon_{ff}$ cases are eventually at the same bulk density and k with slight fluctuations (Table 5.1). In order to make a fair comparison, I normalized the shear stress profiles using theoretical values corresponding to k=1and α=1 (shown by $\tau_{k=1}$) in Table 5.1. Dimensional values of MD shear stress results in the bulk region (τ_{MD}) are also tabulated. As can be seen in Figure 5.5, shear stress is constant in the bulk region while the surface forces induce variations near the walls. This is due to the virial contribution of shear stress which is mostly negligible through the gas domains. In presence of a surface, the surface-gas virial and later the gas-gas virial of adsorbed molecules become dominant inside the force penetration depth. For $\varepsilon_{wf}/\varepsilon_{ff} \leq 3$, shear stress starts to deviate from its bulk value with a single peak point approximately σ distance from the wall. This peak induced by the surface virial decays closer to the surface due to the diminishing density at y≈0.2nm. Interestingly, density and density related properties are in decreasing trend while the surface virial peaks. This region, from one sigma distance to zero density, is the main location where wall and gas molecules interact with strong repulsive forces. An increase in the ε_{wf} value results in stronger surface-gas interactions; and hence, the surface virial becomes more dominant and increases the peak value. However, further increase of $\varepsilon_{wf}/\varepsilon_{ff}$ results in adsorption of gas molecules, and increases the importance of gas-gas virial terms. Starting with the $\varepsilon_{wf}/\varepsilon_{ff}$ =4 case, attractive interactions between the gas molecules near surface create a dip in the shear stress at the location of the first density peak. This is followed by a second shear

stress peak point due to the repulsion between the molecules of first and second density peaks approximately 0.5nm from the surface.

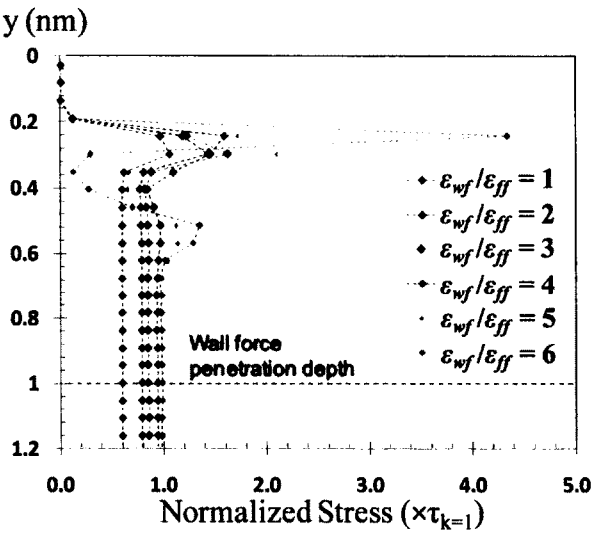

Figure 5.5 Normalized shear stress distribution for various $\varepsilon_{wf}/\varepsilon_{ff}$ gas flows at k=1. Normalization is obtained using the corresponding theoretical shear stress values for k=1 and α=1 ($\tau_{k=1}$ in Table 5.1).

Comparing MD shear stress results with the theoretical values calculated using Equations (16) and (17), I predicted the TMAC values for argon gas interacting with different $\varepsilon_{wf}/\varepsilon_{ff}$ surfaces. Results in Table 5.1 show TMAC values varying from α =0.75 to α =0.90 for $1 \leq \varepsilon_{wf}/\varepsilon_{ff} \leq 6$. Since I predict the TMAC values directly using the bulk flow shear stress, it is important to verify the consistency of my TMAC predictions by comparing the velocity profiles obtained from MD simulations with the kinetic theory predictions for k=1 flows at different TMAC values. Figure 5.6 shows the velocity profiles for $\varepsilon_{wf}/\varepsilon_{ff}$=1 and $\varepsilon_{wf}/\varepsilon_{ff}$=2 cases, which are in good agreement with the linearized Boltzmann solution using TMAC values of α=0.75 and α=0.90, respectively.

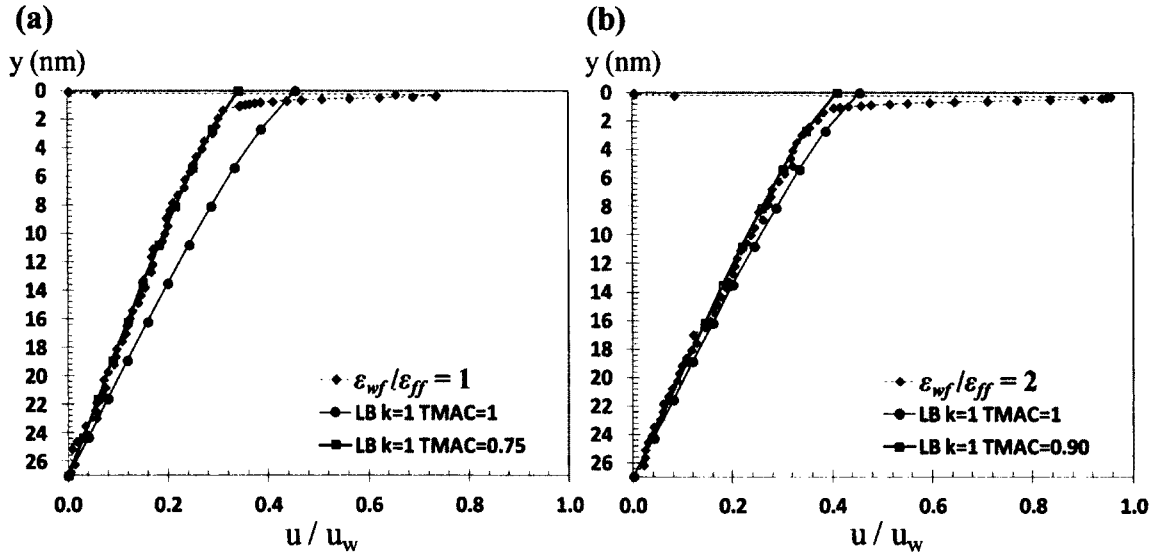

Figure 5.6 Comparison of the velocity profiles for k=1 flows in half of the 54nm height channel with linearized Boltzmann solutions using (a) α=0.75 for $\varepsilon_{wf}/\varepsilon_{ff}$=1 and (b) α=0.9 for $\varepsilon_{wf}/\varepsilon_{ff}$=2.

5.2.2 Gas Flows at k=10

Shear driven gas flows at k=10 inside 5.4 nm height channels are studied for various $\varepsilon_{wf}/\varepsilon_{ff}$ values. Simulation details are given in Table 5.2. Similar to the earlier case, adsorption of gas molecules on solid surfaces increases with increased $\varepsilon_{wf}/\varepsilon_{ff}$ values. Figure 5.7 (a) shows density variations in half of the channel for different $\varepsilon_{wf}/\varepsilon_{ff}$ cases. Bulk density is constant while the surface forces result in density accumulation appearing as a single density peak inside the wall force penetration depth. The figure also presents the density profiles for k=10 cases for comparison purposes. Identical density profiles are observed between different k flows at same $\varepsilon_{wf}/\varepsilon_{ff}$ values. In my earlier study, a universal behavior inside the wall force penetration depth of various $\varepsilon_{wf}/\varepsilon_{ff}$=1 gas flows was presented for the different values of the characteristic dimensions of confinement, gas density and k values (Barisik and Beskok 2011b). Results in Figure 5.7 (a), further validate my previous findings by providing a universal density distribution for various $\varepsilon_{wf}/\varepsilon_{ff}$ values regardless of the Knudsen number.

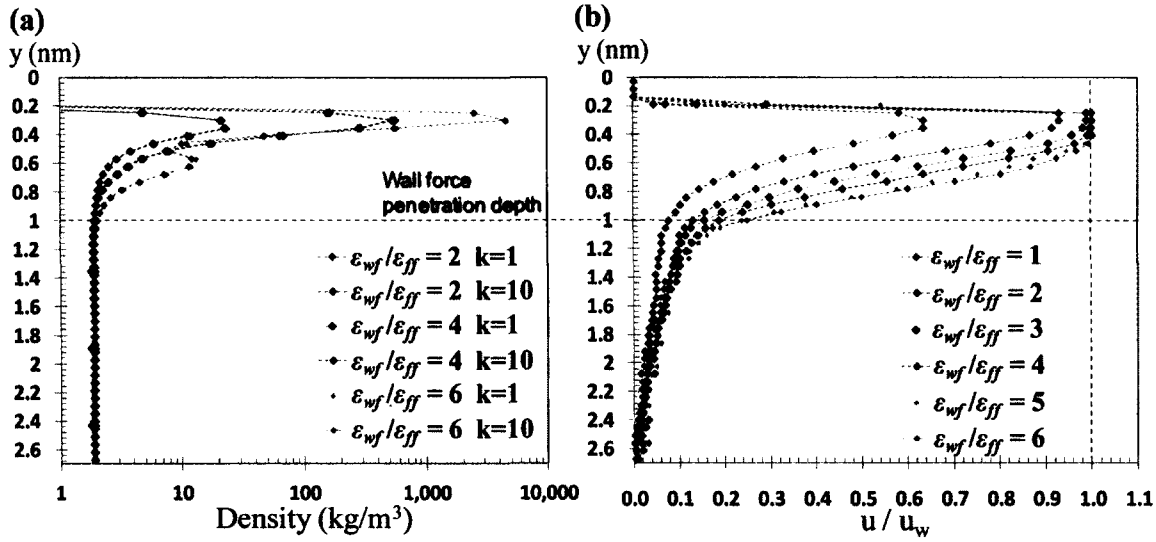

Figure 5.7 (a) Comparison of density profiles for k=1 and k=10 flows for $\varepsilon_{wf}/\varepsilon_{ff}$=2, 4 and 6 within 2.7 nm distance from wall. (b) Velocity profiles of k=10 flows with different $\varepsilon_{wf}/\varepsilon_{ff}$ values in the half of the 5.4nm height channel. Wall velocity is equal to 64m/s.

Table 5.2 Simulation details of k=10 flows within 5.4nm height channels at 298K & 113.4kPa. Theoretical free molecular shear stresses (τ_∞), corrected stress values for k=1 and α=1 flow ($\tau_{k=1}$), MD results (τ_{MD}) and TMAC predictions are tabulated for various $\varepsilon_{wf}/\varepsilon_{ff}$ values.

$\varepsilon_{wf}/\varepsilon_{ff}$	# molecules	ρ_{bulk} (kg/m³)	k	τ_∞ (kPa)	$\tau_{k=10}$(kPa)	τ_{MD}(kPa)	TMAC
1	450	1.82	10.5	-23.12	-21.75	-13.07	0.75
2	690	1.88	10.1	-23.88	-22.42	-17.65	0.90
3	1,570	1.84	10.3	-23.39	-21.98	-18.83	0.93
4	5,300	1.77	10.7	-22.56	-21.24	-19.80	0.96
5	19,000	1.77	10.7	-22.39	-21.09	-20.26	0.98
6	32,000	1.99	9.6	-25.29	-23.65	-23.08	0.99

In Figure 5.7 (b), velocity profiles normalized with the wall velocity are plotted in half of the channel. In the bulk region, MD results agree with the linearized Boltzmann solutions with corresponding α values. Large velocity variations are observed within the force penetration depth, which covers 40% percent of the simulation domain. Similar with the k=1 cases, gas velocity reaches to the wall velocity for $\varepsilon_{wf}/\varepsilon_{ff} \geq 3$. At this point, one can specify location of the wall and the corresponding velocity boundary condition predicted by the current atomistic model. Due to the finite size of molecules and wall

corrugation effects, gas molecules cannot penetrate closer than y ≈ 0.2nm. Depending on $\varepsilon_{wf}/\varepsilon_{ff}$, the maxima in gas density is at 0.3 ≤ y ≤ 0.34nm, while the shear stresses and gas velocities peak at 0.24 ≤ y ≤ 0.3nm. Observation of the velocity profiles clearly show location of the wall (from continuum point of view) around y=0.24nm. By using this information, I can conclude that $\varepsilon_{wf}/\varepsilon_{ff} \geq 3$ results in velocity stick boundary condition, while velocity slip is observed for lower $\varepsilon_{wf}/\varepsilon_{ff}$ values. This is a drastic difference from the LB solution, which indicates substantial velocity slip on the walls.

Shear stress variation in 5.4nm height channel shows similar behavior with the earlier case of the k=1, except that the bulk flow stress values are higher due to higher k (Table 5.2). Shear stress is constant in the bulk flow region, while the surface-gas interactions and for $\varepsilon_{wf}/\varepsilon_{ff} \geq 2$ the gas-gas interactions induce deviations in the wall force penetration depth. Using the same approach for k=1 flow, I calculated the TMAC values of k=10 flows for various $\varepsilon_{wf}/\varepsilon_{ff}$ cases, and tabulated them in Table 5.2. Starting with the value of 0.75 for $\varepsilon_{wf}/\varepsilon_{ff}=1$, TMAC increases with increased ε_{wf}, and approaches unity for $\varepsilon_{wf}/\varepsilon_{ff} \geq 3$. TMAC variations for k=1 and k=10 flows for the studied cases are plotted in Figure 5.8. TMAC variations as a function of $\varepsilon_{wf}/\varepsilon_{ff}$ are shown to be independent of the Knudsen number, which was also a conclusion I derived in an earlier study obtained for $\varepsilon_{wf}/\varepsilon_{ff}= 1$ flow at different k values (Barisik and Beskok 2011b).

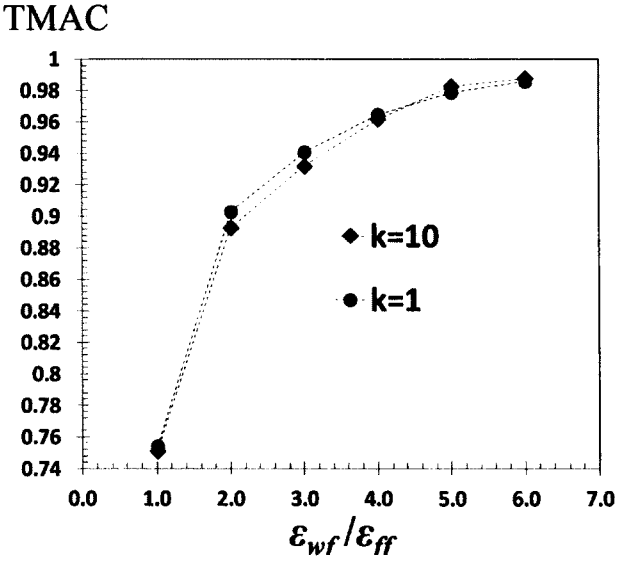

Figure 5.8 TMAC variation of k=1 and k=10 flows as a function of the normalized gas-wall potential strength ratio $\varepsilon_{wf}/\varepsilon_{ff}$.

5.3 Summary

The findings show that surface gas interaction strength uniquely define the tangential momentum exchange between gas and wall molecules (i.e. TMAC) regardless of the local Kn value and channel dimensions. As a result, the bulk flow velocity profile, and shear stress are functions of the $\varepsilon_{wf}/\varepsilon_{ff}$ ratio and the Knudsen number. Kinetic theory based velocity profiles using calculated TMAC values agree well with MD velocity profiles in the bulk flow region. Despite this agreement, MD results show formation of a near-wall region within three molecular diameters away from the surface. In this region, gas density and velocity increase with increased $\varepsilon_{wf}/\varepsilon_{ff}$ ratio. Although $\varepsilon_{wf}/\varepsilon_{ff} \geq 3$ cases result in velocity stick on the surface, induced by the density buildup and onset of adsorption, neglection of this near wall region results in slip of the bulk flow region, consistent with the kinetic theory predictions. The presence of this near wall region shows breakdown of the dynamic similarity between rarefied and nano-scale gas flows based on the Knudsen and Mach numbers. Hence, one should define a new dimensionless parameter as the ratio of the force field penetration depth to the characteristic channel dimension, where wall effects cannot be neglected for large values of this parameter. A good example of this is the k=10 case obtained in 5.4nm height channel, where the deviations from kinetic theory predictions extends over 40% of the channel.

CHAPTER 6

CONCLUSIONS

Molecular dynamics simulations of rarefied gas flows are overwhelmed by the number of wall molecules compared to the gas molecules. This has limited the use of MD in nano-scale gas transport problems. In this study, I introduced a smart wall molecular dynamics algorithm (SWMD), which models three-dimensional Face Centered Cubic (FCC) walls in the (1,0,0) plane using only 74 wall molecules. This is a simple, yet important development, which allowed us to simulate gas flows within arbitrarily large domains. Within the current implementation, the computations are dominated by the number of gas molecules and their interactions with walls are modeled using the 74 molecule wall stencil, resulting in significant memory savings in computations. Using the SWMD, I was able to perform three-dimensional MD simulations spanning one mean free path length in all three directions. To my knowledge, MD simulations of rarefied gas flows in such large flow domains have not been attempted before.

Thermodynamic properties of Argon at dilute gas, dense gas and liquid density conditions were studied. Using the Irving-Kirkwood method, I calculated the normal stresses (pressure) for argon gas and liquid within periodic domains, and verified the results using published thermodynamic states. I presented the importance of long-range force field interactions and concluded that MD can predict the thermodynamic pressure providing that sufficiently large force cut-off distances are utilized in the computations. Next, behavior of dilute gas, dense gas and liquid states was studied within nanoscale confinements. Presence of surface creates anisotropic normal stresses primarily caused by surface virial which was introduced as a measure of surface effects. Existence of "Surface Virial" was validated by providing its clear appearance on the development of the well known liquid density layering.

Subsequent work focused on shear driven gas flows in nanoconfinements. Significant effects of wall force field on the velocity, density, shear stress and normal stress distributions inside force penetration depths was presented. Sudden increases of density, velocity, normal stress and shear stress were observed within this region. This

behavior is found to be independent of the channel dimensions and density, however it varies as a function of the Knudsen number due the rarefaction effects. Away from this region, kinetic theory predictions agree well with MD. Another interesting finding of this study is the calculation of Tangential Momentum Accommodation Coefficient (TMAC) by simply comparing the MD calculated shear stress with the theory. TMAC values for different simulations of specified gas/surface couple was calculated as TMAC=0.75, independent of the Knudsen number in the transition and free molecular flow regimes.

Shear driven argon gas flows were studied in the early transition and free molecular flow regimes for different surface-gas potential strength ratios ($\varepsilon_{wf}/\varepsilon_{ff}$). Similar to the results discussed in the earlier chapters, a bulk flow region and a near wall region that extends three molecular diameters away from the surfaces were observed. Within the near wall region the velocity, density, and shear stress distributions exhibit deviations from the kinetic theory predictions. Gas density increased by increased $\varepsilon_{wf}/\varepsilon_{ff}$ and got close to monolayer adsorption on surfaces. Velocity slip values were found to be smaller than kinetic theory solutions and eventually velocity stick was observed with increased $\varepsilon_{wf}/\varepsilon_{ff}$. Using the same approach introduced earlier, TMAC values were calculated as a function of $\varepsilon_{wf}/\varepsilon_{ff}$, and similar TMAC values were found for the cases at the same $\varepsilon_{wf}/\varepsilon_{ff}$, independent of the Knudsen number.

Overall the results show that the wall force field penetration depth is an additional length scale for gas flows in nano-channels, breaking the dynamic similarity between rarefied and nano-scale gas flows solely based on the Knudsen and Mach numbers. Hence, one should define a new dimensionless parameter as the ratio of the force field penetration depth to the characteristic channel dimension, where the wall effects cannot be neglected for large values of this dimensionless parameter.

REFERENCES

Allen MP, Tildesley DJ (1989) Computer simulation of liquids. Oxford Science Publications Oxford University Press, New York

Arkilic EB, Breuer KS, Schmidt MA (2001) Mass flow and tangential momentum accommodation in silicon micromachined channels. Journal of Fluid Mechanics 437:29-43

Arya G, Chang HC, Maginn EJ (2003) Molecular simulations of Knudsen wall-slip: effect of wall morphology. Molecular Simulation 29(10–11):697–709

Bahukudumbi P, and Beskok A (2003a) A phenomenological lubrication model for the entire Knudsen regime. Journal of Micromechanics and Microengineering, 13(6): 873-884

Bahukudumbi P, Park JH, Beskok A (2003b) A unified engineering model for steady and quasi-steady shear-driven gas microflows. Microscale Thermophysical Engineering, 7:291-315

Barisik M, Kim B, Beskok A (2010) Smart wall model for molecular dynamics simulations of nanoscale gas flows. Communications in Computational Physics doi:10.4208/cicp.2009.09.118

Barisik M, Beskok A (2011a) Equilibrium molecular dynamics studies on nanoscale confined fluids. Microfludics Nanofludics. doi:10.1007/s10404-011-0794-5

Barisik M, Beskok A (2011b) Molecular dynamics simulations of shear-driven gas flows in nano-channels. Microfludics Nanofludics. doi:10.1007/s10404-011-0827-0.

Bentz JA, Tompson RV, Loyalka SK (1997) The spinning rotor gauge: measurements of viscosity, velocity slip coefficients, and tangential momentum accommodation coefficients for N2 and CH4. Vacuum 48(10):817–24

Bentz JA, Tompson RV, Loyalka SK (2001) Measurements of viscosity, velocity slip coefficients, and tangential momentum accommodation coefficients using a modified spinning rotor gauge. J Vacuum Sci Technol A – Vacuum Surf Films 19(1):317–24

Beskok, A., and Karniadakis G.E. (1994) Simulation of Heat and Momentum Transfer in Complex Micro-Geometries. Journal of Thermophysics and Heat Transfer, 8(4):647-655

Bidkar RA, Tung RC, Alexeenko AA, Sumali H, Raman A (2009) Unified theory of gas damping of flexible microcantilevers at low ambient pressures. Applied Physics Letters doi:10.1063/1.3122933.

Bird GA (1994) Molecular Gas Dynamics and the Direct Simulation of Gas Flows. Oxford Science Publications, Midsomer Norton, Avon, UK

Cao BY, Chen M, Guo ZY (2005) Temperature Dependence of the Tangential Momentum Accommodation Coefficient for Gases. Applied Physics Letters doi:10.1063/1.1871363

Cercignani C, Lampis M (1971) Kinetic models for gas-surface interactions. Transport Theory and Stat. Phys 1:101–114

Cercignani C, Pagani CD (1966) Variational approach to boundary value problems in kinetic theory. Physics of Fluids 9:1167-1173

Cieplak M, Koplik J and Banavar JR (1999) Applications of statistical mechanics in subcontinuum fluid dynamics. Physica A-Statistical Mechanics and Its Applications, 274(1-2):281-293

Cieplak M, Koplik J and Banavar JR (2000) Molecular dynamics of flows in the Knudsen regime. Physica A-Statistical Mechanics and Its Applications, 287(1-2):153-160

Cieplak M, Koplik J and Banavar JR (2001) Boundary conditions at a fluid-solid interface. Physical Review Letters, 86(5):803-806

Cieplak M, Koplik J and Banavar JR (2006) Nanoscale fluid flows in the vicinity of patterned surfaces. Physical Review Letters, 96(11):114502

Chirita V, Pailthorpe BA, Collins RE (1993) Molecular dynamics study of low-energy Ar scattering by the Ni(001) surface J Phys D: Appl Phys 26(1):133–42

Chirita V, Pailthorpe BA, Collins RE (1997) Non-equilibrium energy and momentum accommodation coefficients of Ar atoms scattered from Ni(0 0 1) in the thermal regime: a molecular dynamics study. Nucl Instrum Methods Phys Res B – Beam Interact Mater Atoms 129(4):465–73

Clelanda AN, Aldridge JS, Driscoll DC, Gossard AC (2002) Nanomechanical displacement sensing using a quantum point contact. Applied Physics Letters 81:1699-1701.

Ekinci KL, Roukes ML (2008) Nanoelectromechanical systems. Rev. Sci. Instrum. doi:10.1063/1.1927327.

Enguang D (2002) Surface-related phase noise in SAW resonators. IEEE Trans Ultrason Ferroelectr Freq Control 49:649-55.

Evans DJ, Hoover WG (1986) Flows far from equilibrium via molecular-dynamics. Annual Review of Fluid Mechanics 18:243-264

Feng C, Jiang LY (2011) Molecular dynamics simulation of squeeze-film damping effect on nano resonators in the free molecular regime. Physica E 43:1605-1609.

Finger GW, Kapat JS, Bhattacharya A (2007) Molecular Dynamics Simulation of Adsorbent Layer Effect on Tangential Momentum Accommodation Coefficient. Journal of Fluids Engineering doi:10.1115/1.2375128

Frenkel D, Smit B (2002) Understanding molecular simulation: from algorithms to applications. Elsevier, San Diego

Fukui S, Kaneko R (1990) A database for interpolation of Poiseuille flow rates for high Knudsen number lubrication problems. Journal of Tribology 112:78-83

Fukui S, Kaneko R (1987) Analysis of Ultra-thin Gas Film Lubrication Based on the Linearized Boltzmann Equation: Influence of Accommodation Coefficient. JSME International Journal 30:1660–1666

Gad-el-Hak M (1999) The fluid mechanics of microdevices—The Freeman Scholar Lecture. J Fluids Eng-Trans ASME, 121:5-33.

Gallis MA, Torczynski JR (2004) An improved Reynolds-equation model for gas damping of microbeam motion. Journal of Microelectromechanical Systems 13(4):653–9.

Goodman FO, Wachman HY (1976) Dynamics of gas-surface scattering. Academic Press. New York

Gronych T, Ulman R, Peksa L, Repa P (2004) Measurements of the relative momentum accommodation coefficient for different gases with a viscosity vacuum gauge. Vacuum 73(2):275–9

Guo M, Lu BCY (1997) Long range corrections to thermodynamic properties of inhomogeneous systems with planar interfaces. The Journal of Chemical Physics 106(9):3688-3695

Honig CDF, Sader JE, Mulvaney P, Ducker WA (2010) Lubrication forces in air and accommodation coefficient measured by a thermal damping method using an atomic force microscope. Physical Review E doi:10.1103/PhysRevE.81.056305.

Huang B, Li Z, Liu Z, Zhou G, Hao S, Wu J, Gu BL, Duan W (2008) Adsorption of gas molecules on graphene nanoribbons and its implication for nanoscale molecule sensor. J Phys. Chem. C 112:13442-13446.

Husain A, Hone J, Postma HWC, Huang XMH, Drake T, Barbic M, Scherer A, Roukesa ML (2003) Nanowire-based very-high-frequency electromechanical resonator. Applied Physics Letters 83:1240-1242.

Irving JH, Kirkwood JG (1950) The statistical mechanical theory of transport processes. IV. The equations of hydrodynamics. The Journal of Chemical Physics 18:817–829

Juang JY, Bogy DB, Bhatia CS (2007) Design and Dynamics of Flying Height Control Slider With Piezoelectric Nanoactuator in Hard Disk Drives. ASME J Tribology 129:161-170

Karniadakis GE, Beskok A, Aluru N (2005) Micro Flows and Nano Flows: Fundamentals and Simulation. Springer-Verlag, New York

Kim BH, Beskok A, Cagin T (2008) Thermal interactions in nanoscale fluid flow: molecular dynamics simulations with solid–liquid interfaces. Microfluid Nanofluid 5(4):551-559

Kim BH, Beskok A, Cagin T (2008) Molecular dynamics simulations of thermal resistance at the liquid-solid interface. Journal of Chemical Physics 129:174701

Kim BH, Beskok A, Cagin T (2010) Viscous heating in nanoscale shear driven liquid flows. Microfluid Nanofluid 9:31-40

Lee J, Aluru NR (2010) Separation of Gases from Gas-Water Mixtures Using Carbon Nanotubes. Applied Physics Letters 96:133108.

Li Y, Xu J, Li D (2010) Molecular dynamics simulation of nanoscale liquid flows. Microfluidics and Nanofluidics doi: 10.1007/s10404-010-0612-5

Loyalka SK, Petrellis N and Storvick TS (1979) Some exact numerical results for the BGK model, Couette, Poiseuille and Thermal creep flow between parallel plates. J. Appl. Math. Phys. (ZAMP), 1:514–521

Mecke M, Winkelman J, Fischer J (1997) Molecular dynamic simulation of the liquid-vapor interface: The Lennard-Jones fluid. The Journal of Chemical Physics 107(21):9264-9270

Park JH, Bahukudumbi P, Beskok A (2004) Rarefaction effects on shear driven oscillatory gas flows: A DSMC study in the entire Knudsen regime. Phys Fluids 16(2):317–330

Rettner CT (1998) Thermal and tangential-momentum accommodation coefficients for N2 colliding with surfaces of relevance to disk-drive air bearings derived from molecular beam scattering. IEEE Trans Magnet 34(4):2387–95

Sazhin OV, Borisov SF, Sharipov F (2001) Accommodation coefficient of tangential momentum on atomically clean and contaminated surfaces. J Vacuum Sci Technol A – Vacuum Surf Films 19(5):2499–503

Shen C (2005) Rarefied Gas Dynamics. Springer-Verlag. Berlin

Sonntag RE, Borgnakke C (2002) Tables of Thermodynamics and Transport Properties. Computer-Aided Thermodynamic Tables Software Provided by Fundamentals of Thermodynamics. Wiley, New York

Sone Y, Takata S, Ohwada T (1990) Numerical analysis of the plane Couette flow of a rarefied gas on the basis of the linearized Boltzmann equation for hard sphere molecules. European Journal of Mechanics B/Fluids 9:273–288

Steele WA (1973) The physical interaction of gases with crystalline solids I. Gas-solid energies and properties of isolated adsorbed atoms. Surface Science 36:317–352

Stefanov S, Gospondinov P and Cercignani G (1998) Monte Carlo simulation and Navier–Stokes finite difference calculation of unsteady-state rarefied gas flow. Phys. Fluids, 10: 289

Sun J, Li ZX (2008) Effect of gas adsorption on momentum accommodation coefficients in microgas flows using molecular dynamic simulations. Molecular Physics 106:2325–2332.

Sun J, Li ZX (2010) Two-dimensional molecular dynamic simulations on accommodation coefficients in nanochannels with various wall configurations. Computer and Fluids doi:10.1016/j.compfluid.2010.04.004

Sun J, Li ZX (2011) Three-Dimensional Molecular Dynamic Study on Accommodation Coefficients in Rough Nanochannels doi: 10.1080/01457632.2010.509759

Tagava N, Yoshioka N, Mori A (2007) Effects of ultra-thin liquid lubricant films on contact slider dynamics in hard-disk drives. Tribology International 40:770-779

Thompson PA and Troian SM A general boundary condition for liquid flow at solid surfaces. Nature, 389(6649):360-362, 1997

Todd BD, Evans DJ, Daivis PJ (1995) Pressure tensor for inhomogeneous fluids. Physical Review E doi:10.1103/PhysRevE.52.1627

Tsai DH (1971) The Virial Theorem and Stress Calculation in Molecular Dynamics. Journal of Chemical Physics 70(3):1375–1382.

Willis DR (1962) Comparison of kinetic theory analyses of linearized Couette flow. Phys. Fluids A, 30:127–135

Woods LC (1993) An Introduction to the Kinetic Theory of Gases and Magnetoplasmas. Oxford Science publications

Veijola T, Kuisma H, Lahdenperi J (1998) The influence of gas-surface interaction on gas-film damping in a silicon accelerometer. Sensors and Actuators A 66:83-92.

Verbridge SS, Craighead HG, Parpia JM (2008) A megahertz nanomechanical resonator with room temperature quality factor over a million. Applied Physics Letters doi:10.1063/1.2822406.

Yamamato K, Takeuchi H, Hyakutake T (2006) Characteristics of Reflected Gas Molecules at a Solid Surface. Physics of Fluids doi:10.1063/1.2191871

Yang YT, Callegari C, Feng XL, Roukes ML (2011) Surface adsorbate fluctuations and noise in nanoelectromechanical systems. Nano Lett. 11:1753–1759.

Zhang WM, Meng G, Zhou JB, Chen JY (2009) Nonlinear dynamics and chaos of microcantilever-based TM-AFMs with squeeze film damping effects. Sensors doi:10.3390/s90503854

Zhou L (2007) Adsorption: Progress in fundamental and application research. World Scientific, New York

VITA

MURAT BARISIK
Research Assistant
Old Dominion University
Mechanical & Aerospace Engineering
Institute of Micro and Nanotechnology
ECSB 1300, Elkhorn Avenue
Norfolk, VA 23509-0247
muratbarisik@yahoo.com

Ph.D. Old Dominion University, Norfolk, VA, USA, May, 2012,
Major: Mechanical and Aerospace Engineering,
Dissertation: Molecular Dynamics Studies on Nanoscale Gas Transport
Advisor: Dr. Ali Beskok

M.S. Middle East Technical University, Ankara, Turkey, June, 2008,
Major: Mechanical Engineering,
Dissertation: Analytical Solution for Single Phase Microtube Heat Transfer including Axial Conduction and Viscous Dissipation
Advisor: Dr. Almila Guvenc Yazicioglu
Co-Advisor: Dr. Sadik Kakac

B.S. Middle East Technical University, Ankara, Turkey, June, 2006,
Major: Mechanical Engineering,

Book

1. Beskok A, Kim B, Barisik M (2012) Contemporary Perspectives on Molecular Simulations of Liquid and Gas Nanoflows. Begell House, New York. *Under Review.*

Journals

1. Barisik M, Beskok A (2012) Boundary Treatment Effects on Molecular Dynamics Simulations of Interface Thermal Resistance. Journal of Computational Physics, *under review.*
2. Shi Z, Barisik M, Beskok A (2012) Interface Thermal Resistance between Liquid Argon and Various Solids. International Journal of Thermal Sciences, doi:10.1016/j.ijthermalsci.2012.04.009.
3. Barisik M, Beskok A (2012) Surface-Gas Interaction Effects on Nanoscale Gas Flows. Microfluidics Nanofluidics, *Accepted.*
4. Barisik M, Beskok A (2011) Molecular Dynamics Simulations of Shear Driven Gas Flows in Nano-Channels. Microfluidics Nanofluidics, doi:10.1007/s10404-011-0827-0.
5. Barisik M, Beskok A (2011) Equilibrium Molecular Dynamics Studies on Nanoscale-confined Fluids. Microfluidics Nanofluidics, doi:10.1007/s10404-011-0794-5.
6. Barisik M, Kim B, Beskok A (2010) Smart Wall Model for Molecular Dynamics Simulations of Nanoscale Gas Flows. Communications in Computational Physics, doi:10.4208/cicp.2009.09.118.